

ADVANCED MATERIALS AND PRODUCTION TECHNIQUE APPLICATIONS

Editor
HASAN KÖTEN



BİDGE Yayınları

**ADVANCED MATERIALS AND PRODUCTION
TECHNIQUE APPLICATIONS**

Editor: HASAN KOTEN

ISBN: 978-625-372-763-5

1st Edition

Page Layout By: Gzde YCEL

Publication Date: 2025-06-25

BİDGE Yayınları

All rights reserved. No part of this work may be reproduced in any form or by any means, except for brief quotations for promotional purposes with proper source attribution, without the written permission of the publisher and the editor.

Certificate No: 71374

All rights reserved © BİDGE Yayınları

www.bidgeyayinlari.com.tr - bidgeyayinlari@gmail.com

Krc Bilişim Ticaret ve Organizasyon Ltd. Şti.

Gzeltepe Mahallesi Abidin Daver Sokak Sefer Apartmanı No: 7/9 Çankaya /
Ankara



PREFACE

In engineering studies, more and more importance is given to disciplines such as engineering and natural sciences to determine the limit points. Parameters used in optimization studies are used as limit values to determine the most efficient points. The application of these limit values is based on fundamental elements such as production methods and advanced material techniques. In this book, we focus on the latest studies in this field, including theoretical, numerical, experimental and optimization, as well as special production and material techniques. We believe that these engineering techniques will be a valuable reference for both researchers and technical personnel involved in practical applications. We would like to thank the authors of the chapters in this book and hope that our book will be useful for both our industry and research centers.

Editor

Assoc. Prof. Dr. HASAN KÖTEN

İSTANBUL MEDENİYET ÜNİVERSİTESİ

İÇİNDEKİLER

A TECHNICAL OPINION ABOUT MINE SHAFTS	1
<i>HASAN KOTEN</i>	
INVESTIGATION OF THE EFFECT OF THERMOMECHANICAL PROCESSES APPLIED TO 5083 QUALITY ALUMINUM ALLOY ON MICROSTRUCTURE AND HARDNESS PROPERTIES	28
<i>HAYRETTİN AHLATCI, KENZA DJEBARI</i>	
INVESTIGATION OF THE EFFECT OF THERMOMECHANICAL PROCESSES APPLIED TO 5083 QUALITY ALUMINUM ALLOY ON MICROSTRUCTURE AND HARDNESS PROPERTIES	58
<i>YAVUZ SUN, HAYRETTİN AHLATCI</i>	
CORROSION PERFORMANCE AND H ₂ EVOLUTION OF AS-CAST AND EXTRUDED MG-2ZN-1Y-0.5X (X = GD, LA, ZR, AG, CA) ALLOYS IN SIMULATED PHYSIOLOGICAL CONDITIONS	88
<i>HAYRETTİN AHLATCI</i>	
ARTIFICIAL INTELLIGENCE BASED APPLICATIONS IN MATERIALS AND METALLURGY	138
<i>NİDA KATI, FERHAT UÇAR</i>	
ARTIFICIAL INTELLIGENCE DRIVEN IMAGE ANALYZES IN MATERIAL SCIENCE	155
<i>NİDA KATI, FERHAT UÇAR</i>	
HAZELNUT SHELL FLOUR FILLED EPOXY COMPOSITES: CHARACTERIZATION AND MECHANICAL PROPERTIES	171
<i>MURAT EROĞLU</i>	
NANO SURFACE PRODUCTION AND APPLICATIONS USING NATURAL HONEY	189
<i>NACİYE SÜNDÜZ OĞUZ</i>	

CHAPTER 1

A TECHNICAL OPINION ABOUT MINE SHAFTS

HASAN KÖTEN¹
GÜLNAZ DALOĞLU
SERKAN AYTAŞ

Introduce

There are two the traditional methods to access in deep mines. A shaft is used to equipment and hoisting machine in the lower horizons. Descending ramp (decline) trasportations of people, equipment, skip and ore cage (Hetemi and Zeqiri, 2016).

The choice of methods depends on the topography, the slope of the bed, the thickness and angle of the bed, the deposit size and depth, the rock nature, the roof rocks and the condition of the ground water (Skrzypkowski et al., 2022). Additionally, the depth, the rate of production and the mine life affect to access ways. Table 1 shows the production rate, the depth and mine life of the different countries's mines (Costa et al., 2017).

¹ Head of Mechanical Engineering Department, Istanbul Medeniyet University

Table 1. *The production rate, depth and mine life of the different countries's mines*

Company	Anglo Gold	LKAB	Leviathan Resources Ltd	Lepanto	RTZ	Codelco
Mine	Cuiaba	Kiruna	Stawell	Far Southeast	Palabora	El Teniente
Location	Brazil	Sweden	Australia	Philippines	South Africa	Chile
Production rate (ton/day)	3600	52000	Up to 1000	17000	60000	100000
Mining methods	Cut and fill	78% sublevel caving 22% sublevel stoping	-	Blasthole	Block caving	Block caving
Mineral	Au	Fe	Au	Au	Cu	Cu
Depth (m)	840 (shaft) 1200 (mine) forecast to reach 1600 m.	915	1350	1524	1219	610
Mine life	2026	30+	-	Under construction	Under construction	+50
Main access	Shaft/ decline	shaft	Decline	shaft	Shaft	Shaft/ decline

Brazilian underground mines have low depths (up to 800 m), the production rate and short mine life span. South Africa has greater depths of the gold mines. So, it has high production rate and long mine life. Australia has longer depth than 1000 m with the shaft. The production rates, the life and the depth in the Brazil's mine are low than others. So, the decline (ramp) is preferred in the Brazil's mine (Costa et al., 2017).

Shaft systems can be used for various purposes in underground mines and tunnels. They are opened vertically or inclined for the purpose of transporting materials, ore and personnel. According to their purposes, production (ore and waste), service (personnel and material transport), ventilation (air intake and

definition), search and escape. Shaft classification according to their depths is shown in Table 2 (Melih İphar lecture notes, 2024).

Table 2. Shaft classification against to depth

Vertical shaft	Depth
Shallow	<500 m
Middle depth	500-1000 m
Deep	1000-1500 m
Very deep	>1500 m

Three access ways to deep ore deposit are explained to as following:

Access by Vertical Shaft

The shaft passes through the roof rocks, the ore deposit and the floor rocks (Fig.1) (Costa et al., 2017).

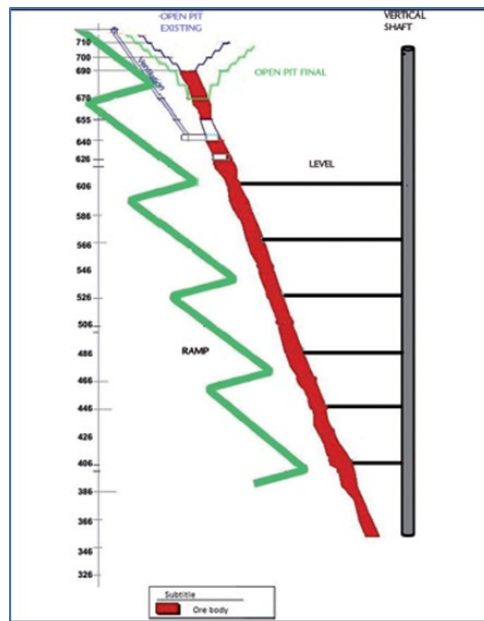


Fig. 1. The vertical shaft

The advantages of vertical shafts are: 1) The shaft easy keeps, because the rock mass pressure on the lining is low,2) The rope wear is low and the shaft short length,3) The water drainage's cost is low and transport capacity is high (Skrzypkowski et al., 2022).

Access by Decline

The direction of driving decline is from top to bottom while the haulage is carried out from the opposite direction. Also, spiral ramps are driven in greater deposit' s depths (Fig. 2a-b) (Skrzypkowski et al., 2022).

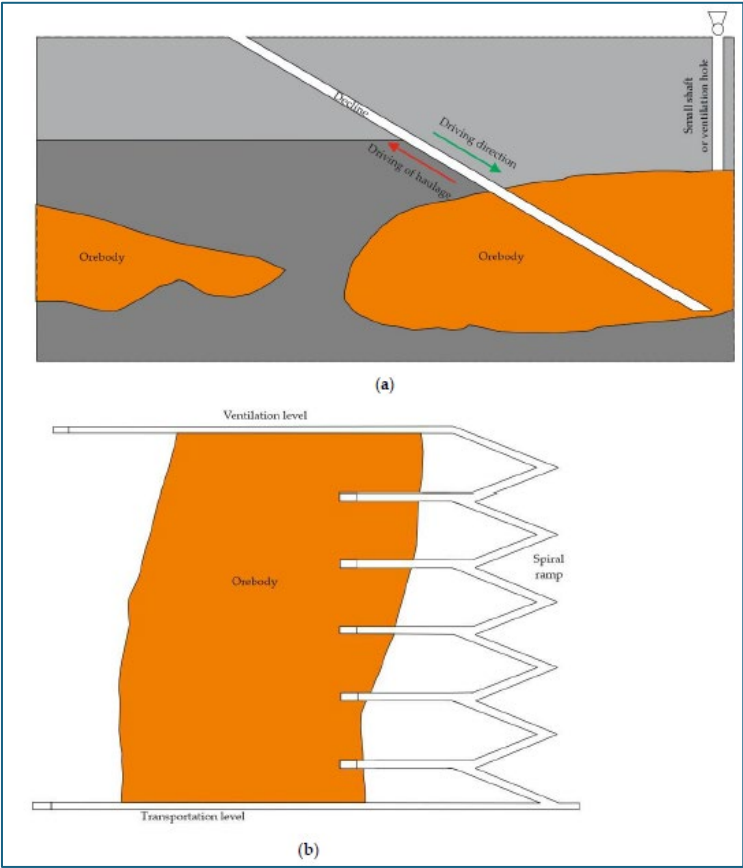


Fig. 2. a) Access of decline and b) the spiral ramp

The advantages of decline: 1) Fuel section machines (TBM) are used for excavation, 2) Easier movement of the mining crew, 3) Using a belt conveyor obtains high efficiency. The disadvantages are; 1) The length and several times, ventilation resistance have great to access a specific level, 2) Haulage efficiency is lower (Skrzykowski et al., 2022).

Access by Inclined Shaft

Inclined shafts have several inclination. The advantages of them: operating costs are reduced, the length of stone drifts is shorter and fast preparation for exploitation (Skrzykowski et al., 2022) (Fig 3).

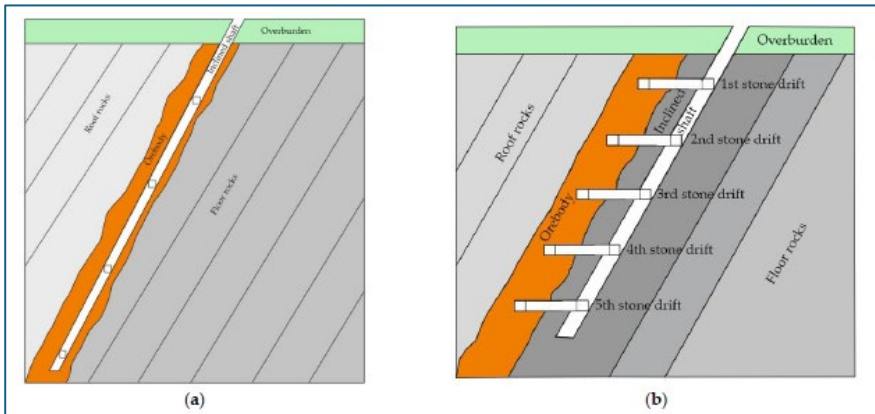


Fig. 3. Access of Inclined Shaft (IS)

The inclined shaft lining structure (ISLS)' s stability is affected by many factors, such as water pressure, the joint, soft rock, lining corrosion, groundwater seepage, cross-sectional shape, formation inclination angle, sidewall height, SL thickness to diameter ratio, lateral pressure coefficient and surrounding rock strength (Fig.4) (Ren et al., 2023).

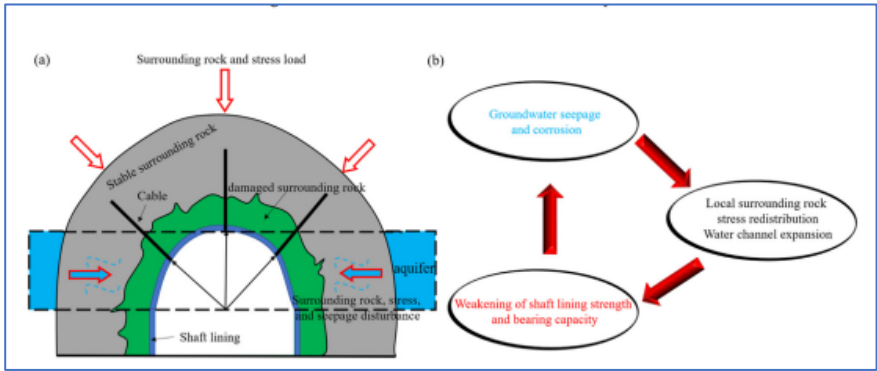


Fig. 4. Influencing factors of incline shafts lining structure instability

Shaft lining concrete is affected by multiple factors in ultra-deep mines. For example; high temperature increase the ultra-high density calcium silicate hydrate content and diminish the Ca/Si ratio. Also, it is developed the mechanical properties of ultra-high performance of concrete. The fibre-reinforced high-performance concrete (FRHPC) and the fibre-reinforced reactive powder concrete (FRRPC) are used in ultra-deep mines. The compressive strength of the FRHPC decreases and the hydration and pozzolanic reaction are little. However, the hydration and pozzolanic reaction are presented and the compressive strength is a stable value in FRRPC. Thus, FRRPC is preferred than the FRHPC in coastal ultra-deep mines (Zhou et al., 2020).

There are three instability risks of the IS: non instability, high and potential instability risk zones in Fig. 5.

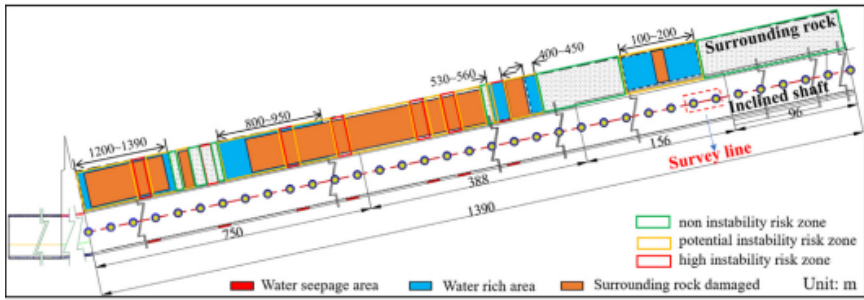


Fig.5. Three instability risks of the IS

To prevent instability risk zones, hydrophobic hole drainage and back-lining gravity are carried out for the water seepage resources and surrounding rock micro fissure. Additionally, stability support measures in shafts are given such as; bolt-cable active support, grooving or drilling pressure, back-lining grouting, steel pipe concrete support and U-shape steel support, reinforced support scheme (Ren et al., 2023).

There are four main problems to access of deposits. Firstly; determination of the size and nature of the stresses of the excavations and in the protective pillars. The selection of proper strength rocks to drive excavations, the cross section and the support method. Secondly; proper climatic working conditions in deep mines. To obtain intensive ventilation, determine the correct location of the inlet and outlet shafts, fresh air inflow, air discharge roads, air speed and cooling intensity of the main fans. The third group includes gas and methane capacity of coal seams at great depths. Finally; negative factors of depth on the transport of people, material, water and output. Thus, the total capital expenditures should be calculated before operating and preparation.

The Sum of Capital Expenditures

Operating costs per 1 ton of extraction can be formulated in Equ. (1) and the extraction is used to Equ. 2 (Skrzypkowski et al., 2022).

$$\sum R = f(L, n) \quad (1)$$

$$\tilde{\eta} = (1 - 0.01a), p = 0.0016b \quad (2)$$

Where; L= length of the mining area, n=level's number, a=operational losses, b= output dilution. For n=1-3 and L=100-1500, Equ. 3 is used:

$$\frac{d\sum R}{dL} = 0, \frac{d\sum R}{dn} = 0 \quad (3)$$

The main steps of mining works: preparatory and exploitation of the deposit. The exploitation is carried to obtain proper extraction depend on the geological and mining conditions. The preparatory works are taken in to account: determine of the conditions and variable parameters of the deposit and efficient mining methods (Skrzypkowski et al., 2022). The time advance indicator for exploitation is formulated by the Equ (4).

$$t_0 = \frac{t_e}{t_{a+d}} \quad (4)$$

Where; t_0 =time advance indicator, t_e = horizontal exploitation time (days), t_{a+d} = time to access and prepare the level (days). There are two horizontal planes: the transport and drainage level are on the lower plane and the ventilation and material level are on the upper plane. The heigh of level are affected some factors: the degree of determine of the deposit, the mechanical and physical properties of rocks, the angle of inclination, the investment outlays per 1 ton of excavated material, the access and prepare period for exploitation.

If the level height is high, the deposit resources, the costs of ventilation and support maintenance, haulage and dewatering and delivering materials for exploitation are rising. Thus, lower heights are propered in thin and irregular and tectonically deposits. The height of (H_1) related to the production capacity of the shaft is formulated in Equ. (5).

$$H_1 = \frac{P \cdot \sin \alpha \cdot (1-p)}{n \cdot L \cdot m \cdot \gamma \cdot \eta} \quad (5)$$

Where; P= annual mining capacity of the shaft (tons), p= output dilution coefficient, n= operating wings number (parts), L=annual progress of exploitation works along strike (m), m= deck thickness (m), γ =output volume weight (t/m^3), η =deposit utilization factor, α =the deck angle ($^\circ$) and H_1 = height of level (m).

The height of the H_1 level is formulated related to the minimum expenditure per 1 ton of extraction in Equ. (6).

$$H_1 = \sqrt{\frac{(V \cdot K_0 + L_k \cdot K_k + L_e \cdot R_e)(1-p)}{0.5 \cdot (e+b+\Delta) \cdot S \cdot \eta \cdot \gamma}} \quad (6)$$

Where; V= workings volume around shaft (m^3), K_0 = 1 m^3 making cost of a rock excavation, L_k = level length of the preparatory excavation (m), K_k = 1 m unit cost of the drift (m^2), S= deposit horizontal projection (m^2), e= 1 ton haulage cost of excavated material, b= per 1 ton dewatering cost of extraction, Δ = per 1 ton operating costs increase of excavated material in the height level increase by 1 m. If the access and preparatory works are assumed in advance of the operational works at the higher level, Equ. 7 can be used.

$$H_1 > \frac{P \cdot w \cdot t \cdot (1-p)}{S \cdot \gamma \cdot \eta} \quad \text{if } w > t_0/t \quad (7)$$

Where; w = advance factor, t_0 =exploitation time, t = access and preparatory time in the lower mining level (Skrzypkowski et al., 2022).

Mine Hoisting Shaft

The shaft is a bridge the surface and the underground mining space. A mine hoisting system occurs some parts: shaft, tower movement and haulage systems (cage/ skip) and rope (Fig. 6) (Zhou et al., 2022).

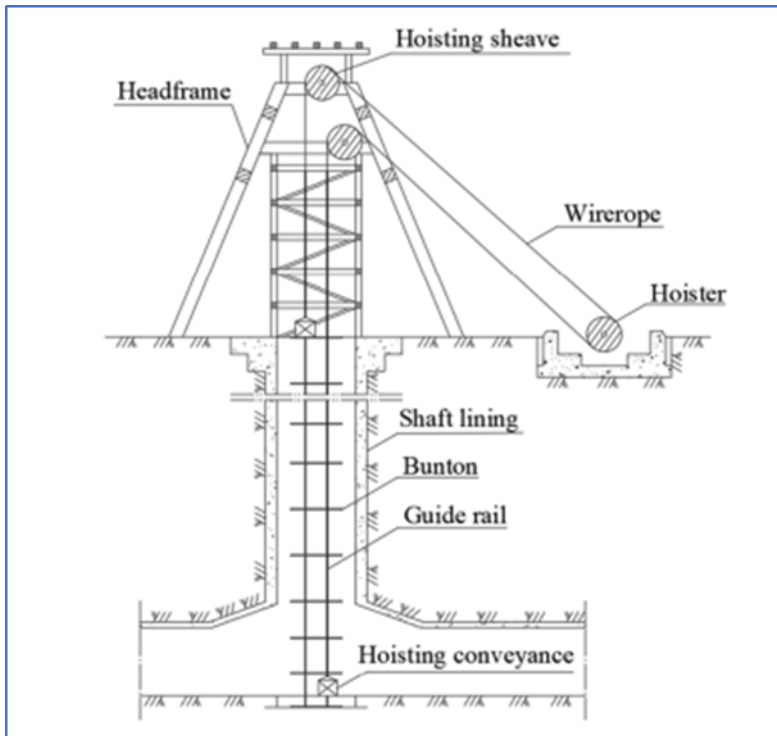


Fig.6. Parts of a Mine Hoisting System

When the mine hoist transport ore and miners from the surface to the underground levels of the mine, there are some risks. Hoisting accidents represent 1.2 % of the fatalities in miners over the 2000-2019. A mine conveyance is a major disaster source. The

conveyance speed is 1500 feet/min (8 m/s) to transport workers. The safety integrated level (SIL) rating is determined to the four risk factors. They are:

- Harm severity (S_e) (between 1-4),
- Harm class probability, $CI=Fr+Pr+Av$,
- Exposure frequency and duration of persons to the hazard, Fr (between 2-5),
- A hazardous event occurrence probability, Pr (between 1-5),
- Harm limit or avoid possibility, Av (1,3 or 5),

A list of essential safety functions for a mine hoist is established by Programmable electronic system (PES):

1. The conveyance speed and track limits,
2. The conveyance collision in the shaft,
3. Personnel safety devices,
4. Emergency stop/validation device,
5. Safety circuit reactivation,
6. Breaking system,
7. The electrical, drive, chain protection,
8. PES and shaft sinking operations.

The safety-related electrical control systems (SRECS) design is a decision-making for mine hoist (Galy and Giraund, 2023).

China use friction hoists for medium-sized and deep mine shafts. Thus, friction coefficients affect shaft lining capacity, safety, efficiency and performance. The frictional lining is a viscoelastic material with good thermal stability, low wear losses, oil-water resistance, flame retardant, high friction coefficient. Friction lining consists of matrix, fillers (SiO_2 , montmorillonite) and additives

(accelerator, antioxidant agent, plasticiser). Three friction lining (K25, G30 and GM-3) commonly used in minashaft hoist. Table 3 shows properties of K25, G30 and GM-3 (Zhang et al., 2016).

Table 3. Properties of K25, G30 and GM-3 friction lining materials

Materials	K25	G30	GM-3
Decomposition temperature ($^{\circ}$ C)	362.5	383.2	317.8
Carbon content (%)	71.46	72.9	58.99
Hardness (HD)	71	75	69
Friciton coefficient at 15 mm/s	0.65	0.57	0.8

Microstructure of three friction lining materials present in Fig. 7 (Zhang et al., 2016).

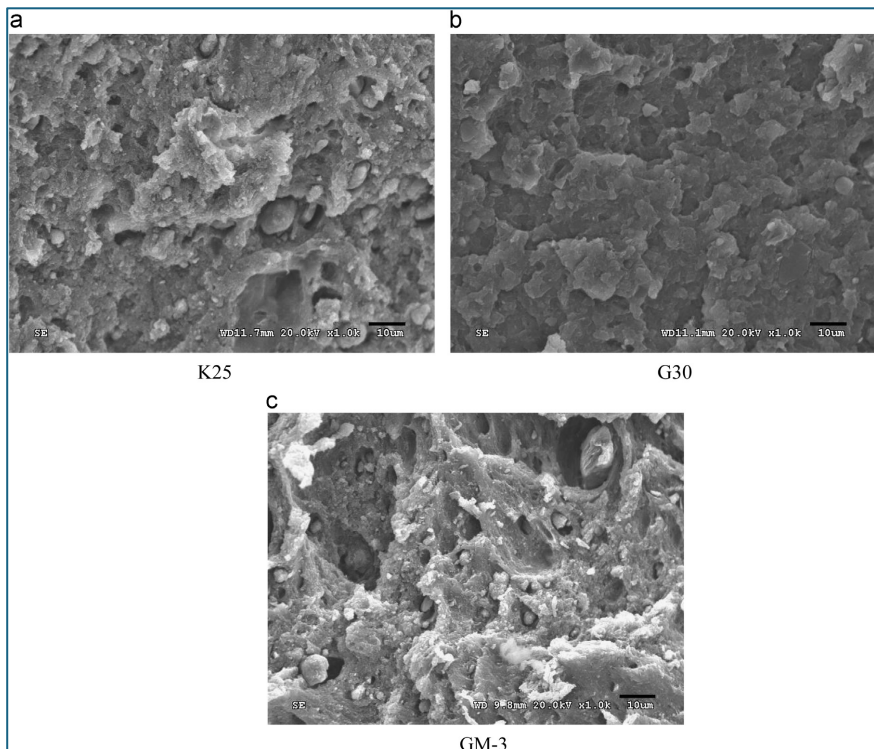


Fig. 7. Microstructure photos of materials.

According to studies, higher methylene and filler contents increase friction coefficient, but thermal decomposition affects this correlation.

A Guide rail deformation laws

A guide rail is the crucial vertical shaft element for the hoisting conveyance. There are deformation laws related to different connection states, positions. The force direction on the guide rail bears the vertical upward force in the upper and lower sections and the vertical downward force in the middle section. Deformation laws are related to the bottom aquifer water head (BAWH) and the vertical additional force (VAF). The BAWH is the position change of the elastoplastic interface. Thus, it is obtained the VAF distribution law of the shaft. The VAF's Equ. 8 is shown.

$$\tau(z) = \begin{cases} \frac{k_s u_0}{(e^{\varepsilon Z_p} + e^{-\varepsilon Z_p})} (e^{\varepsilon z} + e^{-\varepsilon z}), & z \leq Z_p \\ c + \lambda p z \tan \phi, & z > Z_p \end{cases} \quad (8)$$

Where; k_s = the unit stiffness coefficient between the soil and the shaft lining, u_0 = the relative shear displacement between the soil and the shaft lining for the elastoplastic position, D = the shaft dimension, $\varepsilon = \sqrt{(\pi D k_s)/(EA)}$, E = the longitudinal elastic modulus, A = the cross section area, z = the distance between the location and the top surface of the shaft, Z_p = the distance between the elastoplastic interface and the top surface of the shaft, c = the strength index cohesion, I_i = the average lateral pressure coefficient of the soil against to the shaft lining at Z_p depth, p = the average effective gravity density, ϕ = the internal friction angle. Table 4 is presented to the basic parameters of the a mine shaft (Zhou et al., 2022).

Table 4. Basic parameters of an auxiliary shaft

D(m)	A(m ²)	E(Mpa)	H(m)	k _s (mPa)	U _o (m)	C(Mpa)	φ	λ	I _i (MN/m ³)
8.9	29	10000	243	113.86	0.007	0.13	18.1	0.5	0.01

If the Z_p is given ΔH and the shaft vertical stress at z=230 m, Table 5 is supplied.

Table 5. Z_p changed to ΔH of an auxiliary shaft

ΔH (m)	5	10	15	20	25	30	35	40	45	50
Z _p (m)	240.1	234.9	230.7	216.2	204.3	200.6	197.1	193.7	190.6	187.6
Σz=230 MPa	0.31	1.19	2.95	10.53	15.03	16.79	18.05	19.84	20.90	22.35

According to theoretical results, the shaft lining ruptures when the BAWH disceases to 48 m (Zhou et al., 2022).

When the ground is in plastic stage, a shaft lining is necessary. When the ground tolerates the elastic stress by sinking a shaft, the support is necessary. Researches presented to the Mohr-Coulomb and Hoek-Brown rock masses for a circular tunnel. Hoek-Brown failure criterion is used to elastic-perfectly plastic behave for rock mass in Equ. 9 (Öztürk and Güler, 2016):

$$\sigma_1 = \sigma_3 + \sigma_{ci} \left(m_b \frac{\sigma_s}{\sigma_{ci}} + S \right) \quad (9)$$

Where; σ_1, σ_3 = the major and minor effective failure principal stress, σ_{ci} = the uniaxial compressive strength for intact rock material, m_b = the minimized value for material constant m_i , s and a = constants for rock mass. Equations 10-11-12 give m_b , s and a constants:

$$m_b = m_i \exp \left(\frac{GSI-100}{28-14D} \right) \quad (10)$$

$$s = \exp \left(\frac{GSI-100}{9-3D} \right) \quad (11)$$

$$a = \frac{1}{2} + \frac{1}{6} \left(e^{-GSI/15} + e^{-20/3} \right) \quad (12)$$

Where; D= a disturbance factor due to blast damage and stress relaxation, GSI= geological strength index (Öztürk and Güler, 2016). D= 0 for undisturbed rock mass and D=1 for very disturbed rock mass. A lining pressure (P_i) in a plastic rock is predicted by Terzaghi in equ. 13.

$$P_i = \frac{2}{(\tan \beta + 1)} \left\{ \sigma_h + \frac{\sigma_c}{\tan \beta - 1} \right\} \left(\frac{r}{R} \right)^{(\tan \beta - 1)} - \frac{\sigma_c}{(\tan \beta - 1)} \quad (13)$$

Where; tan β= the passive pressure coefficient, σ_h= the horizontal ground stress, σ_c= uniaxial compressive stress, r= shaft radius, R= zone radius. A lining pressure (P_i) in a brittle rock is predicted by Talobre in equ. 14.

$$P_i = \left\{ \frac{c}{\tan \phi} + \sigma_h (1 - \sin \phi) \right\} \left(\frac{r}{R} \right)^{(\tan \beta - 1)} - \frac{c}{\tan \phi} \quad (14)$$

Where; c= cohesion, φ= the angle of friction. The thickness of the shaft lining (t_c) can be found from Equ. 15 using Lamé's thick wall cylinder.

$$t_c = r \left(\sqrt{\frac{f_c}{f_c - 2P_i}} - 1 \right) \quad (15)$$

Where; f_c=concrete allowable compressive stress, n= the coefficient of lining.

** According to Poland Branch Standart, P_i=0.013z for saturated sand, P_i=0.017z for clays.

The maximum support pressure of the concrete is formulated by Haynes in Equ. 16.

$$P_i = f_c \left(2.17 \frac{t_c}{2r} - 0.04 \right) \quad (16)$$

Concrete strength (P_i) should be 20-25 MPa in underground mines and not exceeds 50 MPa. The minimum and maximum lining thickness (t_c) are 25 and 150 mm for different rock masses (Öztürk and Güler, 2016).

Sample: Calculation of P_i for 2 m radius shaft for 60 m depth, $\sigma_{ci} = 30 \text{ MPa}$, $GSI=30$, $k_2=2$, $r=2 \text{ m}$, $f_c=25 \text{ MPa}$. If we use Equ.6 and 7;

According to regression analysis, Equ. 6 shows to lining pressure P_i (MPa):

$$P_i = -0.029\sigma_{ci} - 0.068GSI + 0.535\sigma_z + (2.752k_2^2 - 4.048k_2 + 4.950)$$

$$P_i = -0.029 \times 30 - 0.068 \times 30 + 0.535(60 \times 0.027) + (2.752 \times 2^2 - 4.048 \times 2 + 4.950) = 5.81 \text{ MPa.}$$

$$t_c = 2 \left(\sqrt{\frac{25}{25 - 2 \times 5.81}} - 1 \right) = 73 \text{ cm.}$$

Mine Ventilation Shaft

The mining process (ventilation and transport) needs a long period in the deposit. There are two connections of the underground mines in the surface; intake shaft (fresh air supply) and exhaust shaft (exhaust air discharge). Harmful gases can accumulate in the shafts. Thus, the forcing systems commonly are used to vertical and inclined shafts's ventilation (Semin and Lenvin, 2021). A plan of mining ventilation is shown in Fig. 8 (He et al. 2023).

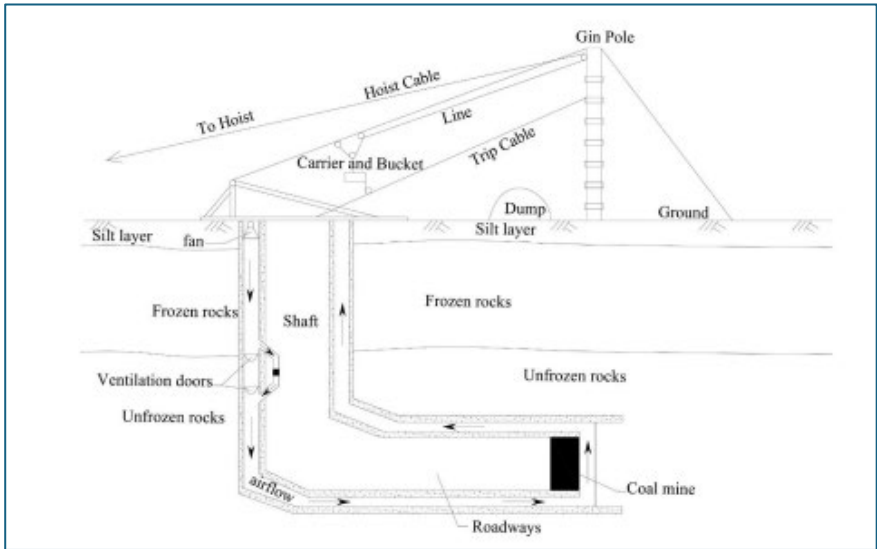


Fig.8. Mine ventilation system

Airflow, temperature, radon gass and humidity equations in a shaft are given as following parts, respectively.

Airflow formulas

The fresh air flows from the surface to the floor by the ventilation duct. If the air flow moves up the shaft and shaft wall temperature is minimized than the air temperature, the air velocity distorted in the shaft. Thus, theoretical formulas of airflow patterns in a vertical mine shaft are mentioned. Boussinesq Equation(17) is a density of a fluid depends on temperature (Semin ve Lemin, 2021).

$$P = P_0(1 + \beta(T - T_0)) \quad (17)$$

Where; P= the fluid density at a unstabil temperature(kg/m³), P₀ = known fluid density at a reference temperature (kg/m³), β= the air thermal expansion coefficient (1/°C). The critical Rayleigh number for laminar flow is calculated in Equ. 18.

$$Ra_{er} = \frac{g\beta AR^4}{v\chi} = \pi^4 \approx 100 \quad (18)$$

Where; g = gravity acceleration (m/sn^2), A = vertical temperature gradient ($^0C/m$), R = shaft radius (m), v = air kinematic viscosity (m^2/s) and χ = the air thermal diffusivity (m^2/s). The critical Rayleigh number for turbulent flow is calculated in Equ. 19.

$$A_{cr} = \frac{\pi^4 v \chi}{g \beta R^4} + \frac{g M}{\gamma \beta R_g (T + 273.15)}$$

$$Ra_{er} = \frac{g \beta A R^4}{v \chi} = \pi^4 + \frac{g^2 R^4}{\gamma v \chi R_g (T + 273.15)} \quad (19)$$

Where; γ = the adiabatic coefficient, R_g = the universal gas constant ($J/mol/K$) and M = the molar mass (kg/mol). The critical Rayleigh number is determined to turbulence air flow properties in a shaft cross-section There are three crucial factors:

1. Affect of the average air velocity in the shaft on return air flows,
2. Non-zero temperature gradient,
3. Changes of the turbulent properties in a shaft.

According to these parameters, Shalimov derived the average air velocity in the vortex in the inclined mine airway in Equ.20.

$$V = \sqrt{\frac{g}{2} \frac{P_u - P_d}{P_u + P_d} (L \sin \alpha + D \cos \alpha)} \quad (20)$$

Where; P_u = air density in the upper airpart (kg/m^3), P_d = air density in the lower airpart (kg/m^3), L = shaft length (m), D = airway diameter (m) and α =air way angle (0). The minimum allowable air velocity in mine shaft (v_{min}) is formulated to Equ. 21 (Semin ve Lemin, 2021).

$$v_{min} = \frac{v_1}{R} \left(\frac{g\beta\Delta TR^3}{0.19v_1X_1 \cdot 10^{10}} + 6.26 \right)^4 \quad (21)$$

Where; R= shaft radius (m), β = the air thermal expansion coefficient ($1/^\circ\text{C}$), v_1 = the air kinematic viscosity (m^2/s), X_1 = the air thermal diffusivity (m^2/s), ΔT = the difference of temperature ($^\circ\text{C}$).

Sample: Calculate to the minimum allowable air velocity in mine shaft (v_{min}), parameters are shown as following:

$$g=9.81 \text{ m}^2/\text{s},$$

$$v_1=1,48 \cdot 10^{-5} \text{ m}^2/\text{s},$$

$$X_1=1,85 \cdot 10^{-5} \text{ m}^2/\text{s},$$

$$\Delta T=5,05 \text{ } ^\circ\text{C}$$

B=0.0034 and R= 4 m. from the Equ. M;

$$v_{min} = \frac{v_1}{R} \left(\frac{g\beta\Delta TR^3}{0.19v_1X_1 \cdot 10^{10}} + 6.26 \right)^4 =$$

$$\frac{1,48 \cdot 10^{-5}}{4} \left(\frac{9.81 \times 0.0034 \times 5.05 \times 4^3}{0.19 \times 1.48 \cdot 10^{-5} \times 1.85 \cdot 10^{-5} \cdot 10^{10}} + 6.26 \right)^4 = 1,96 \text{ m/s}$$

Temperature formulas

The airflow temperature in the shaft calculates the relation between airflow temperature and the shaft depth, ground temperature, initial rock temperature, ventilation time and ventilation amount in Equ. 22.

$$t_1 = t_{y1} - (t_{y1} - t_0) \exp \left(- \frac{2\pi\lambda K_T \varepsilon Z}{Gc_{pk}} \right) + \frac{Z(1+d_0)}{427(c_{pk} + d_0 c_{psh})} \quad (22)$$

Where; t_{y1} = the mean initial temperature of rock at the first shaft section, Z= the depth of each shaft section (10 m), t_0 = beginning airflow temperature, λ = thermal conductivity of rock around the shaft, ε = heat ratio (0.3), c_{pk} = specific heat capacity of air (1.0 kJ/kg $^\circ\text{C}$), c_{psh} = specific heat capacity of air (1.84 kJ/kg $^\circ\text{C}$), d_0 = air

humidity, K_{ζ} = heat transfer coefficient between airflow and rock around the shaft (0.503), G = the amount of the wind. There is a linear relationship between the convective heat coefficient (h) of a concrete surface and wind speed v , (m/s) in Equ. 23-24 (He et al., 2023).

$$h = 3.06v + 4.11 \quad (23)$$

$$G = p_{air}vS \quad (24)$$

Where; h = coefficient heat transfer, v = wind speed, p = the air density (kg/m^3), S = the sectional area of the shaft (m^2) and G = ventilation amount.

**For mining ventilation conditions; if $G=30$ kg/s, $h=13.91$ $\text{W/m}^2\text{ }^{\circ}\text{C}$ and if $G=10$ kg/s, $h=7.38$ $\text{W/m}^2\text{ }^{\circ}\text{C}$.

If the G is constant, the airflow temperature (T_a) varies to time “ t ” and depth “ x ” of the shaft in Equ. 25.

$$T_a = a + b \cdot \sin\left(\frac{2\pi t}{8760} + c\right) \quad (25)$$

Where; T_a = airflow temperature in the shaft, a - b - c =parameters to the depth of the shaft.

If the $G=30$ kg/s, parameters of a and b and T_a are formulated in Eq. 26-27-28.

$$a = 0.025x - 3.3 \quad (26)$$

$$b = 12.7 \exp\left(\frac{x}{69.45}\right) + 2.81 \times 10^{-5} \quad (27)$$

$$T_a = 0.022x - 3.3 + \left(12.7 \exp\left(-\frac{x}{69.45}\right) + 2.81 \times 10^{-5}\right) \sin\left(\frac{2\pi t}{8760} - \frac{3\pi}{5}\right) \quad (28)$$

Where; t = ventilation time (hours), x =shaft depth (m). If the $G=10$ kg/s, T_a is calculated in Eq. 29.

$$T_a = 0.022x - 1.92 + \left(12.7 \exp\left(-\frac{x}{26.57}\right) + 1.85 \times 10^{-5}\right) \sin\left(\frac{2\pi t}{8760} - \frac{3\pi}{5}\right) \quad (29)$$

Finally, the wind amount (G) depends on the wind speed, air density and shaft cross-section. The heat/humidity transfer is important between the air temperature of the shaft and around rocks in winter seasons. When the shaft depth rises, the air temperature increases in summer seasons. Thus, airflow temperature is major factor in the stability of the supporting structure of the shaft (He et al., 2023).

Radon emission formulas

Radon emits in uranium mines' s shaft as a nuclear energy source. Its emission concentration is affected by the shaft location and height, gas emission velocity, wind speed and direction, atmospheric stability, precipitation, topography (Xie et al., 2014). Radon concentration of the air in the shaft contributes to pollution in the mines. Thus, China has two provisions in the nuclear industrial standard:

- 1) Empirical limit- 100.000 T annual ore-hoisting must not be as ventilation shaft,
- 2) Mandatory limit- the intake air radon concentration must not be 200 Bq m⁻³ (Zhao et al., 2019).

The radon release rate of the shaft is formulated as Equ. 30 (Zhou et al., 2019).

$$P=C_x V_x S \quad (30)$$

Where; P= the radon release rate, C= the radon concentration of the air outlet of ventilation shaft (Bq m^{-3}), V= air speed (m/s), S= area of shaft (m^2).

Sample: Calculate to radon gas concentration and air velocity, parameters are shown in Table 6 (Zhou et al., 2019).

Table 6. Radon concentration parameters

Shaft depth	300 m.
Shaft inner diameter	3.5 m.
Shaft height	2.5 m.
Wall thickness	30 cm.
Air speed at inlet of shaft	7-10 m/s,
Radon concentration	22-51KBq m^{-3}
Relative humidity	% 90-100
Air temperature	20±2 °C

According to results, air speeds of outlet of shaft change between 6.37-9.65 m/s in different inlet air velocities (5, 7, 10, 15 m/s) at different cross-sections. Radon concentration is between 21-63 kBqS^{-1} and maksimum in shaft centre, minimum in shaft side (Zhou ve ark., 2019).

The effective dose rate (E/T) of radon from ventilation shaft outlet is estimated by Equ. 31 (Xie et al., 2014).

$$E/T=CxFxD \quad (31)$$

Where; E/T= public personnal effective dose rate (mSv h^{-1}), C= radon concentration (Bq m^{-3}), F= an equilibrium factor to outdoors (0.6), T= the annual exposing hours from questionnaires (h y^{-1}), D= dose conversion factor (9×10^{-6} $\text{mSv per Bq m}^{-3} \text{ h}$). The sum of the public personnal effective dose rate (mSv h^{-1}) is calculated from Equ. 32:

$$E_{\text{total}}/T = \sum_v f_v x C_v x F x D \quad (32)$$

Humidity formulas

The moisture accumulation in the air and ground water inflows provide air resistance in the shaft. The air resistance and fan pressure rise in the shaft. The barometric pressure changes to depth of the shaft in Equ. 33 (Semin and Zaitsev, 2020).

$$P = P_0 - p_0 g(x - H) \quad (33)$$

Where; P_0 = surface barometric pressure (Pa), p_0 = air density of surface, (kg/m^3), g = gravity acceleration (m/s^2), x = vertical coordinate of shaft (m), H = shaft section height. The moist density of air is calculated from Equ. 34.

$$p_a = \frac{29P - 0.11\phi(479 + (11.52 + 1.62T)^2)}{8314(T + 273)} \quad (34)$$

Where; ϕ = the air relative humidity (%). The saturated water vapour pressure (P_s) is formulated to Equ. 35.

$$P_s = 611 \exp\left(\frac{17.5T}{T + 241.2}\right) \quad (35)$$

*If the air velocity < 9.22 m/s, the water droplets fall,

* If the air velocity > 9.22 m/s, the water droplets increase,

* If the air velocity = 9.22 m/s, the water droplets have turbulent air flow.

The pressure drop (ΔP) is a function of the air velocity (v) of the shaft. Equ. 36 is used for the $v < 9.22$.

$$\Delta P = \frac{P_{fan}(v - 9.22) + P_{fan} \sqrt{\frac{4gvI(v)}{SP_{fan}} + (v - 9.22)^2}}{2v} \quad (36)$$

Equ. 37 is used for the $v \geq 9.22$.

$$\Delta P = \frac{P_{fan}(v-9.22) - P_{fan} \sqrt{\frac{4gvl(v)}{SP_{fan}} + (v-9.22)^2}}{2v} \quad (37)$$

Sample: Calculate to the moisture effect in the shaft, parameters are shown in Table 7 (Semin ve Zaitsev, 2020).

Table 7. Thermodynamic parameters of Val Reefs (Rusya) mining ventilation shaft

Mine Name	Oktyabrskiy				Taimyrskiy	
Shaft	VS1	VS2	VS3	VS4	VS6	VS7
Air speed (m/sn)	12.2	8.5	12.5	7.8	8.8	6.6
Shaft cross length (m)	584	578	935	645	1371	1610
Shaft diameter (m)	6.5	6.5	6.5	6.5	6.5	8
Inlet air temperature (°C)	15	17	17	19	20	24
Inlet relative air humidity (%)	82	82	84	81	90	86
Outlet air temperature (°C)	12.6	14.3	8	14	10.5	14
Average temperature per 100 m (°C)	0.41	0.47	0.96	0.93	0.76	0.62

According to results, the water droplets relative speed is constant (9.22 m/s) for turbulence flow in the ventilation shaft. This value does not depend on geometric sizes of the shaft, but it is determined to air and water densities.

Conclusion

Mine shafts are crucial systems for deep underground mines and tunnels to transport and natural ventilation. Currently, spiral shafts are preferred than classical shafts in countries. Many parameters can be effect to mine hoisting system's parts, such as the shaft lining structure, friction coefficients, frictional lining material, concrete strength, concrete materials, and guide rail deformation. Additionally, the airflow velocity, humidity and temperature values

affect to the ventilation quality of the shaft. China, specially modeled to toxic gasses (radon) amount of a shaft in uranium mines in view as nuclear energy source. All parameters determine to optimum capital costs and the proper time before exploitation and preparatory of the ore deposit according to mine safety regulations.

References

Costa, L.V., Silva, J.M., Lima, H.M., 2017. Analysis of options of production and Access ways in underground mines, *Mining Mineraçao*, 70,2,237-242.

Galy, B., Giraud, L. 2023. Risk mitigation strategies for automated current and future mine hoist, *Safety science*, 167, 106267.

He, W., Sheng, Y., Cao, W., Ning, Z., Tian, M., Wang, Y. 2023. Thermal stability prediction of frozen rocks under fluctuant airflow temperature in a vertical shaft based on finite difference and finite element methods, *Case Std. in Therm. Eng.*, 52,103700.

Hetemi, M., Zeqirir, R., 2016. Concept Paper on shaft of the Mine “Trepca” in Stanterg New Horizons XIth to XIIIth, *J. Int. Env. App. & Science*, 11,1, 65-71.

İphar, M. 2024. Maden Makinaları ders notları, *Esogü Maden Mühendisliği bölümü*, 45.

Ren, Z., Zhang, C., Wang, Y., Lan, S., Liu, S. 2023 Stability analysis and grouting treatment of inclined shaft lining structure in water-rich strata: A case study, *Geohazard Mech.*, 1,308-318.

Semin, M., Zaitsev, A. 2020. On a possible mechanism for the water build-up formation in mine ventilation shafts, *Thermal science and Eng. Progress*, 20,100760.

Semin, M., Levin, L. 2021. Theoretical study of partially return air flows in vertical mine shafts, *Ther. Sci. And Eng. Progress*, 23,100884.

Skrzypkowski, K., Zagorski, K., Zagorska, An., Sengani, F. 2022. Access to deposits as a stage of mining Works, *Energies*, 15,8740, <https://doi.org/10.3390/en15228740>.

Öztürk, H., Güler, E., 2016. A methodology for lining design of circular mine shafts in different rock masses, *Int. Jou. of mining science and Tech.*, 26,761-768.

Xie, D., Wang, H., Kearfott, K.J., Liu, Z., Mo, S. 2014. Radon dispersion modelling and dose assessment for uranium mine ventilation shaft exhaust under neutral atmospheric stability, *Journal of Env. Radioactivity*, 129,57-62.

Zhang, D., Chen, K., Zhang, X. 2016. Comparison of the thermophysical properties, microstructures, and frictional behavior of lining materials used in mine hoists, *Wear*, 354-355, 1-9.

Zhao, J., Ma, C., Xiao, X., Jiang, Y. 2022. Research on deformation law of guide rails caused by mine vertical shafts under non-mining action, *Eng. Failure Analysis*, 134,106089.

Zhou, Q., Liu, S., Xu, L., Zhang, H., Xiao, D., Deng, J., Pan, Z. 2019. Estimation of radon release rate for an underground uranium mine ventilation shaft in China and radon distribution characteristics, *Jou. of Env. Radioactivity* 198,18-26.

Zhou, Y., Liu, J., Huang, S., Yang, H., Ji, H. 2020. Performance change of shaft lining concrete under simulated coastal ultra-deep mine environments, *Cons. And Build. Materials*, 230-116909.

CHAPTER 2

INVESTIGATION OF THE EFFECT OF THERMOMECHANICAL PROCESSES APPLIED TO 5083 QUALITY ALUMINUM ALLOY ON MICROSTRUCTURE AND HARDNESS PROPERTIES

1. Yavuz SUN¹

2. Hayrettin AHLATCI²

Giriş

Aluminum is the most abundant metal in the earth's crust. Aluminum, one of the most produced alloys among non-ferrous metals, has led to its use in many different application areas due to its superior properties. Apart from its superior properties, the easy availability of raw materials, advanced production techniques and cheapness are other reasons for its high consumption. Aluminum's ability to alloy with many metals enables it to obtain the necessary properties for special applications. One of the most important features of aluminum-based materials is that their density is low but

¹ Prof. Dr., Karabük University, Faculty of Engineering, Department of Metallurgy and Materials Engineering, Orcid: 0000-0002-7336-5591,

² Prof. Dr., Karabük University, Faculty of Engineering, Department of Metallurgy and Materials Engineering, Orcid: 0000-0002-6766-4974,

their strength/density ratio is high. The mechanical properties of metals depend on their microstructure, which in turn depends on the composition of the material, the solidification process, and the heat treatments and mechanical shaping processes applied after solidification. Aluminum alloys can be shaped more easily than other materials. Commercial pure aluminum is a light, ductile, soft material with high machinability and corrosion resistance. Although pure aluminum is a very soft material, its strength can be significantly increased by applying cold forming processes. Another way to increase strength is to alloy with elements such as magnesium, silicon, copper, zinc and manganese that can cause solid solution hardening (Mısırlı, 2011:97).

AA 5083 Aluminum alloy is an aluminum alloy containing 4-5 % Magnesium and some Manganese and Chromium additions. It is an alloy that can be hardened by alloying and cold working. For many applications, the alloy can be supplied in hot rolled coils in the 3–10 mm thickness range. For thinner applications, the material is cold rolled and optionally soft annealed. Most structural applications require sheet with good formability. However, under certain processing conditions, significant portions of the alloy have been observed to consist of grains that are considerably elongated in the rolling direction, with small recrystallized grains. This partially recrystallized structure, caused by the extremely high Mg and Cr contents of the alloy, is undesirable due to its negative effects on ductility and formability. It is well known that the application of a suitable homogenization cycle can strongly facilitate the recrystallization behavior of AA 5xxx series alloys (Sheppard & Raghunathan, 1989: 268) (Hollinshead, 1992: 57) (Engler & et al., 1994: 7711) (Radeti, Popovi & Romhanji, 2012: 16) (Engler, Liu & Kuhnke, 2013: 111) (Vetrano & et al., 1994: 565). This makes high-Mg AA 5xxx alloys recrystallized microstructures with fine grain sizes possible by a special thermo-mechanical process, making such

alloys suitable. The fine-grained alloy AA 5083 is the most used material in superplastic forming processes (Iwasaki & et al., 1998:199) (Cleveland, Ghosh & Bradley, 2003: 228).

In this study, new generation 5083Al-Bi alloys were produced by adding 1.2% Bismuth to AA5083 Al alloy. The changes in the microstructure and hardness properties of these new generation Al alloys were examined by applying two different thermomechanical processes.

Casting And Heat Treatment of AA5083 Quality Al Alloys

The 5083 Al alloy and the Bismuth added 5083 Aluminum alloy to be used in this study were produced in Karabük University, Metallurgical and Materials Engineering Casting laboratory (Figure 1.1).

Figure 1 (a) Induction furnace, (b) Atmosphere controlled gas equipments.



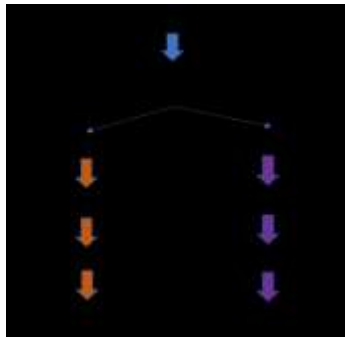
(a)

(b)

After casting, all samples were first homogenized in the Protherm Brand heat treatment furnace within Karabük University Metallurgy and Materials Laboratories. All experiments were continued on homogenized materials. Based on literature research, homogenization process was applied to 5083 Al and 1.2% Bi Added 5083 Al – Bi alloys with a 24-hour waiting period in the oven heated to 500oC.

The heat treatment and Thermomechanical process sequence to be applied after homogenization is shown as a diagram in Figure 2. Aging process was applied as a result of both methods called Thermomechanical 1 and Thermomechanical 2. The method in which cold rolling is applied after homogenization, then taken into solution and aged, is called Thermomechanical 1, and the method in which the materials that are homogenized and then taken into solution are aged after cold rolling is called Thermomechanical 2.

Figure 2. Applied thermomechanical process stages.



Two different temperatures were determined to apply the aging process under optimum conditions after the solution process. 8 different time periods such as 4h-8h-16h-24h-36h-42h-56h-72h were determined at low temperatures of 120oC and 150oC, and the aging process was carried out in the heat treatment furnace. has been implemented. The microstructure and hardness results of the samples aged for 4h-8h-16h-24h-36h-42h-56h-72h at 120oC and 150oC were analyzed. Considering the microstructure images and hardness results of the materials after aging at both temperatures, 150oC was determined as the optimum aging temperature. The subsequent experimental process was continued on materials aged at 150oC for periods of 4h-8h-16h-24h-36h-42h-56h-72h.

Before cold rolling, two test materials aged for 24 hours at 500 °C were prepared for Thermomechanical 1, and materials that

were put into solution at 530 °C for 2 hours were prepared for Thermomechanical 2. Before rolling, the materials were sanded with 400-600-800-1000-1200-2500 mesh to ensure surface smoothness. A specially made rolling device available at Karabük University Metallurgical and Materials Engineering was used as the rolling device (Figure 3.).

Figure 3. Cold rolling device used for rolling process.



Microstructural And Mechanical Characterization

Optical microscope (LOM), scanning electron microscope (SEM) were used for microstructure images of 5083 quality Aluminum alloy and 5083 AL-Bi alloy with 1.2 % Bismuth addition, and Energy Dispersive X-Ray (EDX) analysis was used for the determination of elements. X-Ray Diffraction Pattern (XRD) was performed to determine the phases, but no results were obtained because the phases in the structure were smaller than the diameter of the measurement probe.

Standard metallographic procedures were applied to obtain images under LOM and SEM. The samples were cut into 10 x 10 mm shapes and cold molded using a mixture of epoxy resin and hardener. The surfaces were sanded and polished and made ready for etching. A mixture of 25% hydrochloric acid (HCL) + 25% Nitric acid (HNO₃) + 25% hydrofluoric acid (HF) + 25% CH₃OH was used as etching acid, and after waiting for 10 seconds, the surface was cleaned with alcohol and dried. Microstructure images were

taken with a Nikon brand optical microscope and then images were taken with SEM and EDX analysis was performed.

In this review, XRD qualitative examinations were made of the 5083 quality and 5083 Al-Bi alloys that we produced and subjected to aging heat treatment. Examinations were made between 10 degrees and 90 degrees scanning angles on the Rigaku Ultima IV brand (Figure 4.). Since the diameter of the measurement probe was larger than the diameter of the phases, the phases could not be captured and a healthy data flow could not be received.

Figure 4. Rigaku Ultima IV X-Ray Diffraction Spectrometer.



Figure 5. Hardness Test Device.



Mechanical properties were determined by Vickers hardness measurements at room temperature. The hardness of the metallographically prepared samples was determined by the Vickers Hardness test on the Shimadzu brand HMV model device (Figure 5). In the experiment, hardness values were determined by using a pyramid-shaped penetrating tip and keeping it under a load of 0.5 Newton for 15 seconds and measuring the diagonal lengths of the

resulting trace. For each test sample, 10 measurements were made and the average value was taken for the result.

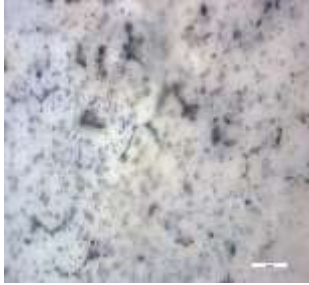
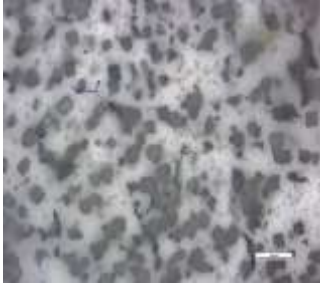
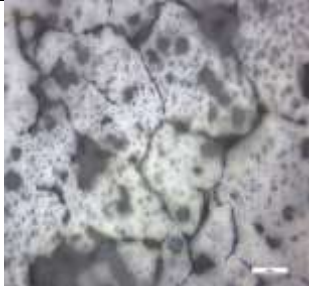
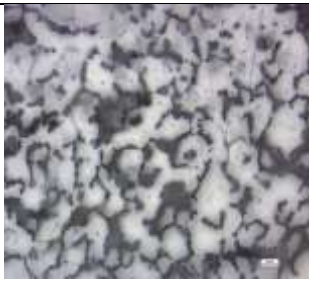
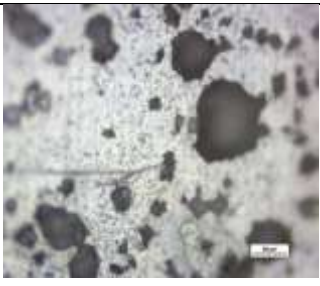
Characterization Results And Discussion

The chemical composition of 5083 quality aluminum according to BS EN 573-3:2009 standard, the chemical composition of cast AA5083 quality aluminum used in this study and cast 5083 aluminum alloys with 1.2% Bismuth addition, measured after spectral analysis, are given in Table 1. In the table, the chemical composition of BS EN 573-3:2009 AA 5083 quality material is given in comparison with the chemical composition of the casting 5083 alloy used in this study and the 5083 alloy with 1.2% Bismuth addition. According to these results, casting 5083 alloy production, which achieved standard material quality, was successfully carried out.

Table 1. Chemical compositions of cast 5083 Al and cast 5083 Al-Bi alloys.

Elements (%)	BS EN 573-3:2009 AA5083	As-cast AA5083	As-cast AA5083 Al-Bi
Al	-	95,40	95,16
Bi	-	0,002 den az	1,27
Mg	4,00-4,90	3,00	1,94
Mn	0,40-1,00	0,42	0,30
Fe	0,40	0,31	0,37
Si	0,0-0,40	0,32	0,33
Ti	0,05-0,25	0,029	0,03
Cr	0,05-0,25	0,10	0,12
Cu	0,10	0,27	0,30
Zn	0,0-0,10	0,08	0,10
Another	0,0-0,15	0,058	0,07

Table 2. Optical microscope images of 5083 Al and 1.2% Bismuth added 5083 Al-Bi alloy.

	5083	5083-Bi
Homogenized (H)		
Aged (Y)		
Thermo-mechanical Treatment 1 (T1)		
Thermo-mechanical Treatment 2 (T2)		

Microstructure analyzes were performed by looking at optical microscope images of 5083 Al and 5083 Al-Bi alloys at each process stage (homogenized, aged, thermomechanical process 1 and

thermomechanical process 2). Optical microscope images of all alloys are given in Table 2.

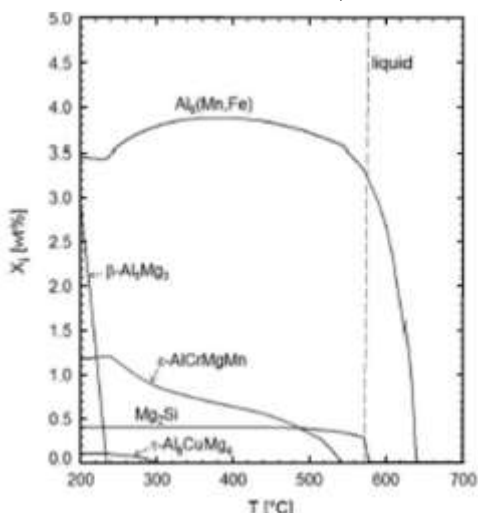
In the microstructure image of the homogenized 5083 Al material, it was seen that small blackish and gray particles of various sizes were distributed on the matrix. It can be said that grain boundaries begin to form in the microstructure with the aging process, and small particles scattered on the matrix are found both within the grain boundary and in the matrix. After homogenization, cold rolling was applied and in the microstructure image of the aged (T1) material, an image was captured in which there was an increase in the number of grain boundaries, capillary grain boundaries were formed and scattered small particles began to collect at the grain boundaries. After homogenization, it was taken into solution and cold rolled and aged. In the microstructure image of the material (T2), distinct grain boundaries were formed and the capillary grain boundaries turned into thick dark grain boundaries. In addition to the small particles within the grain boundary, the capillary grains seen in the previous microstructure remained between the grain boundaries.

When the optical microstructure images of 5083 Al-Bi Alloy with 1.2% Bismuth addition are examined; In the microstructure image of the homogenized 5083 Al-Bi alloy, a microstructure image like the 5083 Al material without Bismuth addition was detected. With the aging process, the grain boundaries began to form almost indistinctly. It is seen that in the thermomechanical process 1 (T1) microstructure, particles larger than the initial size of the black particles were formed, and the grain boundaries did not become very evident. Distinct dark grain boundaries were formed in the thermomechanical process 2 (T2) microstructure. At this stage, when the microstructures of 5083 Al and 5083 Al-Bi alloys were compared, it was observed that in the Bismuth material, the microstructure started to form late at the grain boundaries, and

distinct grain boundaries formed in Thermomechanical Process 2. The effect of this situation on the mechanical properties of the material can be associated with the hardness results.

In their study (Olaf & Simon, 2001: 100), Olaf Engler and Simon Miller-Jupp analyzed the phases formed in the structure by homogenization annealing of AA5083 material. Olaf and Simon, who applied homogenization annealing at low and high temperatures, used Calphad simulation to determine the phases. Calphad simulation uses a large database containing the 14 most important alloying elements of Al alloys (Cr, Cu, Fe, Mg, Mn, Ni, Si, etc.). Figure 6. shows the results of Calphad equilibrium simulations for the AA 5083 alloy in the form of the fraction of phases that emerge as a function of temperature. The scheme appears to be dominated by a Mn and Fe bearing phase called Al₆. According to Calphad simulations, Al₆(Mn, Fe) contains 14% Mn and 11% Fe plus a few tenths of a percent of both Mg and Cr, but no Si. They noted that the equilibrium simulations did not show the cubic α -Al (Fe, Mn) Si phase, which is common in 5xxx alloys, where the Mg₂Si phase is seen in the structure. Olaf Engler and Simon Miller-Jupp stated that the dark phases are Mg₂Si phases, and the bright phases contain Fe, Mn and Cr elements and are rich in Fe and Mn contents. They divided the bright phases into three different types. The bulkier luminous particles contain on average 12% Mn and 15% Fe, plus about 0.35% Cr, but almost no Si. Therefore, these particles are probably called Al₆(Mn, Fe) phases. Components containing Fe and Mn with more sculpted shapes were classified as the "Chinese script", particles containing slightly higher Mn and Fe, and particles containing small amounts of Cr and Si as the α -Al (Fe, Mn) Si phase. Occasionally, they observed small Cr-rich particles containing 5% Cr and about 10–15% both Mn and Mg, but no Fe. They defined these particles as ϵ -Al₁₈(Cr, Mn)₂Mg₃ phase.

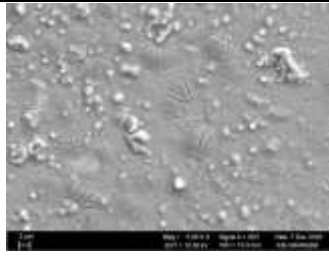
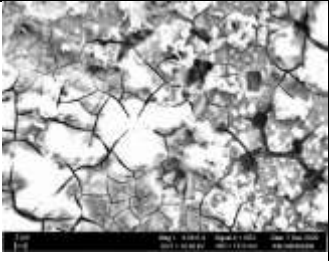
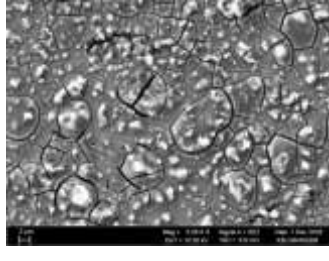
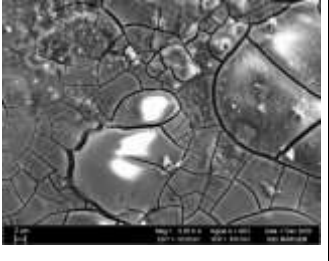
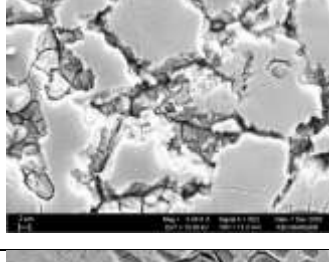
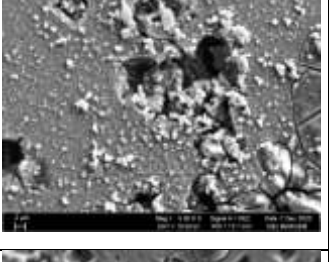
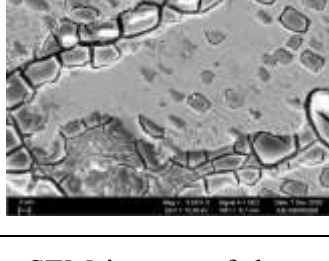
Figure 6. Calphad simulation results of AA5083 material (Olaf & Simon, 2001: 100).



The presence of dark and bright phases seen in the microstructure of 5083 Al and 5083 Al-Bi materials has similar results to the work of Olaf Engler and Simon Miller-Jupp. Microstructure images of 5083 Al and 5083 Al-Bi alloys were taken under a scanning electron microscope (SEM). SEM images of 5083 AL Alloy and 5083 Al-Bi Alloy are given in Table 3.

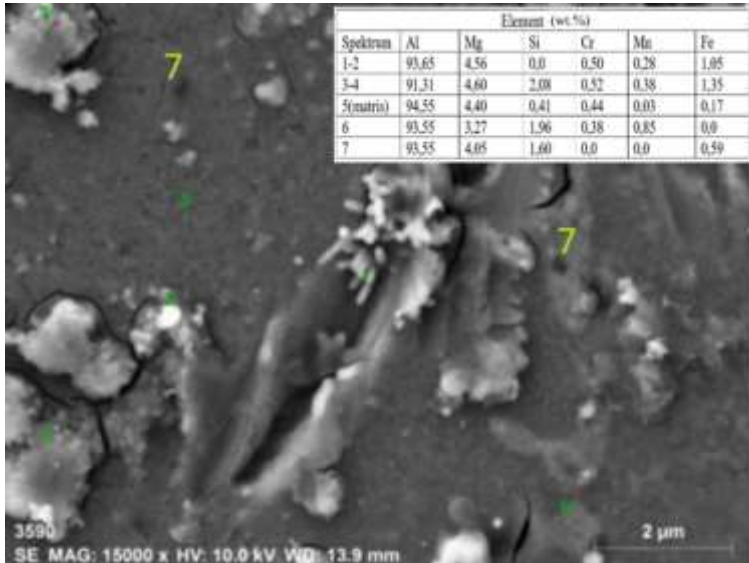
When the SEM Images of 5083Al and 5083 Al-Bi Alloys are examined in Table 3, 5083 Al material gives a smoother microstructure image than 5083 Al-Bi material. Smooth structure means regular particle distribution. In 5083 Al-Bi material, the excessive concentration of bright phases in one place and their absence in other places can be given as an example of this situation. We can tell the effect of the Bi plugin on this situation by looking at EDX analysis. In SEM images, while the presence of bright phases is more in the image after Homogeneous and aging in both materials, with the Thermomechanical Process these phases turn gray and the presence of dark phases begins to increase. It can be seen that especially the recrystallized phases are dark colored phases.

Table 3. SEM images of 5083 Al and 5083 Al-Bi alloy with 1.2% Bismuth addition.

	5083	5083-Bi
Homogenized (HB)		
Aged (YB)		
Thermo-mechanical Treatment 1 (TB1)		
Thermo-mechanical Treatment 2 (TB2)		

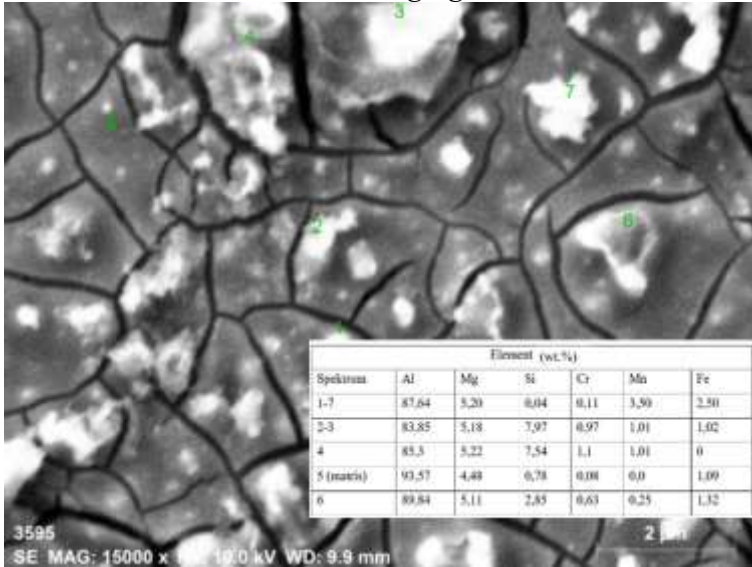
After the SEM images of the examined alloys were taken, EDX analyzes were examined to get an idea about the elemental analysis by weight in the microstructure. EDX results of 5083 Al alloys are given in Figures 7-10.

Figure 7. SEM image and EDX results of 5083 Al alloy after homogenization heat treatment.



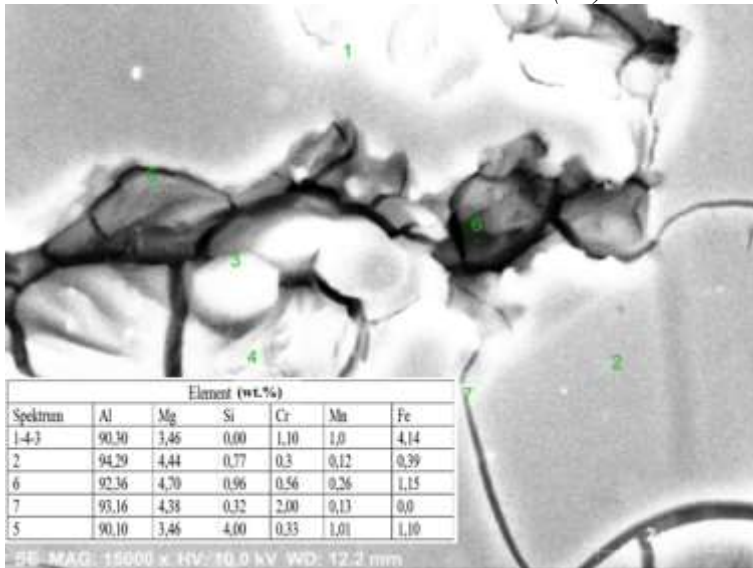
In Figure 7, shows the SEM image and EDX analysis results of 5083 Al material after homogenization (H). Since the phases marked 1 and 2 are Fe and Mn-rich, Si-free and bright phases, it can be said that they fully comply with the phase definition (Olaf & Simon, 2001: 100) in the work of Olaf Engler and Simon Miller-Jupp, and this phase is AL6 (Mn, Fe). The area marked 3-4 is again a bright phase and due to its rich silica content, these phases are thought to be α -Al (Fe, Mn) Si. Phase 5 is the matrix and phase 6 is the Fe-free Cr-rich ϵ -Al18 (Cr, Mn)₂ Mg₃ phase. Phase number 7 is the dark phase and is rich in Mg₂Si.

Figure 8. SEM image and EDX results of 5083 Al alloy after normal aging.



In Figure 8. SEM image and EDX analysis results of 5083 Al material after normal aging (Y) are given. It can be said that phases 1-7 are the bright $Al_6(Mn, Fe)$ phase and are widely found in the structure with the aging heat treatment. Region number 5 is matrix, region number 2 and 3 is $\alpha-Al (Fe, Mn) Si$, phase number 6 is Mg_2Si phase, and phase number 4 is $\epsilon-Al_{18}(Cr, Mn)_2 Mg_3$ phase. In the SEM image of 5083 material after aging, it is seen that the bright $Al_6(Mn, Fe)$ phase dominates the structure and this phase is distributed heterogeneously within the grain boundaries formed by aging. The commonly found $Al_6(Mn, Fe)$ phase can be defined as the constituent phase.

Figure 9. SEM image and EDX results of 5083 Al alloy after thermomechanical treatment 1 (T1).



In Figure 9. SEM image and EDX analysis results of 5083 Al material after T1 are given. With the effect of cold deformation, where the bright phases numbered 1-3-4 are Al₆(Mn, Fe), this phase spreads into the structure by showing banding, including grain boundaries and grain interiors. It seems to cover everything. It can be said that the dark phase number 6 is Mg₂Si, phase number 2 is the matrix, and phase number 7 is ε-Al₁₈(Cr,Mn)₂ Mg₃. Phase number 5 is the α-Al (Fe, Mn) Si phase.

Figure 10. SEM image and EDX results of 5083 Al alloy after thermomechanical treatment 2 (T2).

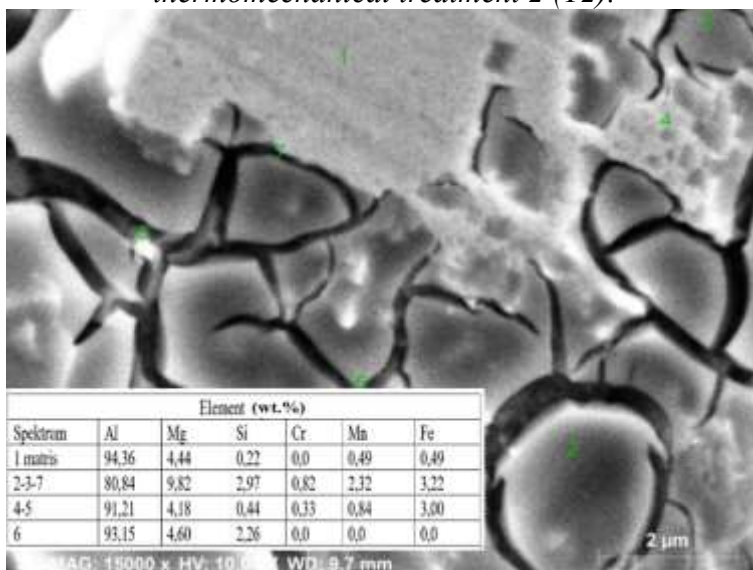


Figure 10 shows the SEM image and EDX analysis results of 5083 Al material after Thermomechanical Process 2 (T2). It can be said that phases 4 and 5 are the $Al_6(Mn, Fe)$ constituent phase. This phase spread into the structure under the effect of rolling without entering the grain boundaries. At the grain boundaries, there is a gray phase $\alpha-Al (Fe, Mn) Si$ phase with recrystallized structure numbered 2-3-7. Phase 6 is the Mg_2Si phase.

EDX results of 5083 Al-Bi alloys are given in Figures 11-14. The effect of the addition of 1.2 % bismuth on the phases can be interpreted using these figures.

Figure 11. SEM image and EDX results of 5083 Al-Bi alloy after homogenization.

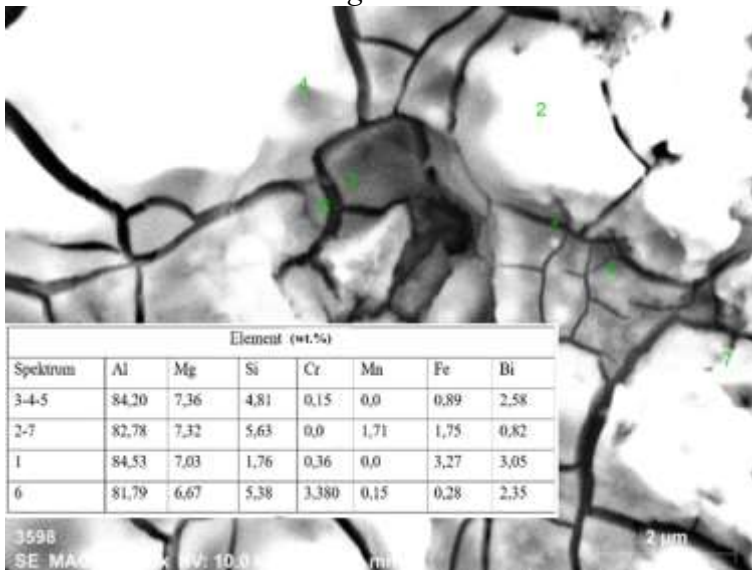


Figure 11 shows the SEM image and EDX analysis results of the 5083 Al-Bi alloy after homogenization. Phases 3-4-5 are Mg₂Si phase. Mg₂Si is one of the important reinforcement phases in magnesium alloy to improve thermal stability and high temperature properties due to its high melting point, high hardness, and low expansion coefficient (Palasantzas, 2002: 266) Palasantzas, G. (2002) (Martinez, Verlinden & Delaey, 1994: 6167) (Liu, Kang & Kim, 1999: 267) (Mondolfo, 1976: 100). However, due to the uneven distribution and irregular shape of the conventional Mg₂Si phase, it is very detrimental to the mechanical properties of the alloy. Therefore, what is necessary to strengthen Mg₂Si and increase its effect is to control its morphology and size (Ahravci & Pekkülyüz, 1998: 147). The most common modification process is to add modifying elements during the melting process (Murray & et al., 1987: 385). Addition of alloying elements is the easiest and most effective method to improve the mechanical and wear properties of alloys (Reddy, Dwivedi & Jain, 2009: 1) (Nam & et al., 2006: 238).

Sb, Ca, Bi, Pb, Ti, Zn and Zr are some of the alloying elements added to Mg alloys. The added alloying elements either dissolve or form compounds within the microstructure (Srinivasan & et al., 2010: 6543).

The addition of 1.2% Bismuth to the structure of the 5083 Al-Bi alloy was added with the expectation of minimizing the negative effects of Mg₂Si. Therefore, we can say that phase 3-4-5 is the Mg₂(Si, Bi) phase. Contrary to the SEM image of the 5083 alloy, the 5083 alloy with Bismuth addition revealed more bright phases. If we interpret this situation, it can be said that the dark gray phases tend to decrease as the addition of bismuth takes up space in volume.

In SEM and EDX analyzes of 5083 Al-Bi alloy after homogenization, it can be said that the phases marked with numbers 2-7 are α -Al (Fe, Mn, Bi) Si, phase number 1 is Al₆ (Mn, Fe, Bi) and phase number 6 is matrix.

Figure 12. SEM image and EDX results of 5083 Al-Bi alloy after normal aging.

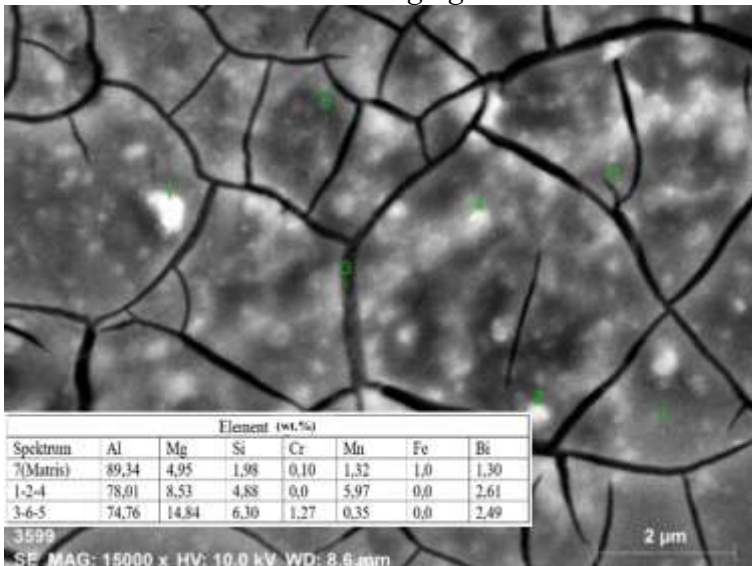


Figure 12 shows the SEM image and EDX analysis results of 5083 Al-Bi material after aging. Two distinct phases emerged in this

SEM image. These are Mg₂Si and Al₆(Mn,Fe) phases, which we call the constituent phases. Phases 1-2-4 show the Al₆(Mn, Fe, Bi) phase with the addition of bismuth to the component, and phases 3-6-5 show the Mg₂(Si, Bi) phase. Phase number 7 is the matrix.

Figure 13. SEM image and EDX results of 5083 Al-Bi alloy after thermomechanical treatment 1 (T1).

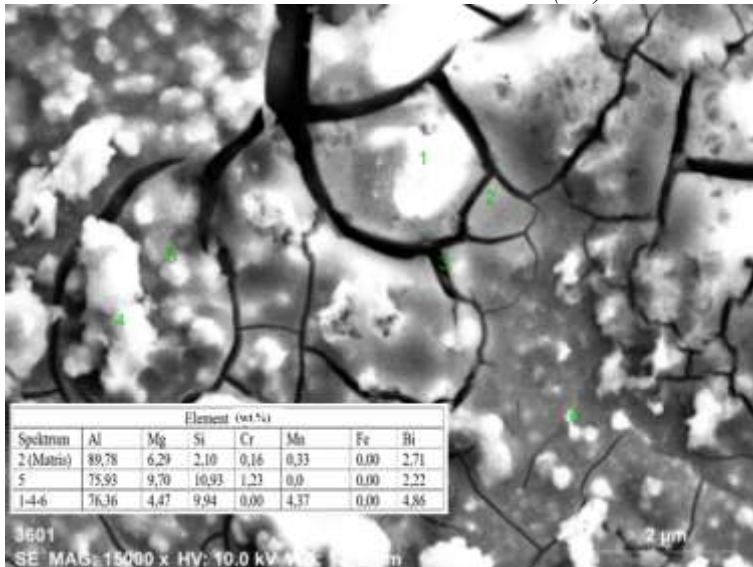


Fig.13. shows the SEM image and EDX analysis results of 5083 Al–Bi alloy after thermomechanical treatment 1 (TB1) are given. When we compare the SEM images of 5083 Bi-free and containing alloys, it can be said that the band-like structure resulting from rolling does not form in the TB1 stage in the Bismuth 5083 alloy, and the bright phases that were suppressed during aging become evident. The Fe percentage of these bright phases is zero, and they are phases with a high Si proportion. Although it is not appropriate to describe the previous constituent phases here due to the lack of Fe ratio, since the presence of bismuth addition takes up space in volume, it can be said that the Fe phases did not disappear from the structure and the constituent phases are fixed here as well.

Therefore, we can define phases 1-4-6 as Al₆(Mn,Bi). 2 matrix is 5 Mg₂(Si,Bi) phase.

Figure 14. SEM image and EDX results of 5083 Al-Bi alloy after thermomechanical treatment 2 (T2).

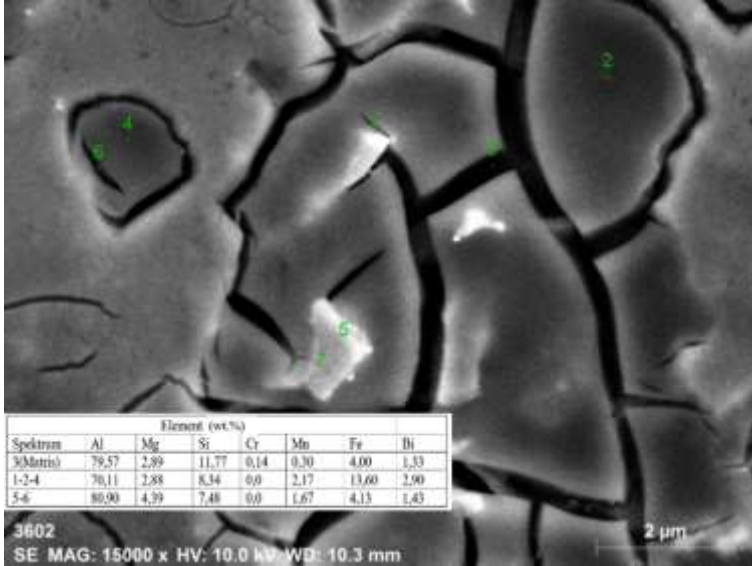


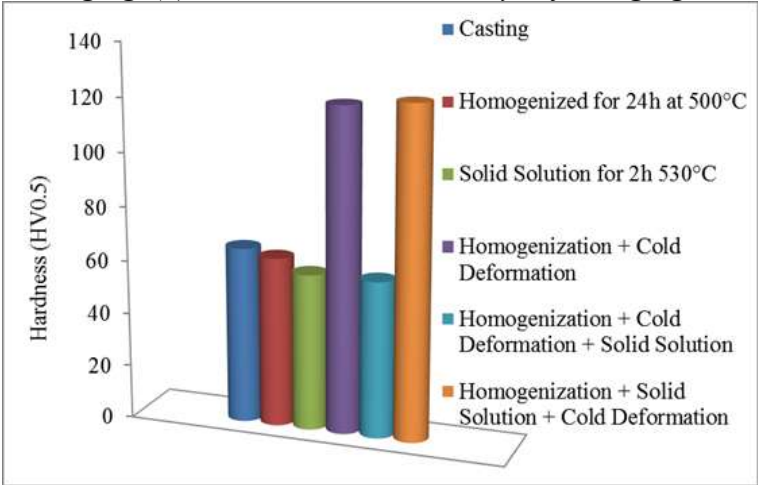
Figure 14 shows the SEM image and EDX analysis results of the 5083 Al–Bi alloy after thermomechanical treatment 2 (T2). The recrystallized structure is clearly formed at the grain boundaries and the banding of bright phases after deformation is observed at this stage. Here, phases 1-2-4 are Al₆(Mn,Fe,Bi) phases, 3 is the matrix, and phases 5-6 are Mg₂(Si,Bi) phase.

Vickers hardness test was performed to obtain information about the mechanical properties of the materials used in the experiment. The development process of mechanical properties was determined by taking hardness measurements at all processing stages. The hardness results of the 5083 as-cast aluminum alloy used in this study and the 5083 Al-Bi alloy with 1.2 % bismuth addition in the intermediate processing stages of aging are given in Figure 15.

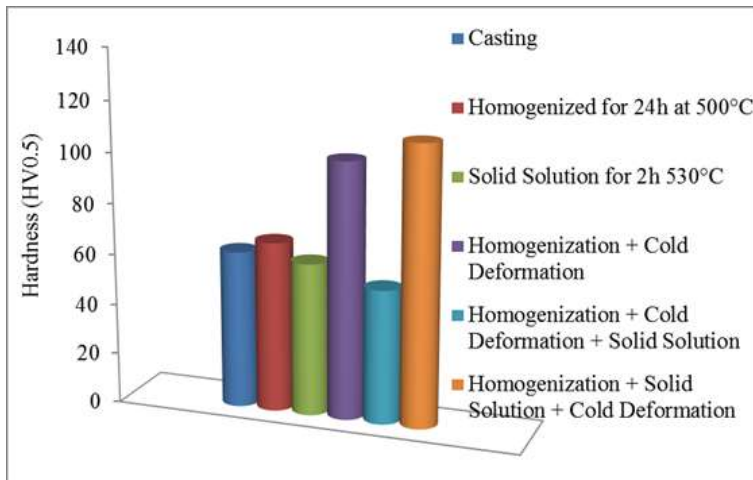
The hardness value of cast 5083 material was measured as 65.7 HV. While the hardness was measured as 63.2 HV after 24 hours of homogenization at 500°C, the Vickers hardness decreased to 58.3 HV after 2 hours of solution at 500°C. The casting hardness of 5083 Al-Bi alloy with 1.2 % Bismuth was measured as 62.1 HV, 67.1 HV after homogenization heat treatment, and 60.2 HV after solution taking. When the hardness values of 5083 aluminum alloy and 5083 Al-Bismuth Alloy are examined, the values are close to each other, and it is seen that the hardness value of AA 5083 alloy is slightly higher.

The effect of cold deformation on hardness is given (Figure 15). With cold deformation, there is a significant increase in the hardness of both materials and the hardness value has become twice the hardness value in the casting state. Although the AA 5083 alloy reaches slightly higher hardness values than the hardness of the 5083 Al-Bi alloy, it is concluded that there are no significant differences.

Figure 15. Hardness values of the (a) as-cast 5083 Al alloy before aging, (b) as-cast 5083 Al-Bi alloy before aging.



(a)



(b)

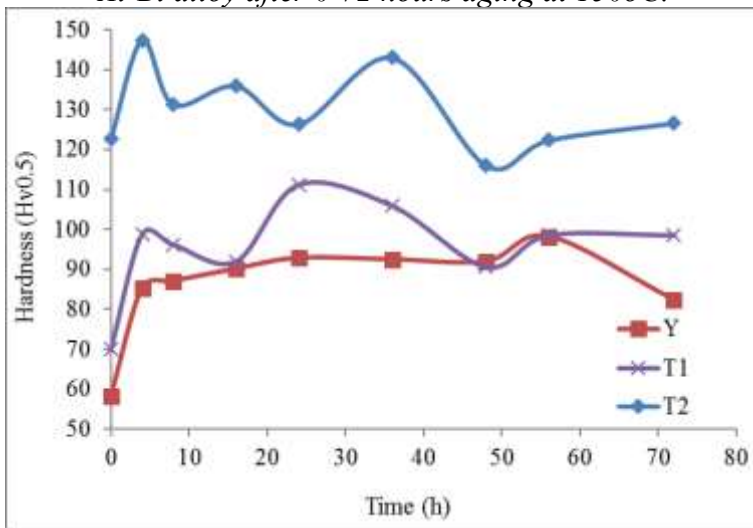
The results obtained by taking hardness measurements in every 0-4-8-16-24-32-48-56-72 hour periods of the materials that were aged for 0-72 hours at 150oC are shown in Figure 16. Normal aging, Thermomechanical process 1 and Thermomechanical process 2 peak hardness values were determined for both alloys. The determined peak hardness values were used as optimum parameters of the aging processes.

Looking at Figure 16. (a) for the 5083 alloy, it is seen that there is a sudden increase in hardness in the first 4 hours of aging for all stages (Y, T1 and T2) at a constant temperature of 150oC. In normal aging (Y), a steady increase in hardness was observed due to the increase in aging time and the peak hardness value was reached in 56 hours. Afterwards, a decrease in hardness value was observed. Thermomechanical process (T1) first decreased with the increase of aging time and then reached the peak hardness in 24 hours. As the aging time increased, the hardness decreased, increased, and decreased again, creating a zigzag appearance. A similar table is also seen in Thermomechanics 2 (T2). As the aging time increases, the hardness decreases up to 24 hours compared to the beginning, and the pig hardness value is reached in a shorter time than other

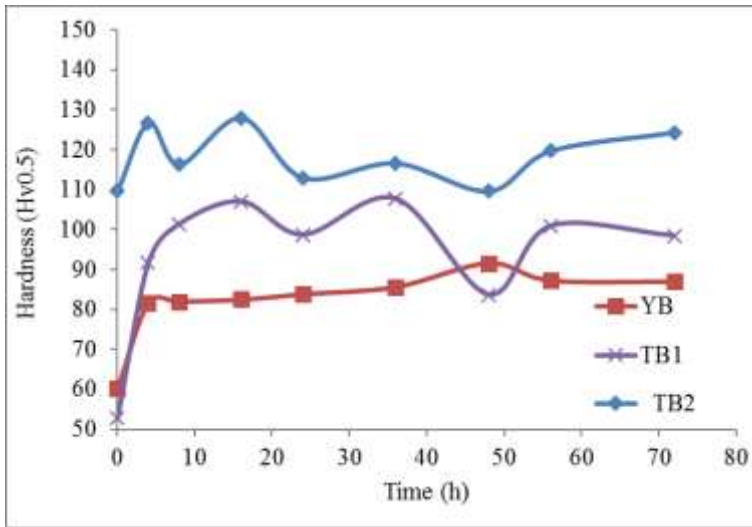
parameters such as 4 hours. As the aging time increased, the hardness decreased, moving away from the zigzag appearance that increased and decreased, and became stable. When the hardness values of thermomechanical processes were compared with the data measured with normal aging, it was seen that there was an increase in hardness.

Looking at the hardness graph of 5083 Al-Bi Alloy (Figure 16. b), for all parameters (Y, T1, T2), a sudden increase in hardness until 4 hours of aging, then a zigzag-looking hardness graph that decreases and increases again, is formed. In normal aging (Y) in 48 hours The peak hardness value was reached in 36 hours with thermomechanical process (T1) and in 16 hours with thermomechanical process 2 (T2).

Figure 16. Hardness values of As-cast (a) 5083 Al alloy, (b) 5083 Al-Bi alloy after 0-72 hours aging at 150oC.



(a)

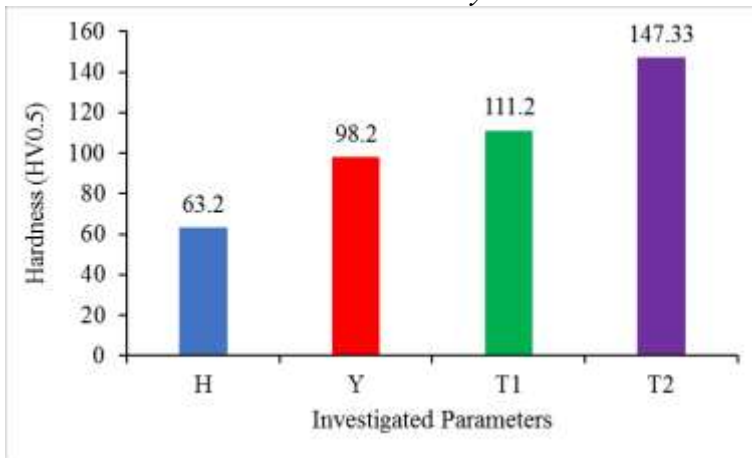


(b)

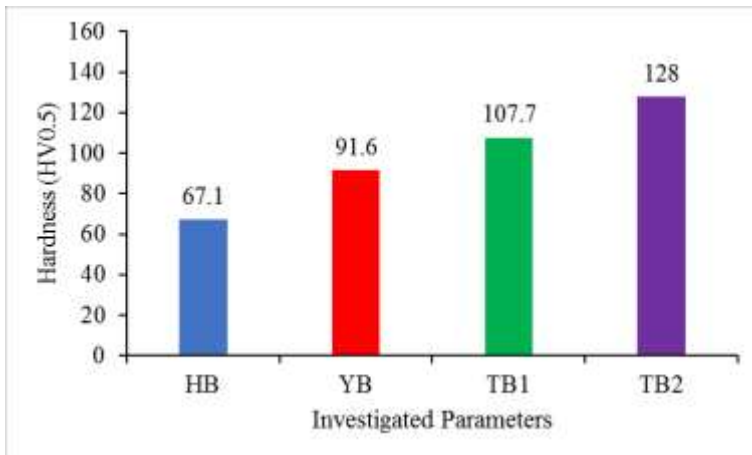
Maximum hardness values of 5083 Al and 5083 Al-Bi Alloy are given in Figure 17. Looking at the graph, it can be said that the Thermomechanical process increases the hardness and improves the mechanical properties. While the hardness of 5083 Al Alloy was 63.2 HV with homogenization, its hardness with normal aging was 98.2 HV, and it reached 111.2 HV with cold deformation + aging (T1). The highest hardness value of 147.33 HV was reached with cold deformation + aging (T2) after solution solution. In 5083 Al-Bi alloy, hardness increase was achieved with thermomechanical process and the highest hardness was reached with 128 HV in TB2 process.

When the hardness results are examined, it has been observed that cold deformation and thermomechanical treatment stages provide an increase in hardness in both materials, 5083 Al Alloy reaches a higher hardness value than Bismuth 5083 alloy, and peak hardness values are reached in shorter aging times in both alloys compared to the thermomechanical process parameters.

Figure 17. Peak hardness values of As-cast (a) 5083 Al alloy, (b) 5083 Al-Bi alloy.



(a)



(b)

C. N Panagopoulos and his friend E. P Georgiou examined the mechanical properties of commercial 5083 Al material by cold rolling at rates of 7% and 15% (Panagopoulos,& Georgiou, 2007: 161) (Panagopoulos,& Georgiou, 2009: 649). In their study, they demonstrated the effect of cold rolling on hardness by applying micro hardness tests on the surface of 5083 alloy. The hardness of 5083 materials, which were cold rolled at 0%, 5%, and 15%

respectively, were measured as 78HV-84HV-88HV. According to this result, they said that increasing the deformation range (from 0% to 15%) caused a significant increase in the hardness of the alloy. The reason for this increase is reduction of grain size of alloys: It is widely known that grain boundaries prevent dislocation movement and proliferation. According to the Hall–Petch equation (Dieter, 1988: 91), it is generally found that the yield strength (σ) of a metallic material increases with decreasing grain size.

Deformation hardening of the alloy: During forming processes of metallic materials, the number of dislocations per volume of material increases significantly (Callister, 1998: 80). Thus, the nucleation and movement of new dislocations are inhibited by existing dislocations, resulting in an increase in the hardness of this material.

In this study, the surface hardness of 5083 quality material as cast increased to twice the hardness level with 100% cold deformation. Looking at the studies in the literature, it has been shown that similar results were obtained, and that cold deformation applied to the 5083 alloy increased the hardness of the alloy. We can say that the hardness is increased by successfully applying the Thermomechanical process to 5083 Al material.

One of the reasons for the increase in hardness is the Thermomechanical processes applied. Maximum hardness was reached by aging heat treatment. As it is known, precipitation hardening is the process of precipitation of very small and hard second phases in the internal structure, which prevents dislocation movements and causes an increase in strength. These precipitates increase the strength of the material by preventing dislocations (Kayalı, 1991: 72) (Novikov, 2012:72) (Shan & Zhen, 2012: 267).

When looking at the microstructure of 5083 material in its cast state and after thermomechanical processes, it is seen that the

precipitated phases remain within the grain boundaries and are concentrated. These phases are thought to be Mg₂Si phases. Mg₂Si is an intermetallic compound and exhibits high melting temperature, low density, and high hardness (Li & et al. 2012: 5963). Hardness increases proportionally with this phase.

General Assessment

In this study, new generation 5083Al-Bi alloys were produced by adding 1.2% Bismuth to AA5083 Al alloy. The changes in the microstructure and hardness properties of these new generation Al alloys were examined by applying two different thermomechanical processes. The results from this study are listed as follows:

LOM and SEM analyses of the Homogenized, Aged and Thermomechanical processed alloys revealed that Al₆(Mn-Fe-Cr) and Al₆Mn, as well as the independently nucleated Mg₂Si phases, were formed in the matrixes with Fe and Mn rich content. The grains became thinner after the TMM process, and the Al₃Mg₂ phases nucleated.

According to the AGED process, while the highest hardness value was achieved in Al-Mg alloy in less time than Al-Mg-Bi1.3 alloy, this time was reduced even more with TMM processes due to 100% cold deformation. In comparison to the homogenized Al-Mg-Bi1.3 alloy's hardness, the ratio of hardness increased by 42% with aging and 66% with thermomechanical treatment.

Acknowledgement

This study was supported by Karabük University Scientific Research Projects Coordination with the project code FLY-2020-2261. The authors would like to thank the KBÜ-BAP unit for their financial support. They would also like to thank Medine Kılınç for her contributions.

REFERENCES

- Ahravci, C.A., ve Pekgülyüz, Ö. (1998) Calculation of phase diagrams for the metastable Al–Fe phases forming in direct-chill (DC)-cast aluminum alloy ingots. *Calphad*, 22:147–155. Doi: 10.1016/S0364-5916(98)00020-0
- Callister, W.D. (1998) *Materials science and engineering an introduction*. Wiley, New York, 163–5.
- Cleveland, R.M., Ghosh, A.K. and Bradley, J.R. (2003) Comparison of superplastic behavior in two 5083 aluminum alloys. *Mater. Sci. Eng.* 351(A):228-236. Doi: 10.1016/S0921-5093(02)00848-1
- Dieter, G.E. (1988) *Mechanical metallurgy*. McGraw-Hill, London, 189–91.
- Engler, O., Liu, Z. and Kuhnke, K. (2013) Impact of homogenization on particles in the Al-Mg-Mn alloy AA 5454: Experiment and simulation. *J. Alloys Comp.*, 560:111-122. Doi: 10.1016/j.jallcom.2013.01.163
- Engler, O., Heckelmann, I., Rickert, T., Hirsch, J. and Lücke, K. (1994) Effect of pretreatment and texture on recovery and recrystallization in Al-4.5Mg-0.7Mn alloy. *Mater.Sci. Tech.*,10 :7711-781. Doi: 10.1179/MST.1994.10.9.771
- Hollinshead, P.A. (1992) Effect of preheat treatment on ingot structure and recrystallization of brass component of rolling texture in hot rolled AA 5182. *Mater.Sci. Tech.* 8: 57-62. Doi: 10.1179/026708392790169795
- Iwasaki, H., Hosokawa, H., Mori, T., Tagata, T. and Higashi, K. (1998) Quantitative assessment of superplastic deformation behavior in a commercial 5083 alloy. *Mater.Sci. Eng.* 252(A):199-202. Doi: 10.1016/S0921-5093(98)00678-9
- Kayalı, E.S. (1991) *Metallere Plastik Şekil Verme İlke ve Uygulamaları*. İTÜ Yayınları, İstanbul.
- Li, Y. J., Zhang, W. Z, and Marthinsen, K. (2012) Precipitation Crystallography of Plate-shaped Al6(Mn, Fe) Dispersoids in AA5182

alloy. *Acta Materialia*, 60: 5963-5974. Doi: 10.1016/j.actamat.2012.06.022

Liu, Y.L., Kang, S.B. and Kim, H.W. (1999) The complex microstructures in an as-cast Al–Mg–Si alloy. *Mater Lett*, 41:267–72. Doi: 10.1016/S0167-577X(99)00141-X

Martinez, D. L. P. S., Verlinden, B. and Delaey, L. (1994) Hot workability of an Al–Mg alloy AA5182 with 1 wt.% Cu. *J. Mater. Sci.*, 29:6167–74. Doi: 10.1007/BF00354557

Mısırlı C. (2011) 5083 Kalite Alüminyum Alaşımının Homojenize Edilerek Sertlik Değerlerinin Ve Mikroyapılarının İncelenmesi. yüksek lisans tezi, Trakya Üniversitesi Fen Bilimleri Enstitüsü.

Mondolfo, L.F. (1976) *Aluminum alloys: structure and properties* 1st ed. Butter Worths, London.

Murray, J.L., McAlister, A.J., Schaefer, R.J., Bendersky, L.A., Biancaniello, F.S., Moffat, D.L. (1987) Stable and metastable phase equilibria in the Al–Mn system. *Metall Trans*, 18(A):385–392.

Nam, K.Y., Song, D.H., Lee, C.W., Lee, S.W., Park, Y.H. and Cho, K.M. (2006) Modification of Mg₂Si morphology in as-cast Mg–Al–Si alloys with strontium and antimony. *Mater. Sci. Forum*, 510 (511):238–41. Doi: 10.4028/www.scientific.net/MSF.510-511.238

Novikov, İ.İ. (2012) *Metallerin Isıl İşlem Teorisi, (1. Basımdan Çeviri)*, Ankara: Nobel Akademik Yayıncılık, Ankara.

Olaf E. and Simon M. (2001) *Control of second-phase particles in the Al-Mg-Mn alloy AA 5083 Hydro Aluminium Rolled Products*. Research and Development Bonn, P.O. Box 2468, D-53014, Germany.

Palasantzas, G. (2002) Electron beam induced oxidation of Al–Mg alloy surfaces. *Appl. Surf. Sci.*, 191:266–72. Doi: 10.1016/S0169-4332(02)00217-9

Panagopoulos, C.N. and Georgiou, E.P. (2007) Wear behaviour of 5083 wrought aluminium alloy under free corrosion conditions. *Tribol: Mater. Surf. Interf.*, 1:161–4. Doi: 10.1179/175158408X276259

Panagopoulos, C.N. and Georgiou, E.P. (2009) Surface mechanical behaviour of composite Ni–P–fly ash/zincate coated aluminium alloy. *Appl.Surf.Sci.*, 255: 649–503. Doi: 10.1016/j.apsusc.2009.02.026

Radeti, T., Popovi, M. and Romhanji, E. (2012) Microstructure evolution of a modified AA5083 aluminum alloy during a multistage homogenization treatment. *Mater. Char.*, 65:16-27. Doi: 10.1016/j.matchar.2011.12.006

Reddy, T.V.S., Dwivedi, D. and Jain N.K. (2009) Adhesive wear of stir cast hypereutectic Al–Si– Mg alloy under reciprocating sliding conditions. *Wear*, 266:1–5. Doi: 10.1016/j.wear.2008.05.003

Shan D, Zhen L. (2012) Aging behavior and microstructure evolution in the processing of aluminum alloys. In: Lin J, Balint D, Pietrzyk M (eds) *Microstructure evolution in metal forming processes*. Cambridge, UK: Woodhead Publishing, pp.267–297.

Sheppard, T. and Raghunathan, N. (1989) Modification of cast structures in Al-Mg alloys by thermal treatments. *Mater. Sci. Tech.*, 5: 268-280. Doi: 10.1179/mst.1989.5.3.

Srinivasan, A., Pilla, U.T.S. and Pai, B.C. (2010) Effects of elemental additions (Si and Sb) on the ageing behavior of AZ91 magnesium alloy. *Mater. Sci. Eng.*, 527(A) (24– 25):6543–50. Doi: 10.1016/j.msea.2010.07.020

Vetrano, J.S., Lavender, C.A., Hamilton, C.H., Smith, M.T. and Bruemmer, S.M. (1994) Superplastic behaviour in a commercial 5083-aluminum-alloy. *Scr. Metall.Mater.*, 30:565-570. Doi: 10.1016/S0921-5093(98)00678-9

CHAPTER 3

INVESTIGATION OF THE EFFECT OF THERMOMECHANICAL PROCESSES APPLIED TO 5083 QUALITY ALUMINUM ALLOY ON MICROSTRUCTURE AND HARDNESS PROPERTIES

1. Yavuz SUN¹

2. Hayrettin AHLATCI²

Giriş

Aluminum is the most abundant metal in the earth's crust. Aluminum, one of the most produced alloys among non-ferrous metals, has led to its use in many different application areas due to its superior properties. Apart from its superior properties, the easy availability of raw materials, advanced production techniques and cheapness are other reasons for its high consumption. Aluminum's ability to alloy with many metals enables it to obtain the necessary properties for special applications. One of the most important features of aluminum-based materials is that their density is low but

¹ Prof. Dr., Karabük University, Faculty of Engineering, Department of Metallurgy and Materials Engineering, Orcid: 0000-0002-7336-5591,

² Prof. Dr., Karabük University, Faculty of Engineering, Department of Metallurgy and Materials Engineering, Orcid: 0000-0002-6766-4974,

their strength/density ratio is high. The mechanical properties of metals depend on their microstructure, which in turn depends on the composition of the material, the solidification process, and the heat treatments and mechanical shaping processes applied after solidification. Aluminum alloys can be shaped more easily than other materials. Commercial pure aluminum is a light, ductile, soft material with high machinability and corrosion resistance. Although pure aluminum is a very soft material, its strength can be significantly increased by applying cold forming processes. Another way to increase strength is to alloy with elements such as magnesium, silicon, copper, zinc and manganese that can cause solid solution hardening (Mısırlı, 2011:97).

AA 5083 Aluminum alloy is an aluminum alloy containing 4-5 % Magnesium and some Manganese and Chromium additions. It is an alloy that can be hardened by alloying and cold working. For many applications, the alloy can be supplied in hot rolled coils in the 3–10 mm thickness range. For thinner applications, the material is cold rolled and optionally soft annealed. Most structural applications require sheet with good formability. However, under certain processing conditions, significant portions of the alloy have been observed to consist of grains that are considerably elongated in the rolling direction, with small recrystallized grains. This partially recrystallized structure, caused by the extremely high Mg and Cr contents of the alloy, is undesirable due to its negative effects on ductility and formability. It is well known that the application of a suitable homogenization cycle can strongly facilitate the recrystallization behavior of AA 5xxx series alloys (Sheppard & Raghunathan, 1989: 268) (Hollinshead, 1992: 57) (Engler & et al., 1994: 7711) (Radeti, Popovi & Romhanji, 2012: 16) (Engler, Liu & Kuhnke, 2013: 111) (Vetrano & et al., 1994: 565). This makes high-Mg AA 5xxx alloys recrystallized microstructures with fine grain sizes possible by a special thermo-mechanical process, making such

alloys suitable. The fine-grained alloy AA 5083 is the most used material in superplastic forming processes (Iwasaki & et al., 1998:199) (Cleveland, Ghosh & Bradley, 2003: 228).

In this study, new generation 5083Al-Bi alloys were produced by adding 1.2% Bismuth to AA5083 Al alloy. The changes in the microstructure and hardness properties of these new generation Al alloys were examined by applying two different thermomechanical processes.

Casting And Heat Treatment of AA5083 Quality Al Alloys

The 5083 Al alloy and the Bismuth added 5083 Aluminum alloy to be used in this study were produced in Karabük University, Metallurgical and Materials Engineering Casting laboratory (Figure 1.1).

Figure 1 (a) Induction furnace, (b) Atmosphere controlled gas equipments.



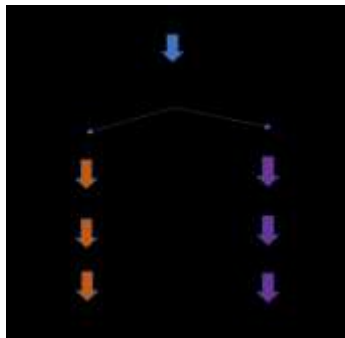
(a)

(b)

After casting, all samples were first homogenized in the Protherm Brand heat treatment furnace within Karabük University Metallurgy and Materials Laboratories. All experiments were continued on homogenized materials. Based on literature research, homogenization process was applied to 5083 Al and 1.2% Bi Added 5083 Al – Bi alloys with a 24-hour waiting period in the oven heated to 500oC.

The heat treatment and Thermomechanical process sequence to be applied after homogenization is shown as a diagram in Figure 2. Aging process was applied as a result of both methods called Thermomechanical 1 and Thermomechanical 2. The method in which cold rolling is applied after homogenization, then taken into solution and aged, is called Thermomechanical 1, and the method in which the materials that are homogenized and then taken into solution are aged after cold rolling is called Thermomechanical 2.

Figure 2. Applied thermomechanical process stages.



Two different temperatures were determined to apply the aging process under optimum conditions after the solution process. 8 different time periods such as 4h-8h-16h-24h-36h-42h-56h-72h were determined at low temperatures of 120oC and 150oC, and the aging process was carried out in the heat treatment furnace. has been implemented. The microstructure and hardness results of the samples aged for 4h-8h-16h-24h-36h-42h-56h-72h at 120oC and 150oC were analyzed. Considering the microstructure images and hardness results of the materials after aging at both temperatures, 150oC was determined as the optimum aging temperature. The subsequent experimental process was continued on materials aged at 150oC for periods of 4h-8h-16h-24h-36h-42h-56h-72h.

Before cold rolling, two test materials aged for 24 hours at 500 °C were prepared for Thermomechanical 1, and materials that

were put into solution at 530 °C for 2 hours were prepared for Thermomechanical 2. Before rolling, the materials were sanded with 400-600-800-1000-1200-2500 mesh to ensure surface smoothness. A specially made rolling device available at Karabük University Metallurgical and Materials Engineering was used as the rolling device (Figure 3.).

Figure 3. Cold rolling device used for rolling process.



Microstructural And Mechanical Characterization

Optical microscope (LOM), scanning electron microscope (SEM) were used for microstructure images of 5083 quality Aluminum alloy and 5083 AL-Bi alloy with 1.2 % Bismuth addition, and Energy Dispersive X-Ray (EDX) analysis was used for the determination of elements. X-Ray Diffraction Pattern (XRD) was performed to determine the phases, but no results were obtained because the phases in the structure were smaller than the diameter of the measurement probe.

Standard metallographic procedures were applied to obtain images under LOM and SEM. The samples were cut into 10 x 10 mm shapes and cold molded using a mixture of epoxy resin and hardener. The surfaces were sanded and polished and made ready for etching. A mixture of 25% hydrochloric acid (HCL) + 25% Nitric acid (HNO₃) + 25% hydrofluoric acid (HF) + 25% CH₃OH was used as etching acid, and after waiting for 10 seconds, the surface was cleaned with alcohol and dried. Microstructure images were

taken with a Nikon brand optical microscope and then images were taken with SEM and EDX analysis was performed.

In this review, XRD qualitative examinations were made of the 5083 quality and 5083 Al-Bi alloys that we produced and subjected to aging heat treatment. Examinations were made between 10 degrees and 90 degrees scanning angles on the Rigaku Ultima IV brand (Figure 4.). Since the diameter of the measurement probe was larger than the diameter of the phases, the phases could not be captured and a healthy data flow could not be received.

Figure 4. Rigaku Ultima IV X-Ray Diffraction Spectrometer.



Figure 5. Hardness Test Device.



Mechanical properties were determined by Vickers hardness measurements at room temperature. The hardness of the metallographically prepared samples was determined by the Vickers Hardness test on the Shimadzu brand HMV model device (Figure 5). In the experiment, hardness values were determined by using a pyramid-shaped penetrating tip and keeping it under a load of 0.5 Newton for 15 seconds and measuring the diagonal lengths of the

resulting trace. For each test sample, 10 measurements were made and the average value was taken for the result.

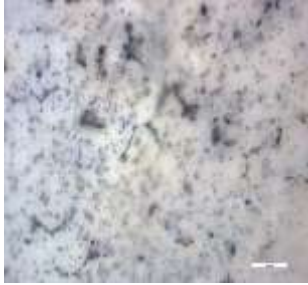
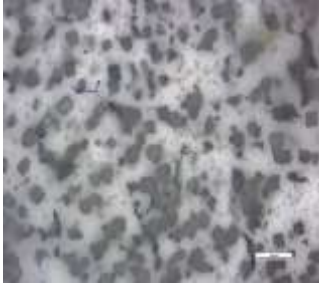
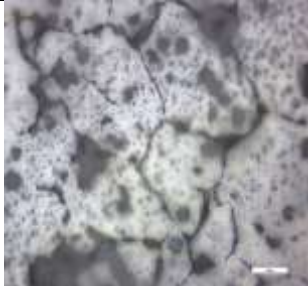
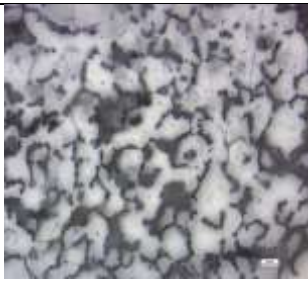
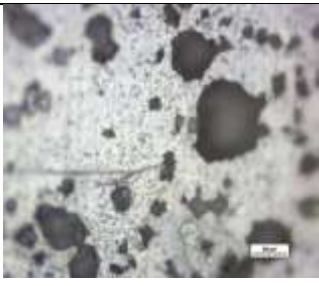
Characterization Results And Discussion

The chemical composition of 5083 quality aluminum according to BS EN 573-3:2009 standard, the chemical composition of cast AA5083 quality aluminum used in this study and cast 5083 aluminum alloys with 1.2% Bismuth addition, measured after spectral analysis, are given in Table 1. In the table, the chemical composition of BS EN 573-3:2009 AA 5083 quality material is given in comparison with the chemical composition of the casting 5083 alloy used in this study and the 5083 alloy with 1.2% Bismuth addition. According to these results, casting 5083 alloy production, which achieved standard material quality, was successfully carried out.

Table 1. Chemical compositions of cast 5083 Al and cast 5083 Al-Bi alloys.

Elements (%)	BS EN 573-3:2009 AA5083	As-cast AA5083	As-cast AA5083 Al-Bi
Al	-	95,40	95,16
Bi	-	0,002 den az	1,27
Mg	4,00-4,90	3,00	1,94
Mn	0,40-1,00	0,42	0,30
Fe	0,40	0,31	0,37
Si	0,0-0,40	0,32	0,33
Ti	0,05-0,25	0,029	0,03
Cr	0,05-0,25	0,10	0,12
Cu	0,10	0,27	0,30
Zn	0,0-0,10	0,08	0,10
Another	0,0-0,15	0,058	0,07

Table 2. Optical microscope images of 5083 Al and 1.2% Bismuth added 5083 Al-Bi alloy.

	5083	5083-Bi
Homogenized (H)		
Aged (Y)		
Thermo-mechanical Treatment 1 (T1)		
Thermo-mechanical Treatment 2 (T2)		

Microstructure analyzes were performed by looking at optical microscope images of 5083 Al and 5083 Al-Bi alloys at each process stage (homogenized, aged, thermomechanical process 1 and

thermomechanical process 2). Optical microscope images of all alloys are given in Table 2.

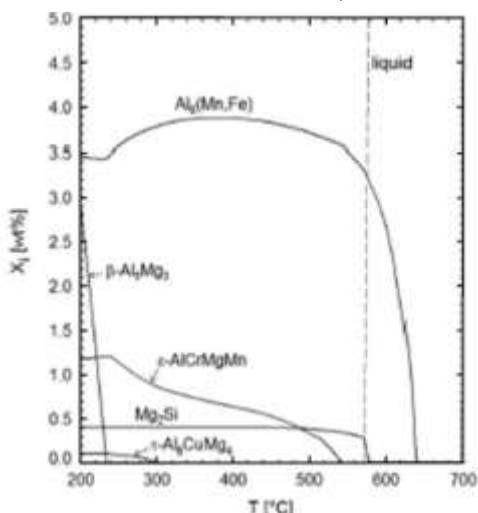
In the microstructure image of the homogenized 5083 Al material, it was seen that small blackish and gray particles of various sizes were distributed on the matrix. It can be said that grain boundaries begin to form in the microstructure with the aging process, and small particles scattered on the matrix are found both within the grain boundary and in the matrix. After homogenization, cold rolling was applied and in the microstructure image of the aged (T1) material, an image was captured in which there was an increase in the number of grain boundaries, capillary grain boundaries were formed and scattered small particles began to collect at the grain boundaries. After homogenization, it was taken into solution and cold rolled and aged. In the microstructure image of the material (T2), distinct grain boundaries were formed and the capillary grain boundaries turned into thick dark grain boundaries. In addition to the small particles within the grain boundary, the capillary grains seen in the previous microstructure remained between the grain boundaries.

When the optical microstructure images of 5083 Al-Bi Alloy with 1.2% Bismuth addition are examined; In the microstructure image of the homogenized 5083 Al-Bi alloy, a microstructure image like the 5083 Al material without Bismuth addition was detected. With the aging process, the grain boundaries began to form almost indistinctly. It is seen that in the thermomechanical process 1 (T1) microstructure, particles larger than the initial size of the black particles were formed, and the grain boundaries did not become very evident. Distinct dark grain boundaries were formed in the thermomechanical process 2 (T2) microstructure. At this stage, when the microstructures of 5083 Al and 5083 Al-Bi alloys were compared, it was observed that in the Bismuth material, the microstructure started to form late at the grain boundaries, and

distinct grain boundaries formed in Thermomechanical Process 2. The effect of this situation on the mechanical properties of the material can be associated with the hardness results.

In their study (Olaf & Simon, 2001: 100), Olaf Engler and Simon Miller-Jupp analyzed the phases formed in the structure by homogenization annealing of AA5083 material. Olaf and Simon, who applied homogenization annealing at low and high temperatures, used Calphad simulation to determine the phases. Calphad simulation uses a large database containing the 14 most important alloying elements of Al alloys (Cr, Cu, Fe, Mg, Mn, Ni, Si, etc.). Figure 6. shows the results of Calphad equilibrium simulations for the AA 5083 alloy in the form of the fraction of phases that emerge as a function of temperature. The scheme appears to be dominated by a Mn and Fe bearing phase called Al₆. According to Calphad simulations, Al₆(Mn, Fe) contains 14% Mn and 11% Fe plus a few tenths of a percent of both Mg and Cr, but no Si. They noted that the equilibrium simulations did not show the cubic α -Al (Fe, Mn) Si phase, which is common in 5xxx alloys, where the Mg₂Si phase is seen in the structure. Olaf Engler and Simon Miller-Jupp stated that the dark phases are Mg₂Si phases, and the bright phases contain Fe, Mn and Cr elements and are rich in Fe and Mn contents. They divided the bright phases into three different types. The bulkier luminous particles contain on average 12% Mn and 15% Fe, plus about 0.35% Cr, but almost no Si. Therefore, these particles are probably called Al₆(Mn, Fe) phases. Components containing Fe and Mn with more sculpted shapes were classified as the "Chinese script", particles containing slightly higher Mn and Fe, and particles containing small amounts of Cr and Si as the α -Al (Fe, Mn) Si phase. Occasionally, they observed small Cr-rich particles containing 5% Cr and about 10–15% both Mn and Mg, but no Fe. They defined these particles as ϵ -Al₁₈(Cr, Mn)₂Mg₃ phase.

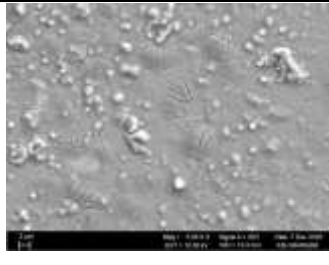
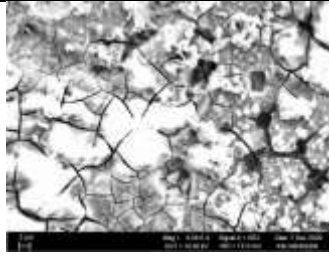
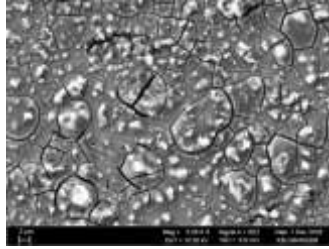
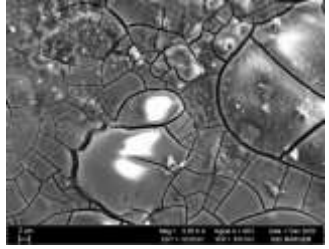
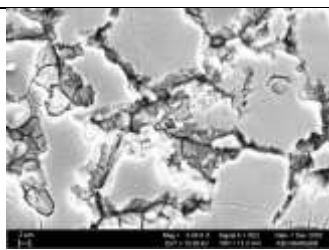
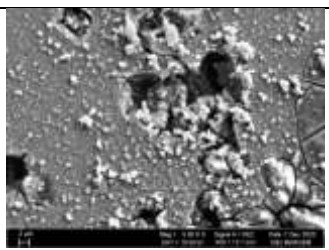
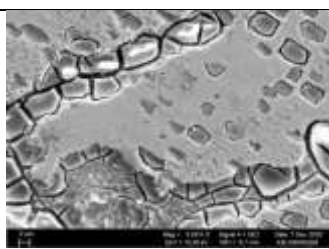
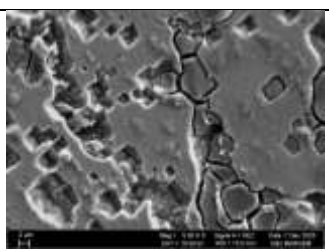
Figure 6. Calphad simulation results of AA5083 material (Olaf & Simon, 2001: 100).



The presence of dark and bright phases seen in the microstructure of 5083 Al and 5083 Al-Bi materials has similar results to the work of Olaf Engler and Simon Miller-Jupp. Microstructure images of 5083 Al and 5083 Al-Bi alloys were taken under a scanning electron microscope (SEM). SEM images of 5083 AL Alloy and 5083 Al-Bi Alloy are given in Table 3.

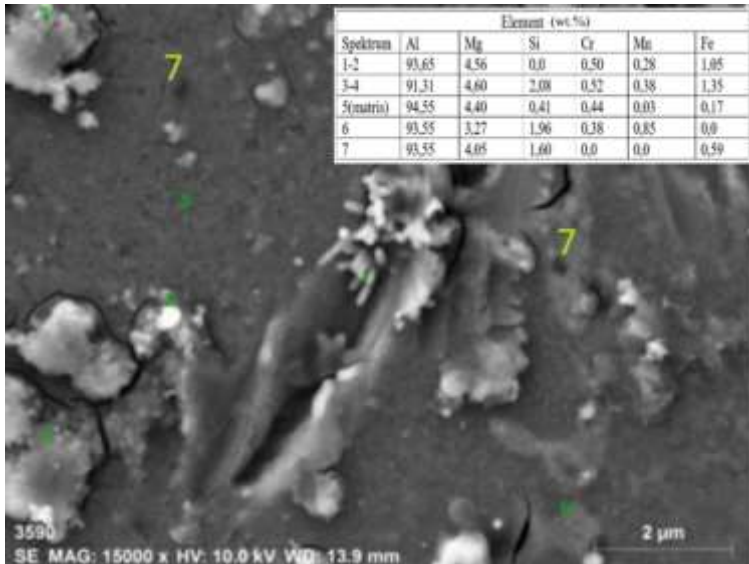
When the SEM Images of 5083Al and 5083 Al-Bi Alloys are examined in Table 3, 5083 Al material gives a smoother microstructure image than 5083 Al-Bi material. Smooth structure means regular particle distribution. In 5083 Al-Bi material, the excessive concentration of bright phases in one place and their absence in other places can be given as an example of this situation. We can tell the effect of the Bi plugin on this situation by looking at EDX analysis. In SEM images, while the presence of bright phases is more in the image after Homogeneous and aging in both materials, with the Thermomechanical Process these phases turn gray and the presence of dark phases begins to increase. It can be seen that especially the recrystallized phases are dark colored phases.

Table 3. SEM images of 5083 Al and 5083 Al-Bi alloy with 1.2% Bismuth addition.

	5083	5083-Bi
Homogenized (HB)		
Aged (YB)		
Thermo-mechanical Treatment 1 (TB1)		
Thermo-mechanical Treatment 2 (TB2)		

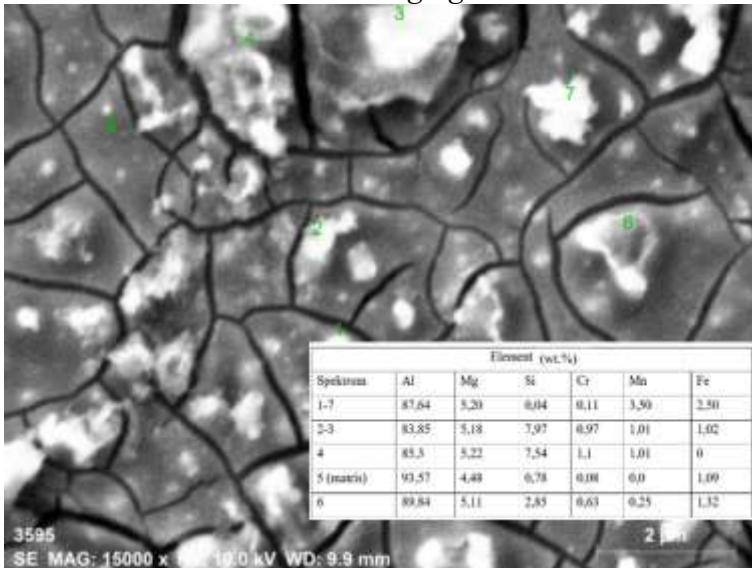
After the SEM images of the examined alloys were taken, EDX analyzes were examined to get an idea about the elemental analysis by weight in the microstructure. EDX results of 5083 Al alloys are given in Figures 7-10.

Figure 7. SEM image and EDX results of 5083 Al alloy after homogenization heat treatment.



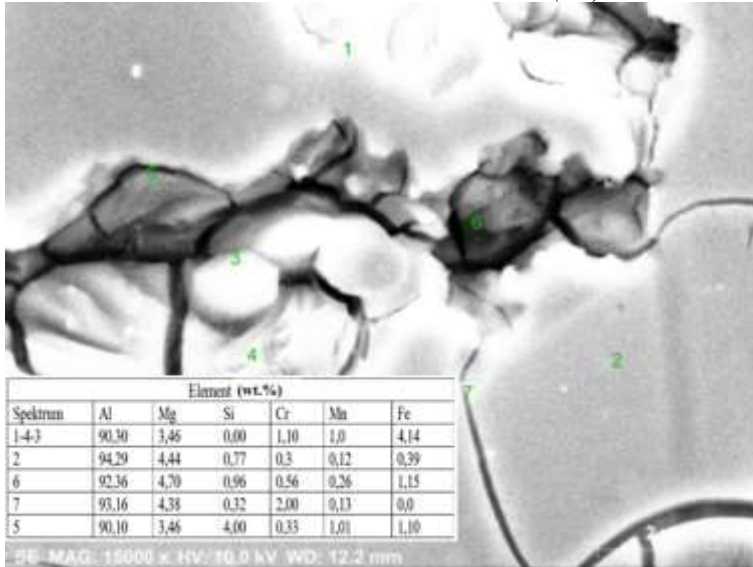
In Figure 7, shows the SEM image and EDX analysis results of 5083 Al material after homogenization (H). Since the phases marked 1 and 2 are Fe and Mn-rich, Si-free and bright phases, it can be said that they fully comply with the phase definition (Olaf & Simon, 2001: 100) in the work of Olaf Engler and Simon Miller-Jupp, and this phase is AL6 (Mn, Fe). The area marked 3-4 is again a bright phase and due to its rich silica content, these phases are thought to be α -Al (Fe, Mn) Si. Phase 5 is the matrix and phase 6 is the Fe-free Cr-rich ϵ -Al18 (Cr, Mn)₂ Mg₃ phase. Phase number 7 is the dark phase and is rich in Mg₂Si.

Figure 8. SEM image and EDX results of 5083 Al alloy after normal aging.



In Figure 8. SEM image and EDX analysis results of 5083 Al material after normal aging (Y) are given. It can be said that phases 1-7 are the bright $Al_6(Mn, Fe)$ phase and are widely found in the structure with the aging heat treatment. Region number 5 is matrix, region number 2 and 3 is $\alpha-Al (Fe, Mn) Si$, phase number 6 is Mg_2Si phase, and phase number 4 is $\epsilon-Al_{18}(Cr, Mn)_2 Mg_3$ phase. In the SEM image of 5083 material after aging, it is seen that the bright $Al_6(Mn, Fe)$ phase dominates the structure and this phase is distributed heterogeneously within the grain boundaries formed by aging. The commonly found $Al_6(Mn, Fe)$ phase can be defined as the constituent phase.

Figure 9. SEM image and EDX results of 5083 Al alloy after thermomechanical treatment 1 (T1).



In Figure 9. SEM image and EDX analysis results of 5083 Al material after T1 are given. With the effect of cold deformation, where the bright phases numbered 1-3-4 are Al₆(Mn, Fe), this phase spreads into the structure by showing banding, including grain boundaries and grain interiors. It seems to cover everything. It can be said that the dark phase number 6 is Mg₂Si, phase number 2 is the matrix, and phase number 7 is ε-Al₁₈(Cr,Mn)₂ Mg₃. Phase number 5 is the α-Al (Fe, Mn) Si phase.

Figure 10. SEM image and EDX results of 5083 Al alloy after thermomechanical treatment 2 (T2).

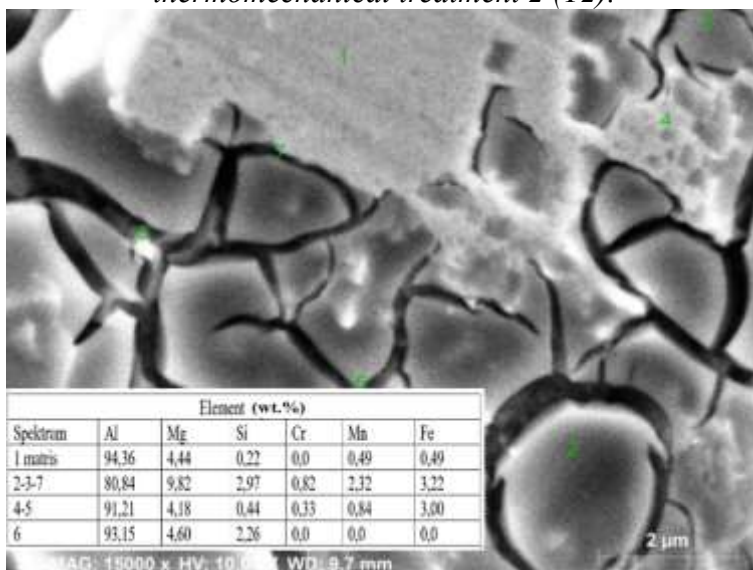


Figure 10 shows the SEM image and EDX analysis results of 5083 Al material after Thermomechanical Process 2 (T2). It can be said that phases 4 and 5 are the $Al_6(Mn, Fe)$ constituent phase. This phase spread into the structure under the effect of rolling without entering the grain boundaries. At the grain boundaries, there is a gray phase $\alpha-Al (Fe, Mn) Si$ phase with recrystallized structure numbered 2-3-7. Phase 6 is the Mg_2Si phase.

EDX results of 5083 Al-Bi alloys are given in Figures 11-14. The effect of the addition of 1.2 % bismuth on the phases can be interpreted using these figures.

Figure 11. SEM image and EDX results of 5083 Al-Bi alloy after homogenization.

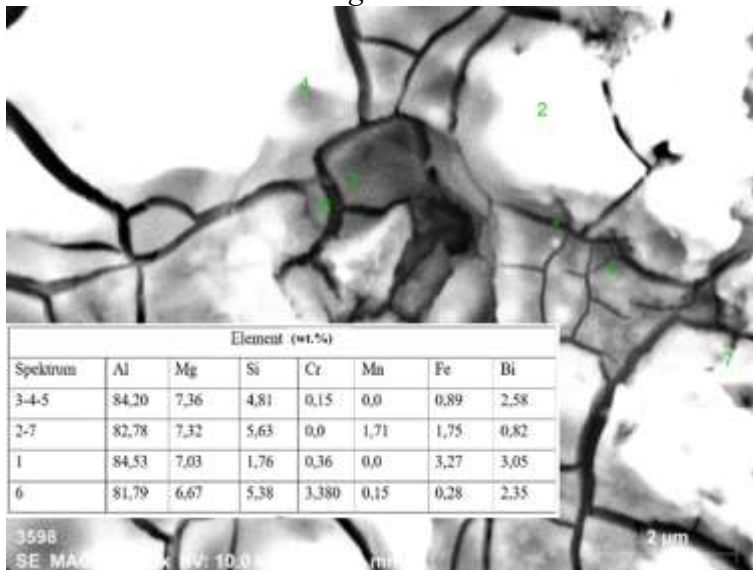


Figure 11 shows the SEM image and EDX analysis results of the 5083 Al-Bi alloy after homogenization. Phases 3-4-5 are Mg₂Si phase. Mg₂Si is one of the important reinforcement phases in magnesium alloy to improve thermal stability and high temperature properties due to its high melting point, high hardness, and low expansion coefficient (Palasantzas, 2002: 266) Palasantzas, G. (2002) (Martinez, Verlinden & Delaey, 1994: 6167) (Liu, Kang & Kim, 1999: 267) (Mondolfo, 1976: 100). However, due to the uneven distribution and irregular shape of the conventional Mg₂Si phase, it is very detrimental to the mechanical properties of the alloy. Therefore, what is necessary to strengthen Mg₂Si and increase its effect is to control its morphology and size (Ahravci & Pekkülyüz, 1998: 147). The most common modification process is to add modifying elements during the melting process (Murray & et al., 1987: 385). Addition of alloying elements is the easiest and most effective method to improve the mechanical and wear properties of alloys (Reddy, Dwivedi & Jain, 2009: 1) (Nam & et al., 2006: 238).

Sb, Ca, Bi, Pb, Ti, Zn and Zr are some of the alloying elements added to Mg alloys. The added alloying elements either dissolve or form compounds within the microstructure (Srinivasan & et al., 2010: 6543).

The addition of 1.2% Bismuth to the structure of the 5083 Al-Bi alloy was added with the expectation of minimizing the negative effects of Mg₂Si. Therefore, we can say that phase 3-4-5 is the Mg₂(Si, Bi) phase. Contrary to the SEM image of the 5083 alloy, the 5083 alloy with Bismuth addition revealed more bright phases. If we interpret this situation, it can be said that the dark gray phases tend to decrease as the addition of bismuth takes up space in volume.

In SEM and EDX analyzes of 5083 Al-Bi alloy after homogenization, it can be said that the phases marked with numbers 2-7 are α-Al (Fe, Mn, Bi) Si, phase number 1 is Al₆ (Mn, Fe, Bi) and phase number 6 is matrix.

Figure 12. SEM image and EDX results of 5083 Al-Bi alloy after normal aging.

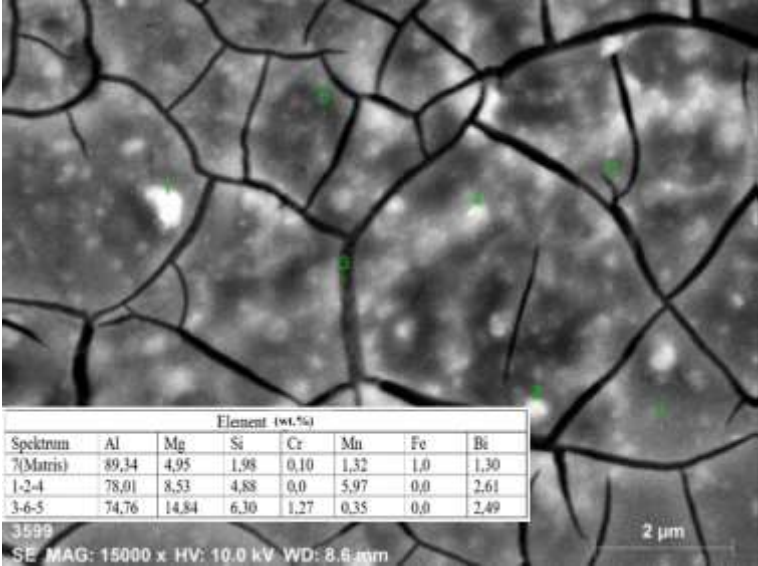


Figure 12 shows the SEM image and EDX analysis results of 5083 Al-Bi material after aging. Two distinct phases emerged in this

SEM image. These are Mg₂Si and Al₆(Mn,Fe) phases, which we call the constituent phases. Phases 1-2-4 show the Al₆(Mn, Fe, Bi) phase with the addition of bismuth to the component, and phases 3-6-5 show the Mg₂(Si, Bi) phase. Phase number 7 is the matrix.

Figure 13. SEM image and EDX results of 5083 Al-Bi alloy after thermomechanical treatment 1 (T1).

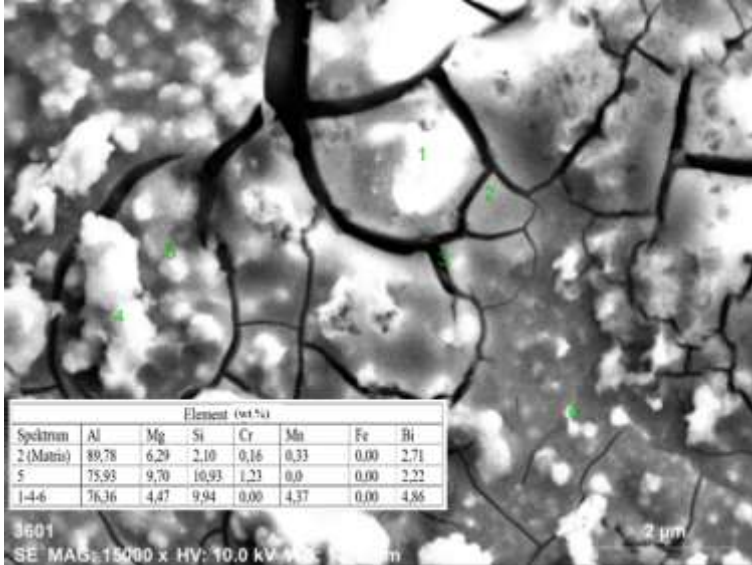


Fig.13. shows the SEM image and EDX analysis results of 5083 Al–Bi alloy after thermomechanical treatment 1 (TB1) are given. When we compare the SEM images of 5083 Bi-free and containing alloys, it can be said that the band-like structure resulting from rolling does not form in the TB1 stage in the Bismuth 5083 alloy, and the bright phases that were suppressed during aging become evident. The Fe percentage of these bright phases is zero, and they are phases with a high Si proportion. Although it is not appropriate to describe the previous constituent phases here due to the lack of Fe ratio, since the presence of bismuth addition takes up space in volume, it can be said that the Fe phases did not disappear from the structure and the constituent phases are fixed here as well.

Therefore, we can define phases 1-4-6 as Al₆(Mn,Bi). 2 matrix is 5 Mg₂(Si,Bi) phase.

Figure 14. SEM image and EDX results of 5083 Al-Bi alloy after thermomechanical treatment 2 (T2).

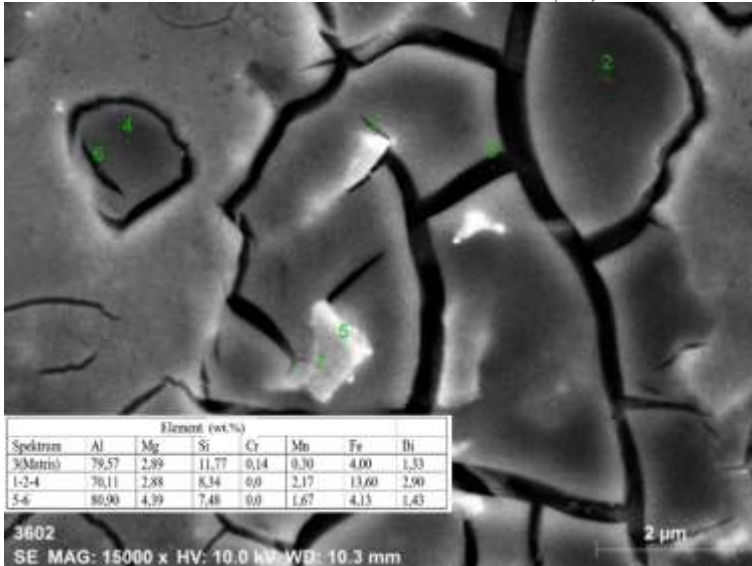


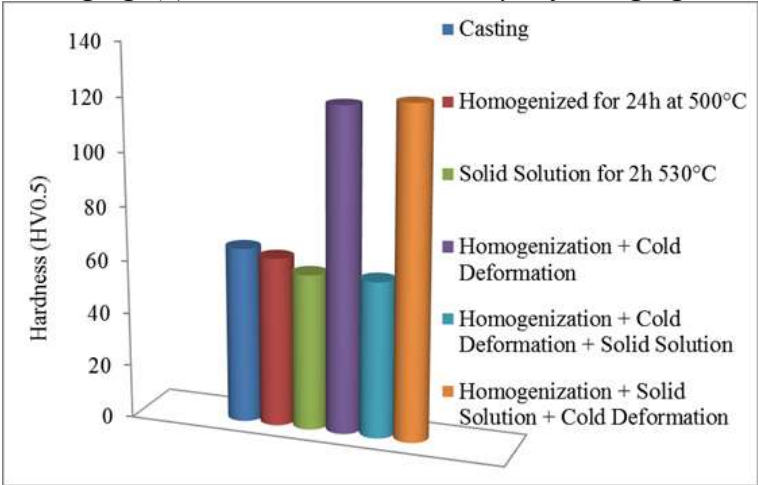
Figure 14 shows the SEM image and EDX analysis results of the 5083 Al–Bi alloy after thermomechanical treatment 2 (T2). The recrystallized structure is clearly formed at the grain boundaries and the banding of bright phases after deformation is observed at this stage. Here, phases 1-2-4 are Al₆(Mn,Fe,Bi) phases, 3 is the matrix, and phases 5-6 are Mg₂(Si,Bi) phase.

Vickers hardness test was performed to obtain information about the mechanical properties of the materials used in the experiment. The development process of mechanical properties was determined by taking hardness measurements at all processing stages. The hardness results of the 5083 as-cast aluminum alloy used in this study and the 5083 Al-Bi alloy with 1.2 % bismuth addition in the intermediate processing stages of aging are given in Figure 15.

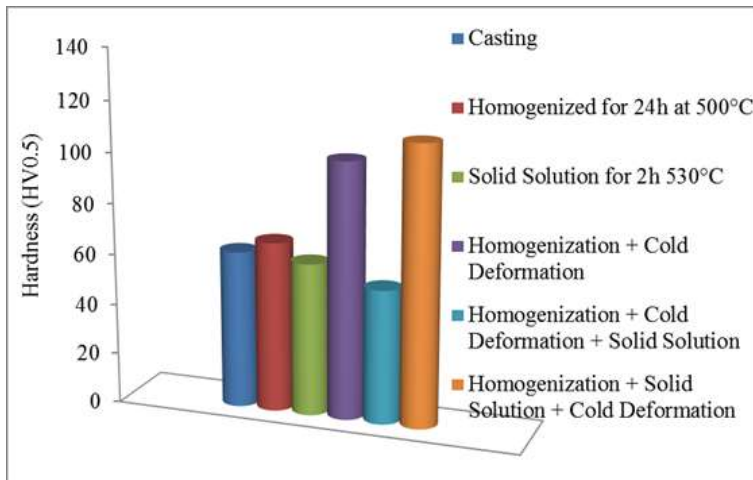
The hardness value of cast 5083 material was measured as 65.7 HV. While the hardness was measured as 63.2 HV after 24 hours of homogenization at 500oC, the Vickers hardness decreased to 58.3 HV after 2 hours of solution at 500oC. The casting hardness of 5083 Al-Bi alloy with 1.2 % Bismuth was measured as 62.1 HV, 67.1 HV after homogenization heat treatment, and 60.2 HV after solution taking. When the hardness values of 5083 aluminum alloy and 5083 Al-Bismuth Alloy are examined, the values are close to each other, and it is seen that the hardness value of AA 5083 alloy is slightly higher.

The effect of cold deformation on hardness is given (Figure 15). With cold deformation, there is a significant increase in the hardness of both materials and the hardness value has become twice the hardness value in the casting state. Although the AA 5083 alloy reaches slightly higher hardness values than the hardness of the 5083 Al-Bi alloy, it is concluded that there are no significant differences.

Figure 15. Hardness values of the(a) as-cast 5083 Al alloy before aging, (b) as- cast 5083 Al-Bi alloy before aging.



(a)



(b)

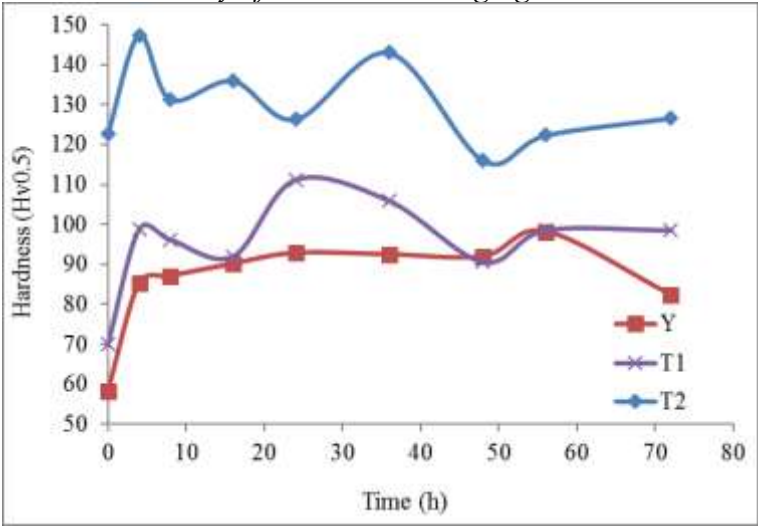
The results obtained by taking hardness measurements in every 0-4-8-16-24-32-48-56-72 hour periods of the materials that were aged for 0-72 hours at 150oC are shown in Figure 16. Normal aging, Thermomechanical process 1 and Thermomechanical process 2 peak hardness values were determined for both alloys. The determined peak hardness values were used as optimum parameters of the aging processes.

Looking at Figure 16. (a) for the 5083 alloy, it is seen that there is a sudden increase in hardness in the first 4 hours of aging for all stages (Y, T1 and T2) at a constant temperature of 150oC. In normal aging (Y), a steady increase in hardness was observed due to the increase in aging time and the peak hardness value was reached in 56 hours. Afterwards, a decrease in hardness value was observed. Thermomechanical process (T1) first decreased with the increase of aging time and then reached the peak hardness in 24 hours. As the aging time increased, the hardness decreased, increased, and decreased again, creating a zigzag appearance. A similar table is also seen in Thermomechanics 2 (T2). As the aging time increases, the hardness decreases up to 24 hours compared to the beginning, and the pig hardness value is reached in a shorter time than other

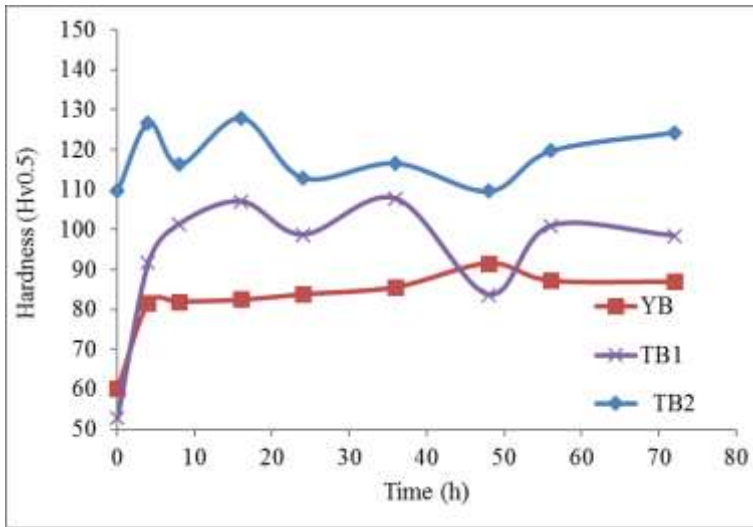
parameters such as 4 hours. As the aging time increased, the hardness decreased, moving away from the zigzag appearance that increased and decreased, and became stable. When the hardness values of thermomechanical processes were compared with the data measured with normal aging, it was seen that there was an increase in hardness.

Looking at the hardness graph of 5083 Al-Bi Alloy (Figure 16. b), for all parameters (Y, T1, T2), a sudden increase in hardness until 4 hours of aging, then a zigzag-looking hardness graph that decreases and increases again, is formed. In normal aging (Y) in 48 hours The peak hardness value was reached in 36 hours with thermomechanical process (T1) and in 16 hours with thermomechanical process 2 (T2).

Figure 16. Hardness values of As-cast (a) 5083 Al alloy, (b) 5083 Al-Bi alloy after 0-72 hours aging at 150oC.



(a)

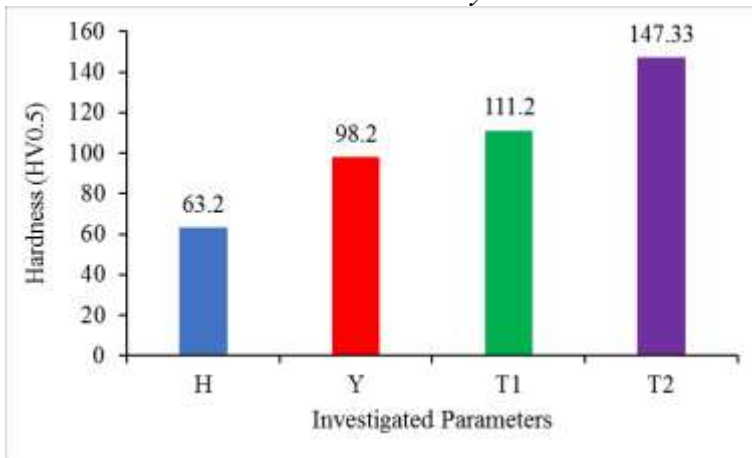


(b)

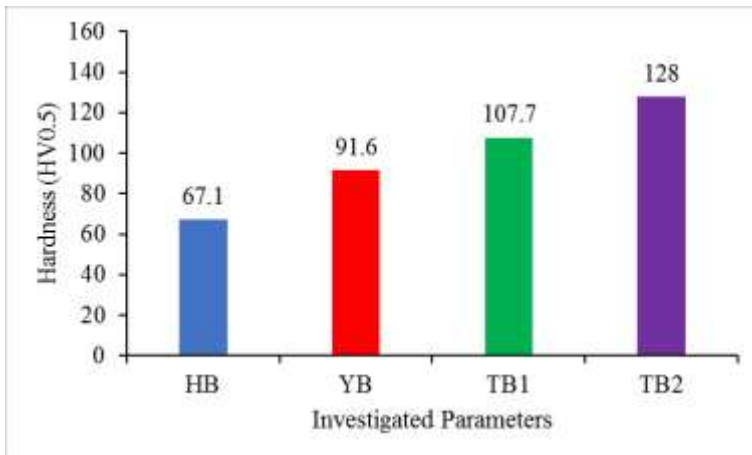
Maximum hardness values of 5083 Al and 5083 Al-Bi Alloy are given in Figure 17. Looking at the graph, it can be said that the Thermomechanical process increases the hardness and improves the mechanical properties. While the hardness of 5083 Al Alloy was 63.2 HV with homogenization, its hardness with normal aging was 98.2 HV, and it reached 111.2 HV with cold deformation + aging (T1). The highest hardness value of 147.33 HV was reached with cold deformation + aging (T2) after solution solution. In 5083 Al-Bi alloy, hardness increase was achieved with thermomechanical process and the highest hardness was reached with 128 HV in TB2 process.

When the hardness results are examined, it has been observed that cold deformation and thermomechanical treatment stages provide an increase in hardness in both materials, 5083 Al Alloy reaches a higher hardness value than Bismuth 5083 alloy, and peak hardness values are reached in shorter aging times in both alloys compared to the thermomechanical process parameters.

Figure 17. Peak hardness values of As-cast (a) 5083 Al alloy, (b) 5083 Al-Bi alloy.



(a)



(b)

C. N Panagopoulos and his friend E. P Georgiou examined the mechanical properties of commercial 5083 Al material by cold rolling at rates of 7% and 15% (Panagopoulos,& Georgiou, 2007: 161) (Panagopoulos,& Georgiou, 2009: 649). In their study, they demonstrated the effect of cold rolling on hardness by applying micro hardness tests on the surface of 5083 alloy. The hardness of 5083 materials, which were cold rolled at 0%, 5%, and 15%

respectively, were measured as 78HV-84HV-88HV. According to this result, they said that increasing the deformation range (from 0% to 15%) caused a significant increase in the hardness of the alloy. The reason for this increase is reduction of grain size of alloys: It is widely known that grain boundaries prevent dislocation movement and proliferation. According to the Hall–Petch equation (Dieter, 1988: 91), it is generally found that the yield strength (σ) of a metallic material increases with decreasing grain size.

Deformation hardening of the alloy: During forming processes of metallic materials, the number of dislocations per volume of material increases significantly (Callister, 1998: 80). Thus, the nucleation and movement of new dislocations are inhibited by existing dislocations, resulting in an increase in the hardness of this material.

In this study, the surface hardness of 5083 quality material as cast increased to twice the hardness level with 100% cold deformation. Looking at the studies in the literature, it has been shown that similar results were obtained, and that cold deformation applied to the 5083 alloy increased the hardness of the alloy. We can say that the hardness is increased by successfully applying the Thermomechanical process to 5083 Al material.

One of the reasons for the increase in hardness is the Thermomechanical processes applied. Maximum hardness was reached by aging heat treatment. As it is known, precipitation hardening is the process of precipitation of very small and hard second phases in the internal structure, which prevents dislocation movements and causes an increase in strength. These precipitates increase the strength of the material by preventing dislocations (Kayalı, 1991: 72) (Novikov, 2012:72) (Shan & Zhen, 2012: 267).

When looking at the microstructure of 5083 material in its cast state and after thermomechanical processes, it is seen that the

precipitated phases remain within the grain boundaries and are concentrated. These phases are thought to be Mg₂Si phases. Mg₂Si is an intermetallic compound and exhibits high melting temperature, low density, and high hardness (Li & et al. 2012: 5963). Hardness increases proportionally with this phase.

General Assessment

In this study, new generation 5083Al-Bi alloys were produced by adding 1.2% Bismuth to AA5083 Al alloy. The changes in the microstructure and hardness properties of these new generation Al alloys were examined by applying two different thermomechanical processes. The results from this study are listed as follows:

LOM and SEM analyses of the Homogenized, Aged and Thermomechanical processed alloys revealed that Al₆(Mn-Fe-Cr) and Al₆Mn, as well as the independently nucleated Mg₂Si phases, were formed in the matrixes with Fe and Mn rich content. The grains became thinner after the TMM process, and the Al₃Mg₂ phases nucleated.

According to the AGED process, while the highest hardness value was achieved in Al-Mg alloy in less time than Al-Mg-Bi1.3 alloy, this time was reduced even more with TMM processes due to 100% cold deformation. In comparison to the homogenized Al-Mg-Bi1.3 alloy's hardness, the ratio of hardness increased by 42% with aging and 66% with thermomechanical treatment.

Acknowledgement

This study was supported by Karabük University Scientific Research Projects Coordination with the project code FLY-2020-2261. The authors would like to thank the KBÜ-BAP unit for their financial support. They would also like to thank Medine Kılınç for her contributions.

REFERENCES

- Ahravci, C.A., ve Pekgülyüz, Ö. (1998) Calculation of phase diagrams for the metastable Al-Fe phases forming in direct-chill (DC)-cast aluminum alloy ingots. *Calphad*, 22:147-155. Doi: 10.1016/S0364-5916(98)00020-0
- Callister, W.D. (1998) *Materials science and engineering an introduction*. Wiley, New York, 163-5.
- Cleveland, R.M., Ghosh, A.K. and Bradley, J.R. (2003) Comparison of superplastic behavior in two 5083 aluminum alloys. *Mater. Sci. Eng.* 351(A):228-236. Doi: 10.1016/S0921-5093(02)00848-1
- Dieter, G.E. (1988) *Mechanical metallurgy*. McGraw-Hill, London, 189-91.
- Engler, O., Liu, Z. and Kuhnke, K. (2013) Impact of homogenization on particles in the Al-Mg-Mn alloy AA 5454: Experiment and simulation. *J. Alloys Comp.*, 560:111-122. Doi: 10.1016/j.jallcom.2013.01.163
- Engler, O., Heckelmann, I., Rickert, T., Hirsch, J. and Lücke, K. (1994) Effect of pretreatment and texture on recovery and recrystallization in Al-4.5Mg-0.7Mn alloy. *Mater.Sci. Tech.*,10 :7711-781. Doi: 10.1179/MST.1994.10.9.771
- Hollinshead, P.A. (1992) Effect of preheat treatment on ingot structure and recrystallization of brass component of rolling texture in hot rolled AA 5182. *Mater.Sci. Tech.* 8: 57-62. Doi: 10.1179/026708392790169795
- Iwasaki, H., Hosokawa, H., Mori, T., Tagata, T. and Higashi, K. (1998) Quantitative assessment of superplastic deformation behavior in a commercial 5083 alloy. *Mater.Sci. Eng.* 252(A):199-202. Doi: 10.1016/S0921-5093(98)00678-9
- Kayalı, E.S. (1991) *Metallere Plastik Şekil Verme İlke ve Uygulamaları*. İTÜ Yayınları, İstanbul.
- Li, Y. J., Zhang, W. Z, and Marthinsen, K. (2012) Precipitation Crystallography of Plate-shaped Al6(Mn, Fe) Dispersoids in AA5182

alloy. *Acta Materialia*, 60: 5963-5974. Doi: 10.1016/j.actamat.2012.06.022

Liu, Y.L., Kang, S.B. and Kim, H.W. (1999) The complex microstructures in an as-cast Al–Mg–Si alloy. *Mater Lett*, 41:267–72. Doi: 10.1016/S0167-577X(99)00141-X

Martinez, D. L. P. S., Verlinden, B. and Delaey, L. (1994) Hot workability of an Al–Mg alloy AA5182 with 1 wt.% Cu. *J. Mater. Sci.*, 29:6167–74. Doi: 10.1007/BF00354557

Mısırlı C. (2011) 5083 Kalite Alüminyum Alaşımının Homojenize Edilerek Sertlik Değerlerinin Ve Mikroyapılarının İncelenmesi. yüksek lisans tezi, Trakya Üniversitesi Fen Bilimleri Enstitüsü.

Mondolfo, L.F. (1976) *Aluminum alloys: structure and properties* 1st ed. Butter Worths, London.

Murray, J.L., McAlister, A.J., Schaefer, R.J., Bendersky, L.A., Biancaniello, F.S., Moffat, D.L. (1987) Stable and metastable phase equilibria in the Al–Mn system. *Metall Trans*, 18(A):385–392.

Nam, K.Y., Song, D.H., Lee, C.W., Lee, S.W., Park, Y.H. and Cho, K.M. (2006) Modification of Mg₂Si morphology in as-cast Mg–Al–Si alloys with strontium and antimony. *Mater. Sci. Forum*, 510 (511):238–41. Doi: 10.4028/www.scientific.net/MSF.510-511.238

Novikov, İ.İ. (2012) *Metallerin Isıl İşlem Teorisi, (1. Basımdan Çeviri)*, Ankara: Nobel Akademik Yayıncılık, Ankara.

Olaf E. and Simon M. (2001) *Control of second-phase particles in the Al-Mg-Mn alloy AA 5083 Hydro Aluminium Rolled Products*. Research and Development Bonn, P.O. Box 2468, D-53014, Germany.

Palasantzas, G. (2002) Electron beam induced oxidation of Al–Mg alloy surfaces. *Appl. Surf. Sci.*, 191:266–72. Doi: 10.1016/S0169-4332(02)00217-9

Panagopoulos, C.N. and Georgiou, E.P. (2007) Wear behaviour of 5083 wrought aluminium alloy under free corrosion conditions. *Tribol: Mater. Surf. Interf.*, 1:161–4. Doi: 10.1179/175158408X276259

Panagopoulos, C.N. and Georgiou, E.P. (2009) Surface mechanical behaviour of composite Ni–P–fly ash/zincate coated aluminium alloy. *Appl.Surf.Sci.*, 255: 649–503. Doi: 10.1016/j.apsusc.2009.02.026

Radeti, T., Popovi, M. and Romhanji, E. (2012) Microstructure evolution of a modified AA5083 aluminum alloy during a multistage homogenization treatment. *Mater. Char.*, 65:16-27. Doi: 10.1016/j.matchar.2011.12.006

Reddy, T.V.S., Dwivedi, D. and Jain N.K. (2009) Adhesive wear of stir cast hypereutectic Al–Si– Mg alloy under reciprocating sliding conditions. *Wear*, 266:1–5. Doi: 10.1016/j.wear.2008.05.003

Shan D, Zhen L. (2012) Aging behavior and microstructure evolution in the processing of aluminum alloys. In: Lin J, Balint D, Pietrzyk M (eds) *Microstructure evolution in metal forming processes*. Cambridge, UK: Woodhead Publishing, pp.267–297.

Sheppard, T. and Raghunathan, N. (1989) Modification of cast structures in Al-Mg alloys by thermal treatments. *Mater. Sci. Tech.*, 5: 268-280. Doi: 10.1179/mst.1989.5.3.

Srinivasan, A., Pilla, U.T.S. and Pai, B.C. (2010) Effects of elemental additions (Si and Sb) on the ageing behavior of AZ91 magnesium alloy. *Mater. Sci. Eng.*, 527(A) (24– 25):6543–50. Doi: 10.1016/j.msea.2010.07.020

Vetrano, J.S., Lavender, C.A., Hamilton, C.H., Smith, M.T. and Bruemmer, S.M. (1994) Superplastic behaviour in a commercial 5083-aluminum-alloy. *Scr. Metall.Mater.*, 30:565-570. Doi: 10.1016/S0921-5093(98)00678-9

CHAPTER 4

CORROSION PERFORMANCE AND H₂ EVOLUTION OF AS-CAST AND EXTRUDED MG– 2ZN–1Y–0.5X (X = GD, LA, ZR, AG, CA) ALLOYS IN SIMULATED PHYSIOLOGICAL CONDITIONS

KENZA DJEBARI¹
YUNUS TÜREN²
HAYRETTİN AHLATÇI³
LEVENT ELEN⁴

Introduction

For successful bone healing, it is essential to provide firm stabilization of fractures to prevent even minor movements under physiological loading. Inflammatory reactions can disrupt the healing process, making high biocompatibility a crucial requirement for implant materials. Owing to their superior strength and

¹ Dr. Kenza DJEBARI, Karabük University, Department of Metallurgical and Materials Engineering, Orcid: 0000-0003-0158-4741

² Prof. Dr. Yunus TÜREN, Necmettin Erbakan University, department of Mechanical Engineering, Orcid: 0000-0001-8755-1865

³ Prof. Dr. Hayrettin AHLATCI, Karabük University, Department of Metallurgical and Materials Engineering, Orcid: 0000-0002-6766-4974

⁴ Ass. Prof. Levent ELEN, Karabük University, Department of Metallurgical and Materials Engineering, Orcid: 0000-0001-8740-7900

toughness, metals remain the materials of choice in load-bearing biomedical applications. Currently, stainless steels, titanium alloys, and cobalt-chromium-based systems are widely used due to their favorable corrosion resistance and long-term mechanical stability within the human body. Nonetheless, prolonged presence of these implants may provoke persistent irritation, chronic inflammation, or the release of harmful ions, all of which pose significant health risks (JACOBS et al., 1998; Jacobs et al., 2003; Lhotka et al., 2003).

Additionally, these materials exhibit mechanical mismatches with native bone, particularly in terms of elastic modulus. This discrepancy causes stress shielding, an effect that inhibits natural bone remodeling, potentially resulting in localized bone resorption or secondary fractures (Böstman et al., 2000; Nagels et al., 2003). Another drawback is their non-degradability. In short-term treatments like fracture fixation, such implants often necessitate a second surgery for removal post-healing, which increases the risk, pain, and financial burden for patients. These limitations have driven considerable research interest in the development of biodegradable implants that can gradually degrade *in vivo* while synchronously supporting tissue recovery.

An ideal biodegradable implant should demonstrate a degradation profile that parallels tissue regeneration, gradually losing mechanical integrity as the surrounding tissue regains its functional capacity.

Magnesium as a Biodegradable Implant Material

While current biodegradable systems include resorbable polymers and bioceramics, their mechanical inadequacies (e.g., low strength for polymers and brittleness for ceramics) often render them unsuitable for load-bearing applications (Hou et al., 2014). In contrast, biodegradable metals, particularly magnesium (Mg) and iron (Fe)-based alloys, offer promising solutions. However, optimal

systems that exhibit the required combination of mechanical strength, degradation rate, and biocompatibility are still under development. Magnesium and its alloys have recently emerged as attractive candidates in this field (Persaud-Sharma & McGoron, 2012; Staiger et al., 2006; Witte, 2010), particularly in orthopedic applications, such as bone plates and fixation screws, as well as in cardiovascular applications, including stents.

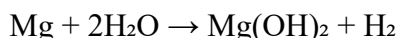
Several intrinsic characteristics make magnesium highly suitable for temporary biomedical use:

1. **Biodegradability:** Magnesium and its alloys are inherently susceptible to corrosion in aqueous environments, particularly those containing chloride ions, making them naturally degradable in physiological conditions (Kraus et al., 2012; Witte et al., 2006)). Compared to Fe-based alloys, Mg degrades at a more favorable rate for short-term applications.
2. **Biocompatibility:** Mg demonstrates excellent biological compatibility. Released Mg^{2+} ions are naturally involved in metabolic processes and, to date, have not been associated with toxic effects at clinically relevant concentrations (L. Li et al., 2004; Maguire & Cowan, 2002).
3. **Mechanical Compatibility:** The elastic modulus of magnesium (~40–45 GPa) is closer to that of cortical bone (3–20 GPa), which significantly minimizes the stress shielding effect compared to conventional implant metals such as stainless steel (~200 GPa), cobalt-chromium alloys (~230 GPa), or titanium alloys (~115 GPa) (Tsakiris et al., 2021).
4. **Low Density:** Magnesium alloys are among the lightest structural metals (1.74–2.0 g/cm³), closely approximating the

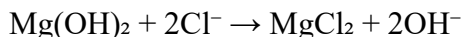
density of natural bone (1.8–2.1 g/cm³), and substantially lower than that of titanium-based biomaterials (4.4–4.5 g/cm³), thereby contributing to reduced implant weight (Tsakiris et al., 2021).

Magnesium Biodegradation in Physiological Conditions

Electrochemical reactions govern the degradation of magnesium in aqueous and physiological environments. In the presence of water, magnesium undergoes corrosion through a redox reaction, forming magnesium hydroxide (Mg(OH)₂) and releasing hydrogen gas (K. Chen et al., 2015; Mueller et al., 2010):



This reaction forms a magnesium hydroxide layer on the surface, which offers only partial protection against further degradation. In environments containing chloride ions, especially when concentrations exceed 30 mmol/L, the protective layer is compromised. Magnesium hydroxide reacts with chloride to produce soluble magnesium chloride (MgCl₂), eliminating the barrier effect (Staiger et al., 2006):



Given that the chloride concentration in human body fluids is approximately 150 mmol/L, the protective Mg(OH)₂ film rapidly dissolves, exposing the bare Mg surface and facilitating continued corrosion (Witte et al., 2006, 2008).

The byproduct hydroxide ions cause a localized pH increase near the implant, which can impact surrounding tissues (Wong et al., 2010). Additionally, body fluids contain calcium and phosphate ions that react with Mg²⁺ to form complex mineral phases such as calcium magnesium phosphate or calcium phosphate, which contribute to surface layer formation and can partially inhibit corrosion and stabilize pH (Jang et al., 2013).

Organic components in physiological fluids, such as proteins, biomolecules, and even cells or bacteria, also affect magnesium's corrosion behavior. Protein adsorption onto the Mg surface can form a biofilm that initially reduces corrosion rates (Yamamoto & Hiromoto, 2009). However, this effect is time-dependent; in some cases, proteins later promote degradation instead of inhibiting it. These biological interactions play a significant role in reducing degradation rates observed in vivo compared to those in vitro, emphasizing the importance of evaluating both protein and cellular interactions on implant degradation (Agha et al., 2016)

Despite these protective or mitigating effects, such interactions can disturb the local equilibrium at the implantation site, further complicating the corrosion environment. The degradation behavior of Mg is highly context-dependent, not only varying across anatomical locations and individual patients but also evolving over time (Y.-C. Tang et al., 2006). Studies show that the degradation rate tends to be high in the initial stages of implantation and decreases with time as a more stable corrosion product layer forms (H. Wang & Shi, 2011; Witte et al., 2005).

Beyond chemical degradation, mechanical loading introduces further complexity. Magnesium implants are subjected to significant forces, such as the 3500 N load experienced by the human spine during regular activity, or the high-frequency cyclic loads on cardiovascular stents due to heartbeats (Singh Raman & Choudhary, 2013). These combined chemical and mechanical stresses make magnesium implants vulnerable to corrosion fatigue (CF) and stress corrosion cracking (SCC) (Kannan, 2010; Silcock, 1982). Hydrogen gas released during corrosion can promote cracking mechanisms by diffusing into the metal, weakening its structure over time (Gu et al., 2010; Jafari et al., 2015).

Challenges in the Application of Biodegradable Magnesium Implants

Magnesium and its alloys are up-and-coming candidates for use in temporary, load-bearing implants due to their excellent degradability, favorable biocompatibility, and mechanical compatibility with bone tissue (Radha & Sreekanth, 2017). However, their practical application faces several hurdles that must be overcome before clinical implementation.

The most significant limitation lies in the rapid corrosion of Mg in physiological environments, which are chemically complex and rich in water, oxygen, proteins, chloride ions, and other reactive species (Alvarez-Lopez et al., 2010; Z. Li et al., 2008). This accelerated degradation occurs primarily due to the conversion of $\text{Mg}(\text{OH})_2$ into the highly soluble MgCl_2 in the presence of high chloride concentrations, which are typical of body fluids (G. L. Song & Atrens, 1999). This poses three main problems:

1. **Mechanical Degradation:** Rapid corrosion compromises the implant's structural integrity before tissue healing is complete. The formation of localized pits due to the interaction of chloride ions with anodically dissolved Mg ions increases local stress concentrations and fosters crack formation (Gonzlez et al., 2013).
2. **Hydrogen Evolution:** Corrosion of Mg also releases hydrogen gas, which can accumulate around the implant, forming gas pockets that hinder tissue integration and may even result in necrosis due to tissue separation (Liu & Schlesinger, 2009; Seal et al., 2009; Witte et al., 2005).
3. **Local Alkalinization:** As Mg dissolves, hydroxide ions are released, increasing the local pH around the implant. Although systemic regulation tends to maintain overall pH

balance, the immediate environment of the implant may experience alkalinity that interferes with biochemical processes and, in extreme cases, causes alkaline toxicity if pH exceeds 7.8 (Ng et al., 2010; G. Song & Song, 2007).

To address these issues, it is essential to develop Mg alloys with controlled corrosion behavior that retain sufficient mechanical performance for the whole bone healing period—ranging from 4 to 16 weeks depending on fracture complexity, tissue damage, and patient-specific factors ((Frost HM,. 1989;268). Ideally, the implant should fully degrade after the tissue has healed, eliminating the need for a second surgical procedure.

Structural Innovations in Magnesium-Based Biodegradable Alloys

Recent advancements in alloy development have focused on tailoring the microstructure of magnesium-based materials to optimize their in vivo performance. Structural modifications, such as grain refinement, phase control, and porosity engineering, have been explored to enhance mechanical and corrosion properties.

Grain Refinement

Reducing the grain size of Mg alloys increases the grain boundary area, which helps to minimize mechanical discontinuity between the metal matrix and the oxide layer formed during corrosion. This improves the layer's adherence and reduces cracking, thereby enhancing corrosion resistance (Birbilis et al., 2010; Orlov et al., 2011). Numerous studies have confirmed that alloying combined with thermo-mechanical processing methods such as extrusion or rolling can modify the morphology and distribution of secondary phases, which in turn influence electrochemical behavior (Pu et al., 2011; Rosalbino et al., 2013; Witte, 2010).

Through grain refinement, not only are corrosion properties improved, but also mechanical parameters such as yield strength (YS), ultimate tensile strength (UTS), and ductility. These enhancements are critical to ensuring the mechanical reliability of the implant during the bone regeneration process.

Strategies to Enhance the Biodegradation Behavior of Magnesium

Various techniques have been investigated to regulate the degradation rate of magnesium (Mg) in physiological environments. Among these, purification, alloying, and surface modifications have shown the most promise. High-purity magnesium exhibits significantly reduced corrosion rates; however, its inherently low yield strength restricts its utility in orthopedic or other load-bearing applications (G. Song & Song, 2007).

To overcome this, alloying Mg with appropriate elements can improve both corrosion resistance and mechanical strength. Nevertheless, the inclusion of alloying elements brings challenges related to biocompatibility, as these elements dissolve into body fluids during corrosion, their cytotoxic potential and long-term biological impacts must be carefully evaluated (Deng et al., 2016). Additionally, many Mg-based alloys suffer from inhomogeneous microstructures, which lead to localized corrosion and compromise structural integrity over time (Kannan, 2010).

Magnesium's highly electronegative nature (-2.4 V vs. SHE) also limits the ability of alloying alone to reduce degradation rates significantly. In response to these issues, alloy systems like Mg–Zn–Y have been extensively explored for their balanced mechanical and corrosion properties, making them promising for both structural and biomedical applications.

Existing research on Mg–Zn–Y alloys has focused on their as-cast, thermally treated, and plastically deformed microstructures, and how these affect mechanical performance (T. J. Chen et al., 2013). However, key knowledge gaps remain. For example, optimal compositions for achieving specific property targets have not been fully defined, and the effect of ternary equilibrium phases—such as the I-phase ($\text{Mg}_3\text{Zn}_6\text{Y}$), W-phase ($\text{Mg}_3\text{Zn}_3\text{Y}_2$), and Z- or X-phase (Mg_{12}ZnY)—on performance is still under investigation (T. J. Chen et al., 2013; Huang et al., 2009). Notably, the I- and Z-phases exhibit strong bonding with the Mg matrix, which inhibits dislocation movement and thereby improves alloy strength.

Despite this promise, Mg–Zn–Y alloys remain underexplored as biodegradable implant materials, highlighting a compelling direction for future studies.

Toward Clinically Relevant Magnesium Alloys

The optimization of Mg alloys for implant use involves a triad of goals:

- Electrochemical stability, to ensure controlled and homogeneous degradation;
- Mechanical performance, targeting strength and ductility appropriate for orthopedic demands;
- Biocompatibility, ensuring minimal cytotoxicity and immunological response.

Thermomechanical treatments, such as extrusion, rolling, or forging, have been shown to refine the grain structure, thereby enhancing both mechanical strength and corrosion resistance. These methods can increase tensile strength by up to 300% (Bommala et al., 2019) and simultaneously slow the corrosion rate while reducing

hydrogen gas evolution, making them essential tools in the design of next-generation implants (Tsakiris et al., 2021).

Precipitation hardening plays a central role in mechanical improvement, as many strengthening elements show reduced solubility in Mg at lower temperatures, promoting precipitate formation (T. J. Chen et al., 2013). In this context, various alloying elements offer unique advantages:

- Zinc (Zn): Enhances strength via solid solution and precipitation strengthening, and helps mitigate the effect of impurities like Ni and Fe. While essential for metabolism and immune function, excess Zn (>2 wt%) may cause casting defects and neurotoxicity.
- Lanthanum (La): Enhances mechanical strength and corrosion resistance, thereby improving ductility and plasticity. However, La may accumulate in soft tissues and bones, raising concerns about long-term toxicity.
- Calcium (Ca): A highly biocompatible addition that promotes grain refinement, stabilizes corrosion-resistant surface layers, and enhances both thermal and mechanical stability. Ca levels in the body are tightly regulated, making it ideal for medical use.
- Zirconium (Zr): Functions primarily as a grain refiner, improving structural uniformity and corrosion behavior. It is non-toxic at low concentrations and particularly suitable for Al-free medical-grade Mg alloys.
- Gadolinium (Gd): Forms corrosion-resistant intermetallics and improves mechanical performance by enhancing strength and creep resistance. While Gd³⁺ ions are toxic in excess, their risk in implants is minimal if degradation is well-controlled.

- Silver (Ag): Provides both antibacterial and strengthening effects. It promotes passivation but must be carefully dosed to avoid galvanic corrosion and cytotoxicity. In small amounts, Ag is safe and useful in preventing implant-related infections (Djebari et al., 2025; Qian & Das, 2006a).

Extrusion: A Key Process for Functional Enhancement

Among processing techniques, extrusion plays a vital role in improving the performance of biodegradable Mg alloys. It refines the microstructure, reduces grain size, and promotes the formation of beneficial crystallographic textures, such as basal texture, which helps resist corrosion (SHIRI et al., 2022; Zhang et al., 2013). Increasing the extrusion ratio typically results in improved corrosion resistance and enhanced mechanical properties. Furthermore, extrusion aids in uniformly distributing alloying elements and reinforcing phases such as hydroxyapatite (HA), enhancing both corrosion behavior and biocompatibility (Kiani et al., 2023; Walker et al., 2012).

To study the in vitro corrosion behavior of Mg alloys, researchers frequently use simulated body fluids such as Hank's Balanced Salt Solution (HBSS). This medium closely mimics the ionic composition of human plasma, including sodium, potassium, calcium, magnesium, bicarbonate, and phosphate ions. Its buffering capacity maintains physiological pH, allowing for a more realistic estimation of the corrosion rate and degradation products of biodegradable metals under simulated physiological conditions. The presence of chloride ions in Hank's solution also ensures that corrosion behavior observed in vitro closely parallels the aggressive in vivo environment. However, due to the absence of proteins and living cells, in vitro tests in Hank's solution may still differ significantly from the actual biological scenario. (Hao et al., 2022; Xin et al., 2010).

In this context, the present chapter investigates the corrosion performance and hydrogen evolution behavior of as-cast and extruded Mg–2Zn–1Y–0.5X alloys, where X represents selected biocompatible elements including Gd, La, Zr, Ag, and Ca. The aim is to evaluate the influence of alloying and extrusion on corrosion kinetics in simulated physiological environments through a combination of potentiodynamic polarization, immersion testing, and hydrogen evolution measurements. By comparing the degradation behavior before and after extrusion, this study seeks to elucidate the relationship between microstructural characteristics, phase distribution, and corrosion mechanisms. These findings will contribute to the development of advanced Mg-based orthopedic implants with optimized structural integrity and degradation profiles tailored to the clinical requirements of temporary bone fixation systems.

Materials and Methods

The experimental alloys were synthesized using high-purity (99.9 wt.%) magnesium, silver, and zinc, supplemented with master alloys containing Mg–20 wt.% Gd, Mg–30 wt.% Ca, and elemental additions of La, Zr, and Y. All metallic constituents were procured from BDM Bilginoglu, 4D Machine and Technology, and Nanography Nano Technology Inc. Alloy fabrication was conducted in an induction furnace equipped with atmospheric control to ensure process stability. The melting and mold preheating temperatures were set at 750 °C and 300 °C, respectively, and maintained using precision-regulated heating plates. Casting was performed via gravity-assisted solidification in a steel permanent mold, while oxidation during the process was suppressed by a protective gas mixture comprising CO₂ and 1 vol.% SF₆. A zirconia-based ceramic foam filter was installed within the runner system to refine the casting quality further and reduce the presence of non-metallic inclusions.

A homogenization heat treatment was conducted following the casting process to minimize casting-related imperfections, including localized grain size variations and elemental segregation. The cast ingots were individually wrapped in aluminum foil and embedded in an SiO₂ and graphite sand insulating medium to ensure uniform heat distribution and prevent surface oxidation. Homogenization annealing was performed at 430 °C for 48 hours. Upon completion of the thermal cycle, the samples were rapidly quenched in water to retain the homogenized microstructure and inhibit phase redistribution.

Hot extrusion of the alloys was performed using a 30-ton capacity hydraulic press. Cylindrical billets were sectioned from the cast ingots at the 35 mm diameter region and machined to 32 mm diameter to ensure dimensional accuracy and surface uniformity before extrusion. To reduce friction and thermal degradation during the process, a heat-resistant MoS₂-based spray lubricant (Molykote) was applied to the surfaces of the billet, die, and punch. The extrusion was conducted at a temperature of 400 °C. The die blocks were preheated using clamping-type heaters, with temperature regulation achieved through a dedicated control unit integrated into the press system. The billets were also preheated to the target extrusion temperature in a furnace. To minimize thermal losses, billets were retained in the furnace for 15 minutes after reaching the set temperature before being transferred to the die. An infrared laser thermometer was used to monitor the billet and die temperatures regularly, ensuring thermal consistency. Once the desired temperature was stabilized, the punch advanced at a constant rate of 0.3 mm/s to extrude the billets, which measured 32 mm in diameter and 50 mm in height. The extrusion process yielded rectangular bars with final dimensions of 20 × 20 × 105 mm. The extrusion ratio (EO) was determined before the process, calculated using the formula provided in Equation

$$EO=A_0 / A_s$$

By Equation 1, A_0 denotes the initial cross-sectional area of the billet, while A_s represents the cross-sectional area of the extruded sample. In this study, all billets used in the hot extrusion process were cylindrical with a diameter of 32 mm. The resulting extruded bars had rectangular cross-sections with dimensions of 20 × 20 mm and a length of 105 mm. Based on these dimensions, the calculated extrusion ratio was approximately 2.24:1. This ratio quantifies the extent of cross-sectional area reduction, reflecting the degree of plastic deformation imposed on the billet during the extrusion process.

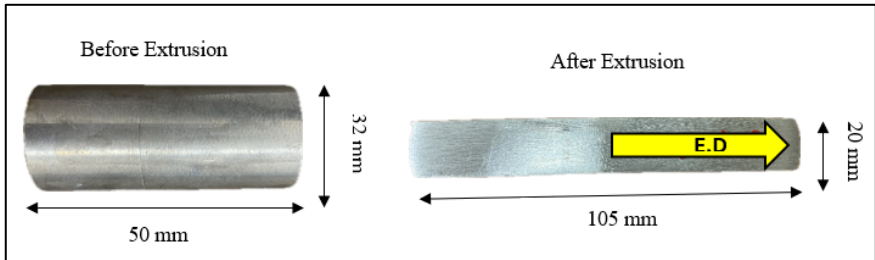


Figure 1. Sample dimensions before and after hot extrusion.

The chemical compositions of the synthesized alloys, designated as NX (Mg–2Zn–1Y + 0.5 wt.% of Zr, Gd, La, Ag, or Ca), were characterized using X-ray fluorescence (XRF) analysis with a Rigaku ZSX Primus II spectrometer. Phase identification was performed on the as-cast samples using X-ray diffraction (XRD) and conducted with a Rigaku Ultima IV diffractometer. The scans were carried out over a 2θ range of 0–90° at a scanning rate of 3°/min.

Microstructural evaluations were initially conducted using optical microscopy (OM) with a Carl Zeiss optical microscope. Specimens were metallographically prepared by grinding, polishing, and etching with a picric acid solution. Average grain sizes were determined from calibrated 20 μm -scale micrographs using the Line Intercept Method, by ASTM E112 standards. Detailed surface and

phase morphology investigations were conducted using a Carl Zeiss Ultra Plus Gemini scanning electron microscope (SEM) and energy-dispersive X-ray spectroscopy (EDX) to assess localized elemental distribution.

The corrosion behavior of both as-cast and extruded samples was assessed through electrochemical potentiodynamic polarization and static immersion tests, conducted in Hank's balanced salt solution (composition provided in Table 1). All corrosion experiments were performed at a physiological pH of 7.3 and a temperature of 36.5 °C.

Table 1. Chemical composition of Hank's solution.

Chemical Composition	Concentration (g/L)
NaCl	8
KCl	0.4
MgSO ₄ .7H ₂ O	0.06
MgCl ₂ .6H ₂ O	0.1
CaCl ₂	0.14
Na ₂ HPO ₄ .2H ₂ O	0.06
KH ₂ PO ₄	0.06
Glucose: C ₆ H ₆ O.2H ₂ O	0.1
NaHCO ₃	0.35

Potentiodynamic polarization testing was performed on both as-cast and extruded specimens, with the latter sectioned perpendicular to the extrusion direction. Each sample was mounted in epoxy resin, with electrical contact established via copper wire. Before testing, the exposed surface was ground using 1200-grit silicon carbide (SiC) abrasive paper to achieve a clean and uniform surface finish. An adhesive tape with a circular aperture of 0.19 cm²

was applied to the polished surface to define a consistent area of exposure. This ensured that only the designated area was in contact with the electrolyte during testing.

The electrochemical setup consisted of a three-electrode configuration: the sample served as the working electrode, a graphite rod functioned as the counter electrode, and a saturated calomel electrode (SCE) was employed as the reference electrode. All electrodes were placed in a 250 mL Isotherm Boro 3.3 glass beaker filled with Hank's balanced salt solution, maintained at 36.5 °C. Before initiating the polarization scan, each specimen was stabilized in the electrolyte for 300 seconds to allow for the establishment of a steady open-circuit potential (E_{corr}). Measurements were performed at room temperature under zero current conditions to monitor the potential difference between the working and reference electrodes.

Subsequently, potentiodynamic polarization curves were acquired by scanning the potential from -0.25 V to $+0.25$ V relative to E_{corr} at a scan rate of 1 mV/s, progressing from cathodic to anodic polarization. Extrapolating the Tafel regions allowed for the determination of the corrosion potential (E_{corr}) and corrosion current density (I_{corr}). All electrochemical measurements were conducted using a Gamry PC4/300 potentiostat/galvanostat, with data acquisition and analysis performed via DC105 software. Each condition was tested in triplicate, and the reported values represent the arithmetic average of the three independent measurements.

Immersion corrosion testing was conducted on the as-cast and hot-extruded samples in Hank's balanced salt solution (composition detailed in Table 1), maintained at a physiological temperature of 36.5 °C. For each alloy, cubic specimens with dimensions of $10 \times 10 \times 10$ mm were sectioned and sequentially ground using SiC papers of 400, 600, 800, 1000, and 1200 grit to achieve uniform surface finishes. The samples were then

ultrasonically cleaned in ethanol for 5 minutes to remove surface contaminants. Before immersion, the surface areas were calculated, and the initial mass (M_s) of each specimen was recorded using a high-precision analytical balance (Precisa XB 220A).

The immersion durations were set at 24, 48, and 72 hours, during which the specimens were individually immersed in separate containers of Hank's solution. Following each immersion period, the corrosion products were removed by submerging the samples in an aqueous chromic acid solution (182 g/L) and ultrasonically cleaning them for 5 minutes. Specimens were then rinsed with distilled water, followed by an ethanol wash using the ultrasonic cleaner, and subsequently dried. Final mass (M_f) measurements were recorded post-drying, and the mass loss due to corrosion was calculated as the difference between M_s and M_f .

To monitor the stability of the corrosion environment, the pH values of the Hank's solution were measured before and after immersion using a Hanna Instruments HI 83141 Portable Analog pH/ORP meter. Post-test surface analyses were performed on all corroded samples using scanning electron microscopy (SEM) and energy-dispersive X-ray spectroscopy (EDS) to evaluate corrosion morphology and compositional changes.

Additionally, the hydrogen evolution method was used to assess the biodegradability of the alloys further. Rectangular specimens measuring $20 \times 20 \times 10$ mm were prepared and polished using the same surface preparation protocol. The samples were immersed in Hank's solution at 36.5°C for 72 hours, with measurements taken at 24 hours. The hydrogen evolution setup consisted of sealed Isotherm beakers with air outlet ports connected to glass syringes via rubber tubing. Plastic clamps were used to prevent gas leakage, and the lids were tightly sealed to ensure airtight conditions. The volume of evolved hydrogen gas was measured directly from the syringes at each time point.

The underlying electrochemical reaction governing hydrogen release from Mg alloy degradation is represented in the equation below:



RESULTS AND DISCUSSION

XRD Phase Analysis

The chemical composition analysis results for the fabricated Mg-2Zn-1Y+0.5 (Gd, La, Zr, Ag, and Ca) casting alloys, coded as, are outlined in Table 2. In contrast, the X-ray diffraction (XRD) patterns of the investigated alloys are depicted in Fig. 1.

Alloys	Produced alloys	Elements (wt. %)								
		Mg	Zn	Y	Zr	Gd	La	Ag	Ca	Al
NX	Mg-2Zn-1Y +0.5(Zr,Gd,La,Ag,Ca)	Bal.	1.68	0.78	0.63	0.72	0.43	0.41	0.47	0.02

Table 2. Chemical compositions wt. % of the investigated Mg-2Zn-1Y+ 0.5 (Gd, La, Zr, Ag, and Ca) as-cast alloys.

X-ray diffraction (XRD) analysis of the NX alloy revealed a multi-phase microstructure dominated by the α -Mg matrix. In the Mg-Zn-Y system, three key intermetallic phases are typically formed depending on the Zn/Y atomic ratio: the icosahedral I-phase ($\text{Mg}_3\text{Zn}_6\text{Y}_2$), the W-phase ($\text{Mg}_3\text{Zn}_3\text{Y}_2$), and the long-period stacking ordered (LPSO) phase (Mg_{12}ZnY). (Hao et al., 2022; Liao et al., 2020; Tahreen & Chen, 2016a). The Zn/Y ratio in the NX alloy was calculated to be 2.15, which lies within the known stability ranges for both the I-phase (1.10–4.38) and the W-phase (1–6) (Aljarrah et al., 2021; Lee et al., 2005a). Accordingly, XRD results confirmed the presence of both I and W phases in the alloy (Lee et al., 2005; Yamasaki & Kawamura, 2009).

Table 3. Determination of I, W and LPSO regarding Zn/Y ratios.

Alloys	Zn/Y > 1 and < 6	Zn/(Y+Nd) [0.85 - 2.05]	Phases	Zn/REE <1	Phases
NX	2.15	2.15	I and W phases determined	0.87	LPSO determined

The LPSO phase is generally favored when the Zn/Y or Zn/REE atomic ratio is less than 1.0 (Hao et al., 2022). In NX, the Zn/Y ratio was 0.87, which supports the formation of the LPSO phase as well. Indeed, the presence of the LPSO structure was detected, consistent with the literature (Liao et al., 2020).

In addition to these ternary phases, the inclusion of minor alloying elements such as Gd, La, Zr, Ag, and Ca resulted in the formation of secondary intermetallic compounds. Among them, $\text{Ca}_2\text{Mg}_6\text{Zn}_3$ (Fu et al., 2022), $\text{Mg}_{54}\text{Ag}_{17}$, and $\text{Mg}_{17}\text{La}_2$ (X. Zhang et al., 2023) were identified in the XRD patterns. These intermetallics are known to influence the corrosion and mechanical behavior of magnesium alloys by contributing to microstructural heterogeneity and localized galvanic interactions. The multiphase structure of the NX alloy, particularly the coexistence of α -Mg with I, W, and LPSO phases, along with these secondary precipitates, plays a crucial role in its degradation profile and is expected to impact its corrosion performance in physiological environments significantly.

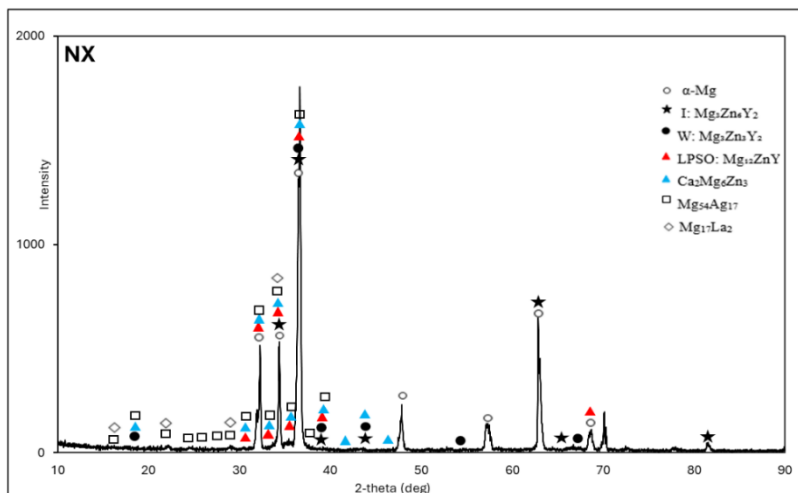


Fig 2. XRD results of the as-cast NX alloy.

Microstructure

Fig. 3 presents the microstructure of the as-cast optimized $\text{Mg-2Zn-1Y} + 0.5\text{X}$ (NX) alloy. The alloy exhibits a fine microstructure composed predominantly of small equiaxed dendrites, with an average grain size of approximately $74\ \mu\text{m}$, and a net-like eutectic structure located in the interdendritic regions (Fig. 3a). The SEM image (Fig. 3a') further reveals that the eutectic phase is not uniformly distributed; instead, it appears as discontinuous lath-like structures in the narrow regions between dendrites and as pool-like regions at triple junctions. These pools exhibit a regular lamellar morphology, indicative of a eutectic solidification mode.

XRD analysis confirms the presence of multiple phases, including primary $\alpha\text{-Mg}$ and a combination of secondary phases such as I-phase, W-phase, LPSO structures, $\text{Ca}_2\text{Mg}_6\text{Zn}_3$, $\text{Mg}_{54}\text{Ag}_{17}$, and $\text{Mg}_{17}\text{La}_2$ (Fig. 1). These findings align well with the observed microstructure, suggesting that the $\alpha\text{-Mg}$ forms the primary dendrites. In contrast, the interdendritic white phases are likely comprised of the Zn- and Y-enriched I-, W-, and LPSO ternary

phases. This interpretation is supported by SEM and EDS analysis, which demonstrate that the interdendritic phases are rich in Zn and Y (Fig. 3a') — consistent with previous findings on the compositional nature of these ternary phases (Huang et al., 2009).

Moreover, a distinct white particle observed at the center of some grains (Fig. 3a) is identified by EDS (spot N:4) as being rich in Zr. Based on literature, elemental Zr is known to act as a potent heterogeneous nucleant during solidification, promoting the formation of α -Mg grains by serving as a nucleation site (Qian & Das, 2006; StJohn et al., 2005). Thus, this Zr-rich particle likely serves as the nucleation core for the observed dendrites.

In addition to Zn, Y, and Zr, the microstructure also contains Ca-rich interdendritic particles (Fig. 3a'). These particles, according to prior studies, are indicative of eutectic Mg-Ca-rich brittle phases, which tend to segregate in the interdendritic regions. While a portion of the Ca may dissolve in the α -Mg matrix, its excessive presence can form coarse, brittle phases that may adversely affect mechanical properties (Kim et al., 2012; B. Tang et al., 2005).

Furthermore, the introduction of other rare earth elements, such as Gd, has been shown to significantly refine the microstructure by reducing the grain size and increasing the volume fraction of secondary phases. This modification enhances the strength and corrosion resistance of the alloy, making it more suitable for biomedical applications (J. Wu et al., 2014).

The microstructure of the extruded Mg-2Zn-1Y + 0.5X (NX) alloy, as shown in Fig. b and b', exhibits a homogenous and refined grain structure, indicative of extensive dynamic recrystallization (DRX). The extrusion process transformed the coarse, dendritic grains of the as-cast state into fine, equiaxed grains, thereby eliminating the prior dendritic morphology and significantly refining the microstructure. The grains appear uniformly distributed

with no visible elongation along the extrusion direction, further confirming the completion of DRX (Yamasaki et al., 2010).

In addition to the refined α -Mg matrix, numerous small, bright particles can be observed dispersed throughout the microstructure. These are likely secondary phases, such as fragmented long-period stacking ordered (LPSO) structures and intermetallic compounds (e.g., I-phase, W-phase), which have been redistributed during the extrusion process. The alignment and distribution of these phases contribute to enhanced mechanical performance by impeding dislocation movement and strengthening the matrix (J. Li et al., 2015).

Extrusion parameters, including temperature, extrusion ratio, and speed, play a crucial role in the extent of recrystallization and, consequently, significantly impact the final mechanical properties. While higher extrusion ratios and faster speeds can promote DRX, they may also lead to partial dissolution or fragmentation of strengthening phases, which can reduce tensile strength if not optimized (Hirano et al., 2010).

The addition of yttrium (Y) further contributes to refining the microstructure and forming stable LPSO phases. These phases, in conjunction with hot extrusion, improve the homogeneity of the alloy and enhance its mechanical properties by providing thermal stability and strength (Yamasaki et al., 2010).

One of the most notable improvements following extrusion is the significant reduction in grain size. In the current study, the grain size decreased from approximately 74 μm in the as-cast condition to about 21 μm after extrusion. This reduction is consistent with Hall–Petch strengthening behavior and leads to improved strength and ductility. Literature reports even finer grain structures, such as 100 - 150 nm in $\text{Mg}_{97}\text{Zn}_1\text{Y}_2$ alloys, which result in ultrahigh

strength and superplastic properties (Inoue et al., 2001; Yoshimoto et al., 2006).

SEM evidence confirms that the extrusion process significantly refines the microstructure, enhances the dispersion of secondary phases, and improves the mechanical behavior of the NX alloy system, making it a strong candidate for structural and biomedical applications.

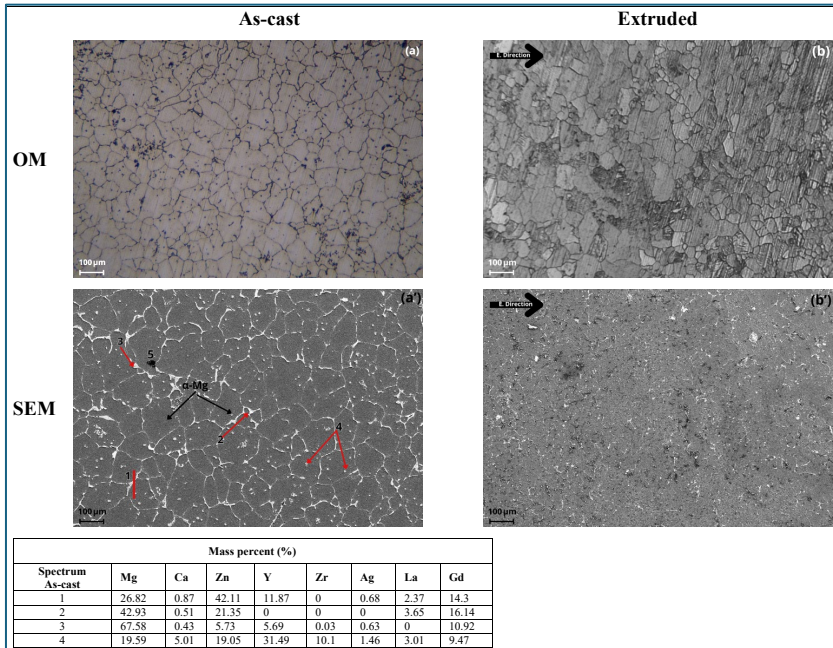


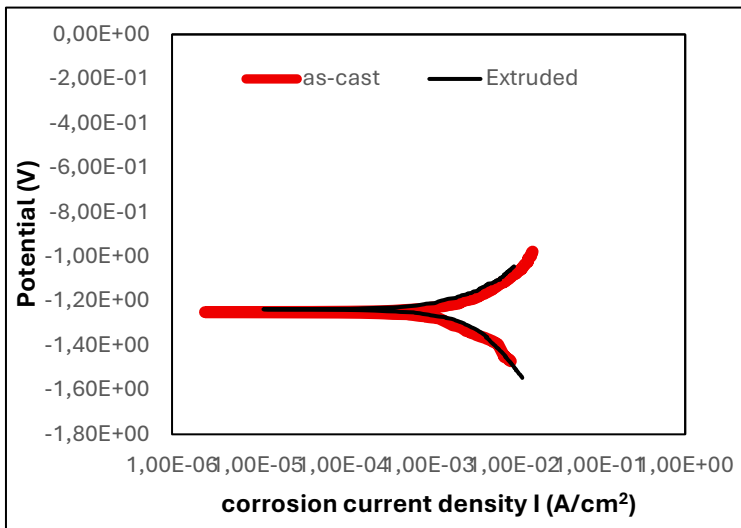
Fig 3. OM and SEM micrographs of as-cast and Extruded NX alloy.

Potentiodynamic Polarization

In Fig. 4, the Tafel curves from potentiodynamic polarization tests in Hank's solution at $\sim 36.5^\circ\text{C}$ on the NX as-cast and after extrusion alloys are presented, with corrosion current density and corrosion potential values shown in Fig. 5. The as-cast state exhibits a relatively noble corrosion potential, indicating better inherent corrosion resistance compared to the extruded state.

The results shown in Fig.5 revealed that the as-cast Mg–2Zn–1Y–0.5X alloys exhibited a corrosion, as current density of $\sim 1500 \mu\text{A}/\text{cm}^2$, while the extruded counterparts showed an increased value of $\sim 2030 \mu\text{A}/\text{cm}^2$. This indicates that extrusion led to a deterioration in corrosion resistance, contrary to the common assumption that thermomechanical processing improves degradation performance in biodegradable Mg alloys (Zheng et al., 2014). The observed increase in corrosion rate after extrusion is attributed to multiple microstructural changes. Grain refinement, increased dislocation density, and the redistribution of second-phase particles intensify micro-galvanic coupling and promote localized corrosion (Aghion et al., 2015; Yang et al., 2020a). While extrusion may homogenize the microstructure and fragment intermetallics, it can also disrupt the passive $\text{Mg}(\text{OH})_2$ layer by increasing the number of electrochemically active sites and grain boundaries, which serve as high-energy dissolution sites under physiological conditions (Atrens et al., 2020; Dobkowska et al., 2022).

Fig 4. Potentiodynamic polarization graphs of as-cast and Extruded NX alloy.

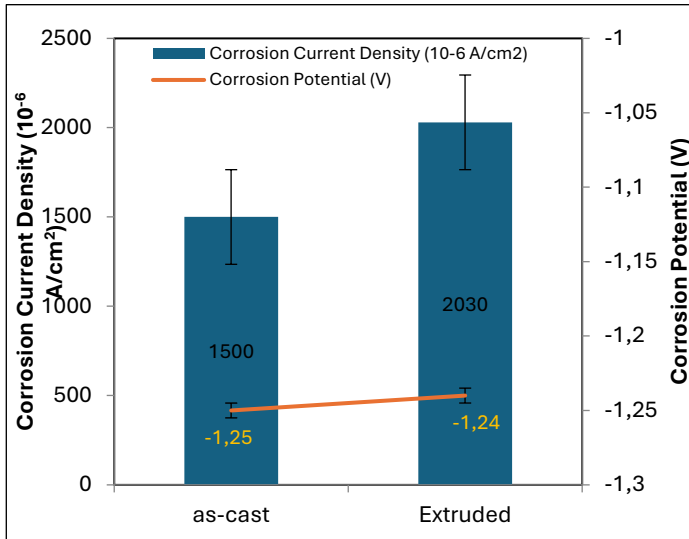


The corrosion behavior is strongly influenced by the alloying elements and the intermetallic phases they form. In the as-cast condition, the formation of long-period stacking ordered (LPSO) phases and ternary compounds such as I-phase ($\text{Mg}_3\text{Zn}_6\text{Y}$) and W-phase ($\text{Mg}_3\text{Zn}_3\text{Y}_2$) contributes to improved corrosion performance via grain refinement and semi-passive film stabilization (Nie, 2012; J. Wang et al., 2018). However, the W-phase exhibits a relatively high potential difference (~ 120 mV) with the α -Mg matrix, increasing its cathodic role and thus its galvanic influence (S. Yin et al., 2020). In contrast, the I-phase and X-phase (Mg_{12}YZn) demonstrate lower potential differences, potentially reducing galvanic corrosion (Shi et al., 2022; Tahreen & Chen, 2016; Zengin & Turen, 2020).

Rare-earth additions such as Gd and La form stable intermetallics (e.g., $\text{Mg}_{17}\text{La}_2$) that can enhance corrosion resistance by stabilizing the corrosion front and the passive layer (Beura et al., 2020; Meng et al., 2013). However, upon extrusion, these intermetallics may become more electrochemically active and contribute to localized corrosion due to their fragmented and redistributed nature (Yamasaki et al., 2022). Additional alloying elements also play nuanced roles. Zirconium promotes grain refinement during solidification, thereby reducing localized anodic dissolution. Calcium, on the other hand, forms $\text{Ca}_2\text{Mg}_6\text{Zn}_3$, which enhances the protective surface film. Ag additions, although beneficial to mechanical properties, tend to form fine cathodic $\text{Mg}_{54}\text{Ag}_{17}$ precipitates, slightly increasing localized corrosion in extruded states (Ding et al., 2014; L. Wang et al., 2017; X. Wu et al., 2024; J. Yin et al., 2024). The chloride-rich environment of Hank's solution (~ 142 mM Cl^-) further exacerbates degradation by destabilizing the $\text{Mg}(\text{OH})_2$ film and inducing pitting (Lamaka et al., 2018; Xin et al., 2008; Zainal Abidin et al., 2011). Nevertheless, the as-cast alloys maintained corrosion behavior within acceptable

ranges for temporary implant materials, indicating a partially stabilized degradation mechanism enabled by the alloying strategy.

Fig 5. Current density and potential values of as-cast and Extruded NX alloy.



In conclusion, although extrusion is generally intended to refine the microstructure and enhance performance, its impact on corrosion resistance in these Mg–2Zn–1Y–0.5X alloys was detrimental. This highlights the crucial importance of alloy-specific optimization of processing parameters, given the intricate interplay between microstructure, intermetallic evolution, and corrosion mechanisms in biodegradable Mg-based systems.

Immersion

The immersion corrosion test results for the as-cast and extruded NX alloy, including mass loss over time, corrosion rate graphs, pH values before and after testing, and surface images of the samples after the experiment, are presented in Figs. 6-9. During the 72-hour immersion in Hank's solution, corrosion product deposits

formed on the NX alloy surface, leading to an increase in pH values throughout the test period (Table 4).

In the as-cast condition, mass loss progressed rapidly during the first 24 hours (Figs. 6 and 7), with corrosion continuing over the subsequent 48 hours. The protective oxide film on the surface of the Mg alloy is initially unstable in physiological solutions, resulting in rapid corrosion rates during the early stages. However, as dissolution proceeds, the oxide layer stabilizes, resulting in a slowed corrosion rate. The corrosion behavior of magnesium alloys in physiological environments is complex and dynamic. Initially, aggressive ions like chloride can induce pitting corrosion, while phosphates and carbonates may slow corrosion rates through precipitation (Xin et al., 2008). The early stages of corrosion are characterized by rapid degradation, but as immersion time increases, a protective layer forms, stabilizing the corrosion rate (Veleva et al., 2018). This physiological stabilization process can be leveraged to improve corrosion resistance and biocompatibility of magnesium alloys (Zhou et al., 2013).

After extrusion, the corrosion rate of the NX alloy increased compared to its as-cast state. This acceleration is attributed to the amount and distribution of precipitates, which influence degradation behavior through micro-galvanic corrosion. The homogenization treatment before extrusion is believed to promote a more uniform distribution of these phases. Consequently, the degradation surfaces of the extruded NX alloy became smoother and exhibited fewer pits despite the increased corrosion rate (Dai et al., 2024; Yang et al., 2020)

Fig 6. Mass loss of as-cast and extruded NX alloys after immersion test.

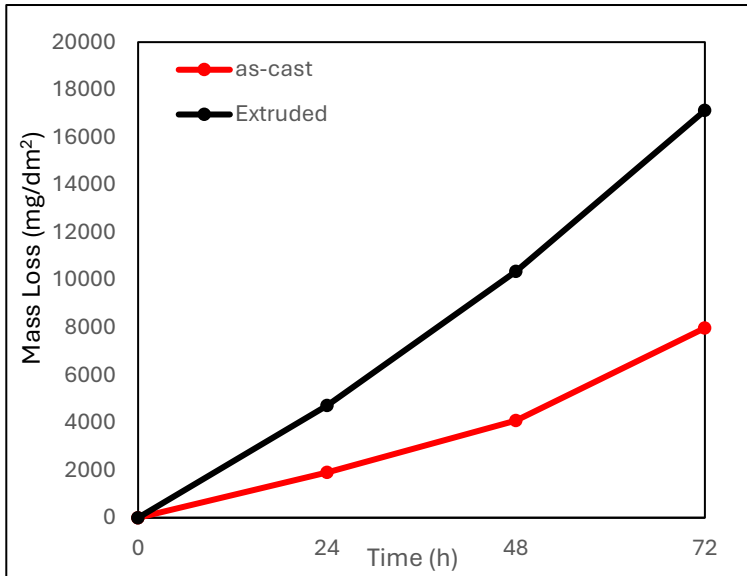
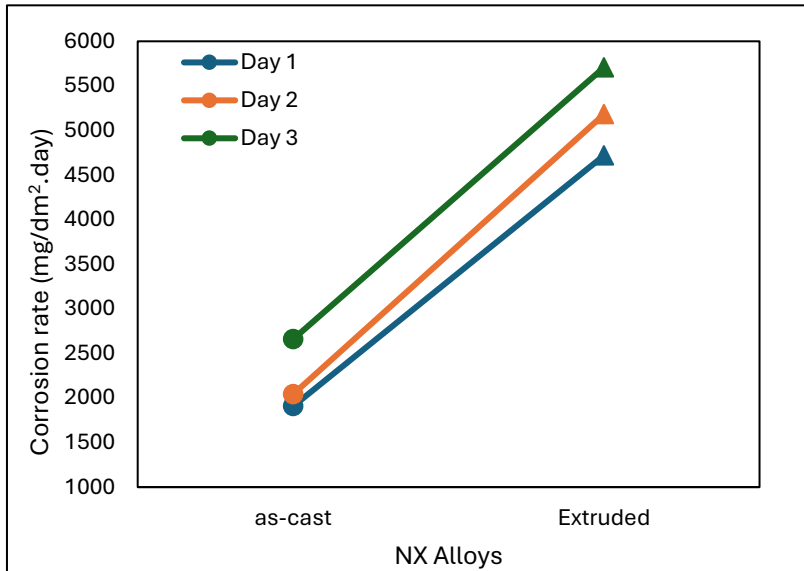


Fig 7. Corrosion rate of as-cast and extruded NX alloys after immersion test.



SEM images revealed that corrosion in the NX alloy primarily advanced along grain boundaries where secondary phases accumulated. Pitting corrosion was evident along these grain boundaries in both the as-cast and extruded states. The pit size and depth varied, reflecting the influence of microstructural features on the progression of corrosion.

Crystalline defects such as high dislocation density, introduced or increased by extrusion, negatively impact the corrosion resistance of the NX alloy. These defects reduce the electrode potential, increasing the dissolution rate of the anodic regions and thereby accelerating corrosion (W. Li et al., 2020).

Finally, the pH values measured after immersion (Table 4) showed an increase, indicating an alkaline environment proportional to the corrosion rate observed in the NX alloy. These immersion test results align well with those obtained from potentiodynamic corrosion measurements.

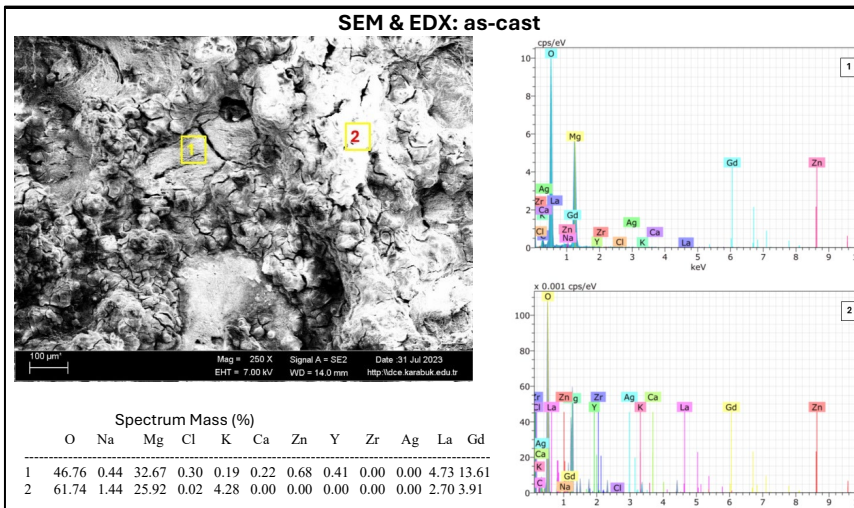


Fig. 8. SEM images of the immersion test applied to as-cast NX alloys.

Table 4. pH of the Hank's solution of the tested NX alloys after 72 h of immersion.

pH before test: 7.3	As-cast	Extruded
NX	9.41	10.02

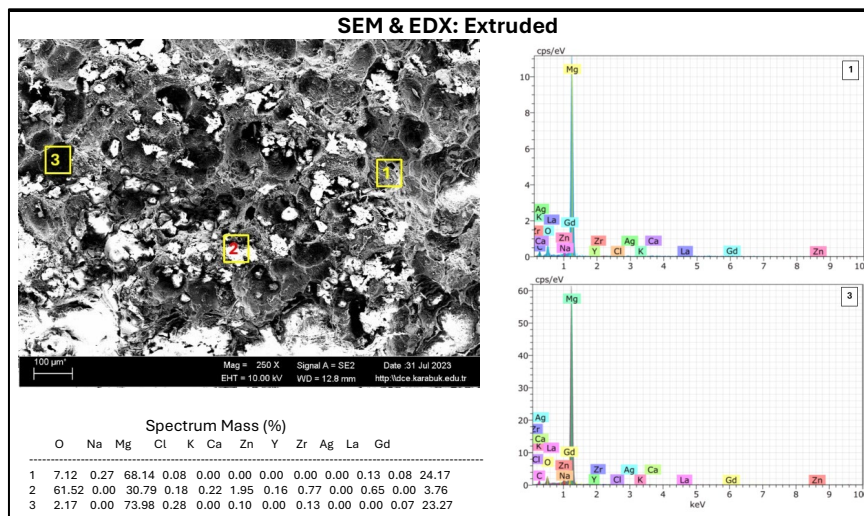


Fig. 9. SEM images of the immersion test applied to extruded NX alloys.

H₂ Evolution

The hydrogen gas evolution results during 72 hours of immersion in Hank's solution for the NX alloy are shown in Fig.10 and 11. In the as-cast condition, NX exhibited a moderate volume of hydrogen evolution, indicating an intermediate corrosion rate. After extrusion, the hydrogen evolution volume increased for NX, suggesting that extrusion accelerated the corrosion process for this alloy. These results are consistent with the trends observed in both potentiodynamic polarization and immersion corrosion tests.

Typically, the acceptable H₂ evolution rate is determined by ensuring that the rate of gas formation is slow enough to allow the surrounding tissue to absorb the hydrogen safely.

In research (Amukarimi & Mozafari, 2021), it is generally considered acceptable if the H₂ evolution rate is around **0.01 to 0.5 mL/cm²/day**. However, the actual acceptable rate can vary depending on the specific alloy composition, surface treatments, and the biological environment in which it is used. For this study which involves the Mg-2Zn-1Y +0.5(Gd, Zr, La, Ag, Ca) alloys, the H₂ evolution rate per day is presented in Fig. 10. Results indicate that lowest results were obtained from as-cast NX are near to the acceptable volume of H₂ accumulated during immersion in Hank's solution per day, with values of 1.17 ml/cm², this last should ideally be compared to the rates reported in similar studies of biodegradable Mg-based implants.

Fig 10. H₂ gas volume after 72 h of immersion in Hank's solution of a-cast and extruded NX alloys.

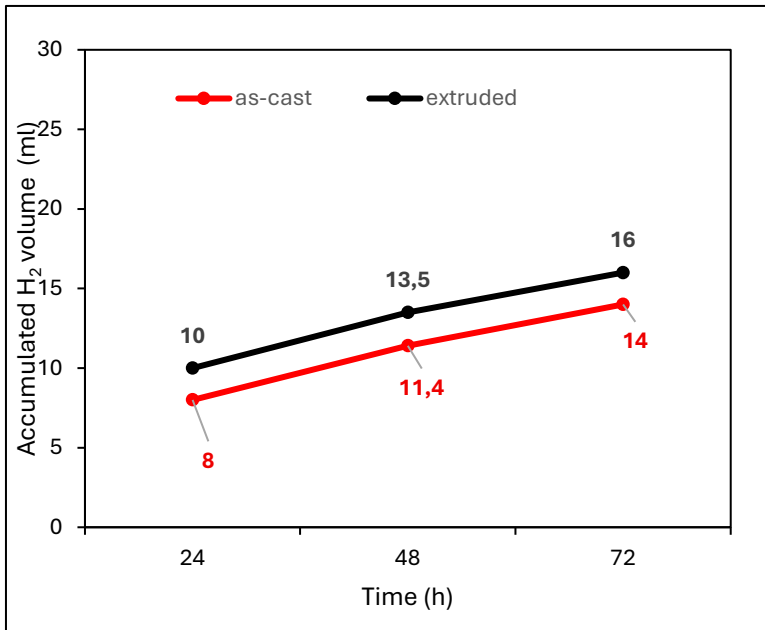
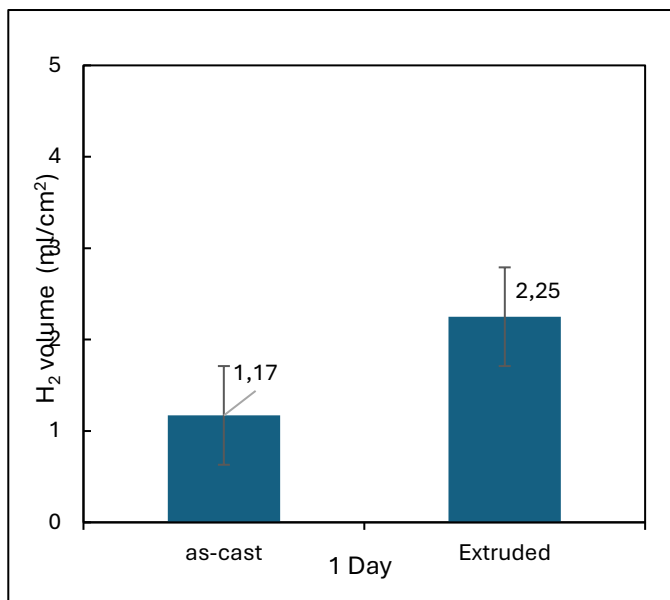


Fig 11. Hydrogen evolution rate per day of the investigated NX alloys.



General Assessment

This chapter presents a systematic investigation into the corrosion behavior and hydrogen evolution characteristics of as-cast and extruded Mg–2Zn–1Y–0.5X (X = Gd, La, Zr, Ag, Ca) alloys in simulated physiological conditions. Through combined microstructural analysis, electrochemical testing, immersion corrosion, and hydrogen evolution measurements, several key insights have been achieved.

The as-cast alloys demonstrated superior corrosion resistance compared to their extruded counterparts, contrary to conventional expectations. This degradation trend was evident across potentiodynamic polarization, immersion, and hydrogen evolution assessments. While extrusion effectively refined the grain structure and homogenized secondary phases, it also increased the density of

grain boundaries and active sites, intensifying micro-galvanic interactions and accelerating corrosion.

The alloying strategy adopted in this study played a critical role in tailoring degradation behavior. Rare-earth and biocompatible elements such as Gd, La, Zr, Ca, and Ag contributed to complex multiphase microstructures, including the formation of I-, W-, LPSO phases and intermetallic compounds like $\text{Ca}_{22}\text{Mg}_6\text{Zn}_3$ and $\text{Mg}_{17}\text{La}_2$. These phases, depending on their morphology and distribution, exhibited varied impacts on corrosion mechanisms. Notably, Ca and Zr demonstrated stabilizing effects on the passive layer, while Ag and fragmented intermetallics in the extruded state occasionally promoted localized corrosion.

Hydrogen evolution data further confirmed that extrusion increased the degradation rate, as reflected by higher gas volumes, especially in the first 24 hours. Despite this, the overall hydrogen evolution values for the as-cast alloys remained within or near the clinically acceptable range, suggesting promise for controlled biodegradation in orthopedic applications.

From a clinical perspective, while extrusion offers mechanical advantages through grain refinement and improved phase dispersion, its influence on corrosion must be carefully managed. Processing parameters and post-extrusion treatments should be optimized to mitigate corrosion acceleration. Future work should also focus on *in vivo* validations and surface modification techniques to balance mechanical integrity and corrosion control.

In conclusion, the Mg–2Zn–1Y–0.5X alloys, particularly in their as-cast form, exhibit promising characteristics for biodegradable implant applications. However, their practical use will depend on fine-tuned processing routes, strategic alloying, and possibly surface treatments to ensure a synchronized degradation profile compatible with the biological healing timeline.

Acknowledgement

This research was supported by The Scientific and Technological Research Council of Turkey (TUBITAK) with 1002-Short Term R&D Funding Program (Project No. 222M438) and Karabük University Scientific Research Projects Coordination Unit (KBÜBAP-24-DS-037).

References

Agha, N. A., Feyerabend, F., Mihailova, B., Heidrich, S., Bismayer, U., & Willumeit-Römer, R. (2016). Magnesium degradation influenced by buffering salts in concentrations typical of in vitro and in vivo models. *Materials Science and Engineering: C*, 58, 817–825. <https://doi.org/10.1016/j.msec.2015.09.067>

Aghion, E., Jan, L., Meshi, L., & Goldman, J. (2015). Increased corrosion resistance of the AZ80 magnesium alloy by rapid solidification. *Journal of Biomedical Materials Research Part B: Applied Biomaterials*, 103(8), 1541–1548. <https://doi.org/10.1002/jbm.b.33335>

Aljarrah, M., Alnahas, J., & Alhartomi, M. (2021). Thermodynamic Modeling and Mechanical Properties of Mg-Zn- $\{Y, Ce\}$ Alloys: Review. *Crystals*, 11(12), 1592. <https://doi.org/10.3390/cryst11121592>

Alvarez-Lopez, M., Pereda, M. D., del Valle, J. A., Fernandez-Lorenzo, M., Garcia-Alonso, M. C., Ruano, O. A., & Escudero, M. L. (2010). Corrosion behaviour of AZ31 magnesium alloy with different grain sizes in simulated biological fluids☆. *Acta Biomaterialia*, 6(5), 1763–1771. <https://doi.org/10.1016/j.actbio.2009.04.041>

Amukarimi, S., & Mozafari, M. (2021). Biodegradable magnesium-based biomaterials: An overview of challenges and opportunities. *MedComm*, 2(2), 123–144. <https://doi.org/10.1002/mco2.59>

Atrens, A., Shi, Z., Mehreen, S. U., Johnston, S., Song, G.-L., Chen, X., & Pan, F. (2020). Review of Mg alloy corrosion rates. *Journal of Magnesium and Alloys*, 8(4), 989–998. <https://doi.org/10.1016/j.jma.2020.08.002>

Beura, V. K., Garg, P., Joshi, V. V., & Solanki, K. N. (2020). *Numerical Investigation of Micro-Galvanic Corrosion in Mg Alloys: Role of the Cathodic Intermetallic Phase Size and Spatial Distributions* (pp. 217–223). https://doi.org/10.1007/978-3-030-36647-6_34

Birbilis, N., Ralston, K. D., Virtanen, S., Fraser, H. L., & Davies, C. H. J. (2010). Grain character influences on corrosion of ECAPed pure magnesium. *Corrosion Engineering, Science and Technology*, 45(3), 224–230. <https://doi.org/10.1179/147842209X12559428167805>

Bommala, V. K., Krishna, M. G., & Rao, C. T. (2019). Magnesium matrix composites for biomedical applications: A review. *Journal of Magnesium and Alloys*, 7(1), 72–79. <https://doi.org/10.1016/j.jma.2018.11.001>

Böstman, O., Viljanen, J., Salminen, S., & Pihlajamäki, H. (2000). Response of articular cartilage and subchondral bone to internal fixation devices made of poly-L-lactide: a histomorphometric and microradiographic study on rabbits. *Biomaterials*, 21(24), 2553–2560. [https://doi.org/10.1016/S0142-9612\(00\)00123-X](https://doi.org/10.1016/S0142-9612(00)00123-X)

Chen, K., Dai, J., & Zhang, X. (2015). Improvement of corrosion resistance of magnesium alloys for biomedical applications. *Corrosion Reviews*, 33(3–4), 101–117. <https://doi.org/10.1515/corrrev-2015-0007>

Chen, T. J., Wang, W., Zhang, D. H., Ma, Y., & Hao, Y. (2013a). Development of a new magnesium alloy ZW21. *Materials & Design*, 44, 555–565. <https://doi.org/10.1016/j.matdes.2012.08.040>

Chen, T. J., Wang, W., Zhang, D. H., Ma, Y., & Hao, Y. (2013b). Development of a new magnesium alloy ZW21.

Materials & Design, 44, 555–565.
<https://doi.org/10.1016/j.matdes.2012.08.040>

Chen, T. J., Wang, W., Zhang, D. H., Ma, Y., & Hao, Y. (2013c). Development of a new magnesium alloy ZW21. *Materials & Design*, 44, 555–565.
<https://doi.org/10.1016/j.matdes.2012.08.040>

Dai, C., Wang, J., Pan, Y., Ma, K., Peng, Y., Wang, Y., Wang, D., Wang, J., & Ma, Y. (2024). Modulation of corrosion properties by heat treatment and extrusion with mechanism analysis of high mechanical strength Mg-5.6Dy-3.1Ni alloy. *Materials Characterization*, 209, 113662.
<https://doi.org/10.1016/j.matchar.2024.113662>

Deng, W., Zhang, X., Huang, L., Xu, X., Wang, L., Wang, J., Shang, Q., Lee, S., & Jie, J. (2016). Aligned Single-Crystalline Perovskite Microwire Arrays for High-Performance Flexible Image Sensors with Long-Term Stability. *Advanced Materials*, 28(11), 2201–2208.
<https://doi.org/10.1002/adma.201505126>

Ding, Y., Wen, C., Hodgson, P., & Li, Y. (2014). Effects of alloying elements on the corrosion behavior and biocompatibility of biodegradable magnesium alloys: a review. *J. Mater. Chem. B*, 2(14), 1912–1933.
<https://doi.org/10.1039/C3TB21746A>

Djebbari, K., Türen, Y., Elen, L., & Ahlatçı, H. (2025). A Comparative Study of As-Cast Alloys of ZW21 with Varied Element Additions, Investigating Dry and Corrosive Wear in Body Fluid. *JOM*, 77(6), 4344–4362.
<https://doi.org/10.1007/s11837-025-07394-z>

Dobkowska, A., Adamczyk-Cieślak, B., Chlewicka, M., Towarek, A., Zielińska, A., Koralknik, M., Kuc, D., & Mizera, J.

(2022). Evolution of microstructure dependent corrosion properties of ultrafine AZ31 under conditions of extrusion with a forward backward oscillating die. *Journal of Materials Research and Technology*, 18, 4486–4496. <https://doi.org/10.1016/j.jmrt.2022.04.131>

Frost HM, *Clin Orthop Relat Res*. 1989; (248):283-93. PMID: 2680202. (n.d.).

Fu, J., Du, W., Liu, K., Du, X., Zhao, C., Liang, H., Mansoor, A., Li, S., & Wang, Z. (2022). Effect of the Ca₂Mg₆Zn₃ Phase on the Corrosion Behavior of Biodegradable Mg-4.0Zn-0.2Mn-xCa Alloys in Hank's Solution. *Materials*, 15(6), 2079. <https://doi.org/10.3390/ma15062079>

Gonzlez, S., Pellicer, E., Suriach, S., Bar, M. D., & Sort, J. (2013). Biodegradation and Mechanical Integrity of Magnesium and Magnesium Alloys Suitable for Implants. In *Biodegradation - Engineering and Technology*. InTech. <https://doi.org/10.5772/55584>

Gu, X. N., Zhou, W. R., Zheng, Y. F., Cheng, Y., Wei, S. C., Zhong, S. P., Xi, T. F., & Chen, L. J. (2010). Corrosion fatigue behaviors of two biomedical Mg alloys – AZ91D and WE43 – In simulated body fluid. *Acta Biomaterialia*, 6(12), 4605–4613. <https://doi.org/10.1016/j.actbio.2010.07.026>

Hao, J., Zhang, J., Wang, H., Cheng, W., & Bai, Y. (2022a). Microstructure and mechanical properties of Mg–Zn–Y–Mn magnesium alloys with different Zn/Y atomic ratio. *Journal of Materials Research and Technology*, 19, 1650–1657. <https://doi.org/10.1016/j.jmrt.2022.05.153>

Hirano, M., Yamasaki, M., Hagihara, K., Higashida, K., & Kawamura, Y. (2010). Effect of Extrusion Parameters on

Mechanical Properties of Mg₉₇Zn₁Y₂ Alloys at Room and Elevated Temperatures. *MATERIALS TRANSACTIONS*, 51(9), 1640–1647. <https://doi.org/10.2320/matertrans.MAW201026>

Hou, L., Li, Z., Pan, Y., Du, L., Li, X., Zheng, Y., & Li, L. (2014). In vitro and in vivo studies on biodegradable magnesium alloy. *Progress in Natural Science: Materials International*, 24(5), 466–471. <https://doi.org/10.1016/j.pnsc.2014.09.002>

Huang, Z. H., Liang, S. M., Chen, R. S., & Han, E. H. (2009a). Solidification pathways and constituent phases of Mg–Zn–Y–Zr alloys. *Journal of Alloys and Compounds*, 468(1–2), 170–178. <https://doi.org/10.1016/j.jallcom.2008.01.034>

Inoue, A., Kawamura, Y., Matsushita, M., Hayashi, K., & Koike, J. (2001). Novel hexagonal structure and ultrahigh strength of magnesium solid solution in the Mg–Zn–Y system. *Journal of Materials Research*, 16(7), 1894–1900. <https://doi.org/10.1557/JMR.2001.0260>

JACOBS, J. J., GILBERT, J. L., & URBAN, R. M. (1998). Corrosion of Metal Orthopaedic Implants*. *The Journal of Bone and Joint Surgery (American Volume)*, 80(2), 268–282. <https://doi.org/10.2106/00004623-199802000-00015>

Jacobs, J. J., Hallab, N. J., Skipor, A. K., & Urban, R. M. (2003). Metal Degradation Products. *Clinical Orthopaedics & Related Research*, 417, 139–147. <https://doi.org/10.1097/01.blo.0000096810.78689.62>

Jafari, S., Singh Raman, R. K., & Davies, C. H. J. (2015). Corrosion fatigue of a magnesium alloy in modified

simulated body fluid. *Engineering Fracture Mechanics*, 137, 2–11. <https://doi.org/10.1016/j.engfracmech.2014.07.007>

Jang, Y., Collins, B., Sankar, J., & Yun, Y. (2013). Effect of biologically relevant ions on the corrosion products formed on alloy AZ31B: An improved understanding of magnesium corrosion. *Acta Biomaterialia*, 9(10), 8761–8770. <https://doi.org/10.1016/j.actbio.2013.03.026>

Kannan, M. B. (2010a). Influence of microstructure on the in-vitro degradation behaviour of magnesium alloys. *Materials Letters*, 64(6), 739–742. <https://doi.org/10.1016/j.matlet.2010.01.022>

Kiani, F., Lin, J., Munir, K., Wen, C., & Li, Y. (2023). Improvements in mechanical, corrosion, and biocompatibility properties of Mg–Zr–Sr–Dy alloys via extrusion for biodegradable implant applications. *Journal of Magnesium and Alloys*, 11(10), 3840–3865. <https://doi.org/10.1016/j.jma.2023.09.031>

Kim, B. H., Jo, S. M., Lee, Y. C., Park, Y. H., & Park, I. M. (2012). Microstructure, tensile properties and creep behavior of Mg–4Al–2Sn containing Ca alloy produced by different casting technologies. *Materials Science and Engineering: A*, 535, 40–47. <https://doi.org/10.1016/j.msea.2011.12.038>

Kraus, T., Fischerauer, S. F., Hänzli, A. C., Uggowitzer, P. J., Löffler, J. F., & Weinberg, A. M. (2012). Magnesium alloys for temporary implants in osteosynthesis: In vivo studies of their degradation and interaction with bone. *Acta Biomaterialia*, 8(3), 1230–1238. <https://doi.org/10.1016/j.actbio.2011.11.008>

Lamaka, S. V., Gonzalez, J., Mei, D., Feyerabend, F., Willumeit-Römer, R., & Zheludkevich, M. L. (2018). Local pH and Its Evolution Near Mg Alloy Surfaces Exposed to Simulated Body Fluids. *Advanced Materials Interfaces*, 5(18). <https://doi.org/10.1002/admi.201800169>

Lee, J. Y., Kim, D. H., Lim, H. K., & Kim, D. H. (2005a). Effects of Zn/Y ratio on microstructure and mechanical properties of Mg-Zn-Y alloys. *Materials Letters*, 59(29–30), 3801–3805. <https://doi.org/10.1016/j.matlet.2005.06.052>

Lhotka, C., Szekeres, T., Steffan, I., Zhuber, K., & Zweymüller, K. (2003). Four-year study of cobalt and chromium blood levels in patients managed with two different metal-on-metal total hip replacements. *Journal of Orthopaedic Research*, 21(2), 189–195. [https://doi.org/10.1016/S0736-0266\(02\)00152-3](https://doi.org/10.1016/S0736-0266(02)00152-3)

Li, J., Wang, F., Mao, P., & Liu, Z. (2015). Microstructure and mechanical properties of Mg-4Zn- x Y alloys prepared by hot-extrusion. *Journal of Materials Research*, 30(12), 1965–1972. <https://doi.org/10.1557/jmr.2015.146>

Li, L., Gao, J., & Wang, Y. (2004). Evaluation of cytotoxicity and corrosion behavior of alkali-heat-treated magnesium in simulated body fluid. *Surface and Coatings Technology*, 185(1), 92–98. <https://doi.org/10.1016/j.surfcoat.2004.01.004>

Li, W., Zhu, S., Sun, Y., & Guan, S. (2020). Microstructure and properties of biodegradable Mg-Zn-Y-Nd alloy micro-tubes prepared by an improved method. *Journal of Alloys and Compounds*, 835, 155369. <https://doi.org/10.1016/j.jallcom.2020.155369>

Li, Z., Gu, X., Lou, S., & Zheng, Y. (2008). The development of binary Mg–Ca alloys for use as biodegradable materials within bone. *Biomaterials*, 29(10), 1329–1344. <https://doi.org/10.1016/j.biomaterials.2007.12.021>

Liao, H., Kim, J., Lee, T., Song, J., Peng, J., Jiang, B., & Pan, F. (2020b). Effect of heat treatment on LPSO morphology and mechanical properties of Mg–Zn–Y–Gd alloys. *Journal of Magnesium and Alloys*, 8(4), 1120–1127. <https://doi.org/10.1016/j.jma.2020.06.009>

Liu, L. J., & Schlesinger, M. (2009). Corrosion of magnesium and its alloys. *Corrosion Science*, 51(8), 1733–1737. <https://doi.org/10.1016/j.corsci.2009.04.025>

Maguire, M. E., & Cowan, J. A. (2002). Magnesium chemistry and biochemistry. *BioMetals*, 15(3), 203–210. <https://doi.org/10.1023/A:1016058229972>

Meng, J., Sun, W., Tian, Z., Qiu, X., & Zhang, D. (2013). Corrosion performance of magnesium (Mg) alloys containing rare-earth (RE) elements. In *Corrosion Prevention of Magnesium Alloys* (pp. 38–60). Elsevier. <https://doi.org/10.1533/9780857098962.1.38>

Mueller, W.-D., Lucia Nascimento, M., & Lorenzo de Mele, M. F. (2010). Critical discussion of the results from different corrosion studies of Mg and Mg alloys for biomaterial applications☆. *Acta Biomaterialia*, 6(5), 1749–1755. <https://doi.org/10.1016/j.actbio.2009.12.048>

Nagels, J., Stokdijk, M., & Rozing, P. M. (2003). Stress shielding and bone resorption in shoulder arthroplasty. *Journal of Shoulder and Elbow Surgery*, 12(1), 35–39. <https://doi.org/10.1067/mse.2003.22>

Ng, W. F., Chiu, K. Y., & Cheng, F. T. (2010). Effect of pH on the in vitro corrosion rate of magnesium degradable implant material. *Materials Science and Engineering: C*, 30(6), 898–903. <https://doi.org/10.1016/j.msec.2010.04.003>

Nie, J.-F. (2012). Precipitation and Hardening in Magnesium Alloys. *Metallurgical and Materials Transactions A*, 43(11), 3891–3939. <https://doi.org/10.1007/s11661-012-1217-2>

Orlov, D., Ralston, K. D., Birbilis, N., & Estrin, Y. (2011). Enhanced corrosion resistance of Mg alloy ZK60 after processing by integrated extrusion and equal channel angular pressing. *Acta Materialia*, 59(15), 6176–6186. <https://doi.org/10.1016/j.actamat.2011.06.033>

Persaud-Sharma, D., & McGoron, A. (2012). Biodegradable Magnesium Alloys: A Review of Material Development and Applications. *Journal of Biomimetics, Biomaterials and Tissue Engineering*, 12, 25–39. <https://doi.org/10.4028/www.scientific.net/JBBTE.12.25>

Pu, Z., Outeiro, J. C., Batista, A. C., Dillon, O. W., Puleo, D. A., & Jawahir, I. S. (2011). Surface Integrity in Dry and Cryogenic Machining of AZ31B Mg Alloy with Varying Cutting Edge Radius Tools. *Procedia Engineering*, 19, 282–287. <https://doi.org/10.1016/j.proeng.2011.11.113>

Qian, M., & Das, A. (2006a). Grain refinement of magnesium alloys by zirconium: Formation of equiaxed grains. *Scripta Materialia*, 54(5), 881–886. <https://doi.org/10.1016/j.scriptamat.2005.11.002>

Radha, R., & Sreekanth, D. (2017). Insight of magnesium alloys and composites for orthopedic implant

applications – a review. *Journal of Magnesium and Alloys*, 5(3), 286–312. <https://doi.org/10.1016/j.jma.2017.08.003>

Rosalbino, F., De Negri, S., Scavino, G., & Saccone, A. (2013). Microstructure and *in vitro* degradation performance of Mg–Zn–Mn alloys for biomedical application. *Journal of Biomedical Materials Research Part A*, 101A(3), 704–711. <https://doi.org/10.1002/jbm.a.34368>

Seal, C. K., Vince, K., & Hodgson, M. A. (2009). Biodegradable surgical implants based on magnesium alloys – A review of current research. *IOP Conference Series: Materials Science and Engineering*, 4, 012011. <https://doi.org/10.1088/1757-899X/4/1/012011>

Shi, Y., Liu, X.-Q., Liu, Z.-L., Xie, H.-J., Wang, Y.-H., & Li, J. (2022). Effect of Zn content on corrosion behavior of Mg-Y-Zn alloys. *Journal of Mining and Metallurgy, Section B: Metallurgy*, 58(1), 51–61. <https://doi.org/10.2298/JMMB210525048S>

SHIRI, M., JAFARI, H., & SINGH, R. (2022). Effect of extrusion parameters on degradation of magnesium alloys for bioimplant applications: A review. *Transactions of Nonferrous Metals Society of China*, 32(9), 2787–2813. [https://doi.org/10.1016/S1003-6326\(22\)65984-3](https://doi.org/10.1016/S1003-6326(22)65984-3)

Silcock, J. M. (1982). Nucleation and Growth of Stress Corrosion Cracks in Austenitic Steels with Varying Ni and Mo Contents. *Corrosion*, 38(3), 144–156. <https://doi.org/10.5006/1.3579267>

Singh Raman, R. K., & Choudhary, L. (2013). Cracking of magnesium-based biodegradable implant alloys under the combined action of stress and corrosive body fluid: a review.

Emerging Materials Research, 2(5), 219–228.
<https://doi.org/10.1680/emr.13.00033>

Song, G. L., & Atrens, A. (1999). Corrosion Mechanisms of Magnesium Alloys. *Advanced Engineering Materials*, 1(1), 11–33. [https://doi.org/10.1002/\(SICI\)1527-2648\(199909\)](https://doi.org/10.1002/(SICI)1527-2648(199909)1(1)11::AID-AEAM11<1.0.CO;2-1)

Song, G., & Song, S. (2007a). A Possible Biodegradable Magnesium Implant Material. *Advanced Engineering Materials*, 9(4), 298–302.
<https://doi.org/10.1002/adem.200600252>

Staiger, M. P., Pietak, A. M., Huadmai, J., & Dias, G. (2006). Magnesium and its alloys as orthopedic biomaterials: A review. *Biomaterials*, 27(9), 1728–1734.
<https://doi.org/10.1016/j.biomaterials.2005.10.003>

StJohn, D. H., Qian, M., Easton, M. A., Cao, P., & Hildebrand, Z. (2005). Grain refinement of magnesium alloys. *Metallurgical and Materials Transactions A*, 36(7), 1669–1679.
<https://doi.org/10.1007/s11661-005-0030-6>

Tahreem, N., & Chen, D. L. (2016a). A Critical Review of Mg–Zn–Y Series Alloys Containing I, W, and LPSO Phases. *Advanced Engineering Materials*, 18(12), 1983–2002.
<https://doi.org/10.1002/adem.201600393>

Tang, B., Wang, X.-S., Li, S.-S., Zeng, D.-B., & Wu, R. (2005). Effects of Ca combined with Sr additions on microstructure and mechanical properties of AZ91D magnesium alloy. *Materials Science and Technology*, 21(5), 574–578. <https://doi.org/10.1179/174328405X43180>

Tang, Y.-C., Katsuma, S., Fujimoto, S., & Hiromoto, S. (2006). Electrochemical study of Type 304 and 316L stainless steels in simulated body fluids and cell cultures. *Acta*

Biomaterialia, 2(6), 709–715.
<https://doi.org/10.1016/j.actbio.2006.06.003>

Tsakiris, V., Tardei, C., & Clicinschi, F. M. (2021a). Biodegradable Mg alloys for orthopedic implants – A review. *Journal of Magnesium and Alloys*, 9(6), 1884–1905. <https://doi.org/10.1016/j.jma.2021.06.024>

Veleva, L., Fernández-Olaya, M. G., & Feliu, S. (2018). Initial Stages of AZ31B Magnesium Alloy Degradation in Ringer’s Solution: Interpretation of EIS, Mass Loss, Hydrogen Evolution Data and Scanning Electron Microscopy Observations. *Metals*, 8(11), 933. <https://doi.org/10.3390/met8110933>

Walker, J., Shadanbaz, S., Kirkland, N. T., Stace, E., Woodfield, T., Staiger, M. P., & Dias, G. J. (2012). Magnesium alloys: Predicting *in vivo* corrosion with *in vitro* immersion testing. *Journal of Biomedical Materials Research Part B: Applied Biomaterials*, 100B(4), 1134–1141. <https://doi.org/10.1002/jbm.b.32680>

Wang, H., & Shi, Z. (2011). *In vitro* biodegradation behavior of magnesium and magnesium alloy. *Journal of Biomedical Materials Research Part B: Applied Biomaterials*, 98B(2), 203–209. <https://doi.org/10.1002/jbm.b.31769>

Wang, J., Jiang, W., Guo, S., Li, Y., & Ma, Y. (2018). The Effect of Rod-Shaped Long-Period Stacking Ordered Phases Evolution on Corrosion Behavior of Mg_{95.33}Zn₂Y_{2.67} Alloy. *Materials*, 11(5), 815. <https://doi.org/10.3390/ma11050815>

Wang, L., Li, J. B., Li, L., Nie, K. B., Zhang, J. S., Yang, C. W., Yan, P. W., Liu, Y. P., & Xu, C. X. (2017). Microstructure, mechanical and bio-corrosion properties of Mg–Zn–Zr alloys

with minor Ca addition. *Materials Science and Technology*, 33(1), 9–16. <https://doi.org/10.1080/02670836.2016.1152348>

Witte, F. (2010a). The history of biodegradable magnesium implants: A review☆. *Acta Biomaterialia*, 6(5), 1680–1692. <https://doi.org/10.1016/j.actbio.2010.02.028>

Witte, F., Fischer, J., Nellesen, J., Crostack, H.-A., Kaese, V., Pisch, A., Beckmann, F., & Windhagen, H. (2006). In vitro and in vivo corrosion measurements of magnesium alloys. *Biomaterials*, 27(7), 1013–1018. <https://doi.org/10.1016/j.biomaterials.2005.07.037>

Witte, F., Hort, N., Vogt, C., Cohen, S., Kainer, K. U., Willumeit, R., & Feyerabend, F. (2008). Degradable biomaterials based on magnesium corrosion. *Current Opinion in Solid State and Materials Science*, 12(5–6), 63–72. <https://doi.org/10.1016/j.cossms.2009.04.001>

Witte, F., Kaese, V., Haferkamp, H., Switzer, E., Meyer-Lindenberg, A., Wirth, C. J., & Windhagen, H. (2005a). In vivo corrosion of four magnesium alloys and the associated bone response. *Biomaterials*, 26(17), 3557–3563. <https://doi.org/10.1016/j.biomaterials.2004.09.049>

Wong, H. M., Yeung, K. W. K., Lam, K. O., Tam, V., Chu, P. K., Luk, K. D. K., & Cheung, K. M. C. (2010). A biodegradable polymer-based coating to control the performance of magnesium alloy orthopaedic implants. *Biomaterials*, 31(8), 2084–2096. <https://doi.org/10.1016/j.biomaterials.2009.11.111>

Wu, J., Chiu, Y. L., & Jones, I. P. (2014). Microstructure of as-cast Mg-4.2Zn-0.8Y (at.%) alloys containing Gd. *Journal of Physics: Conference Series*, 522, 012033. <https://doi.org/10.1088/1742-6596/522/1/012033>

Wu, X., Jiang, Q., Geng, Y., Liu, N., Li, M., Duan, J., & Hou, B. (2024). The microstructure and corrosion resistance of Mg–Zn–0.5Ag–xCa (x=0, 0.5, 1.0, 1.5 wt%) alloys in Hank's solution. *Journal of Materials Research and Technology*, *30*, 5869–5880. <https://doi.org/10.1016/j.jmrt.2024.05.031>

Xin, Y., Hu, T., & Chu, P. K. (2010). Influence of Test Solutions on In Vitro Studies of Biomedical Magnesium Alloys. *Journal of The Electrochemical Society*, *157*(7), C238. <https://doi.org/10.1149/1.3421651>

Xin, Y., Huo, K., Tao, H., Tang, G., & Chu, P. K. (2008b). Influence of aggressive ions on the degradation behavior of biomedical magnesium alloy in physiological environment. *Acta Biomaterialia*, *4*(6), 2008–2015. <https://doi.org/10.1016/j.actbio.2008.05.014>

Yamamoto, A., & Hiromoto, S. (2009). Effect of inorganic salts, amino acids and proteins on the degradation of pure magnesium in vitro. *Materials Science and Engineering: C*, *29*(5), 1559–1568. <https://doi.org/10.1016/j.msec.2008.12.015>

Yamasaki, M., Hashimoto, K., Hagihara, K., & Kawamura, Y. (2010a). Multimodal Microstructure Evolution in Wrought Mg–Zn–Y Alloys with High Strength and Increased Ductility. *Materials Science Forum*, *654–656*, 615–618. <https://doi.org/10.4028/www.scientific.net/MSF.654-656.615>

Yamasaki, M., & Kawamura, Y. (2009). Thermal diffusivity and thermal conductivity of Mg–Zn–rare earth element alloys with long-period stacking ordered phase. *Scripta Materialia*, *60*(4), 264–267. <https://doi.org/10.1016/j.scriptamat.2008.10.022>

Yamasaki, M., Shi, Z., Atrens, A., Furukawa, A., & Kawamura, Y. (2022). Influence of crystallographic orientation and Al alloying on the corrosion behaviour of extruded α -Mg/LPSO two-phase Mg-Zn-Y alloys with multimodal microstructure. *Corrosion Science*, 200, 110237. <https://doi.org/10.1016/j.corsci.2022.110237>

Yang, H., Wu, L., Jiang, B., Liu, W., Xie, H., Song, J., Huang, G., Zhang, D., & Pan, F. (2020a). Effect of Microstructure on the Corrosion Behavior of as-cast and Extruded Mg-Sn-Y Alloys. *Journal of The Electrochemical Society*, 167(12), 121503. <https://doi.org/10.1149/1945-7111/abab27>

Yin, J., Li, M., Yi, F., Zhao, X., Guan, D., Wang, K., Gao, Y., & Liu, C. (2024). Effects of micro-alloying Ag on microstructure, mechanical properties and corrosion behavior of extruded Mg-2Zn-0.2Ca-xAg alloys. *Journal of Alloys and Compounds*, 989, 174376. <https://doi.org/10.1016/j.jallcom.2024.174376>

Yin, S., Duan, W., Liu, W., Wu, L., Yu, J., Zhao, Z., Liu, M., Wang, P., Cui, J., & Zhang, Z. (2020). Influence of specific second phases on corrosion behaviors of Mg-Zn-Gd-Zr alloys. *Corrosion Science*, 166, 108419. <https://doi.org/10.1016/j.corsci.2019.108419>

Yoshimoto, S., Yamasaki, M., & Kawamura, Y. (2006). Microstructure and Mechanical Properties of Extruded Mg-Zn-Y Alloys with 14H Long Period Ordered Structure. *MATERIALS TRANSACTIONS*, 47(4), 959–965. <https://doi.org/10.2320/matertrans.47.959>

Zainal Abidin, N. I., Martin, D., & Atrens, A. (2011). Magnesium Corrosion in Different Solutions. *Materials*

Science Forum, 690, 369–372.
<https://doi.org/10.4028/www.scientific.net/MSF.690.369>

Zengin, H., & Turen, Y. (2020). Effect of Y addition on microstructure and corrosion behavior of extruded Mg–Zn–Nd–Zr alloy. *Journal of Magnesium and Alloys*, 8(3), 640–653. <https://doi.org/10.1016/j.jma.2020.06.004>

Zhang, X. B., Yuan, G. Y., & Wang, Z. Z. (2013). Effects of extrusion ratio on microstructure, mechanical and corrosion properties of biodegradable Mg–Nd–Zn–Zr alloy. *Materials Science and Technology*, 29(1), 111–116. <https://doi.org/10.1179/1743284712Y.0000000107>

Zhang, X., Du, B., & Cao, Y. (2023). Study on Microstructural Evolution and Mechanical Properties of Mg-3Sn-1Mn-xLa Alloy by Backward Extrusion. *Materials*, 16(13), 4588. <https://doi.org/10.3390/ma16134588>

Zheng, Y. F., Gu, X. N., & Witte, F. (2014). Biodegradable metals. *Materials Science and Engineering: R: Reports*, 77, 1–34. <https://doi.org/10.1016/j.msre.2014.01.001>

Zhou, J., Zhang, X., Li, Q., Liu, Y., Chen, F., & Li, L. (2013). Effect of the physiological stabilization process on the corrosion behaviour and surface biocompatibility of AZ91D magnesium alloy. *Journal of Materials Chemistry B*, 1(45), 6213. <https://doi.org/10.1039/c3tb20960>

CHAPTER 5

Artificial Intelligence Based Applications in Materials and Metallurgy

NİDA KATI¹
FERHAT UÇAR²

Introduction

Materials science is one of the cornerstones of technological advances in human history. From the forging of iron in ancient times to superconductors and nanomaterials in the modern era, the discovery and optimization of new materials has revolutionized many fields such as energy, healthcare, transportation and information technology. However, traditional materials science methods often rely on time-consuming, costly and trial-and-error-based processes. In recent years, the integration of artificial intelligence (AI) technologies into materials science has begun to radically transform these processes. AI is taking materials science into a new era, offering unparalleled speed and accuracy in areas such as materials discovery, design simulations, process optimization and property prediction. The applications of AI in

¹ Assoc.Prof., Firat University, Faculty of Technology, Metallurgical and Materials Engineering, Orcid: 0000-0001-7953-1258

² Assoc.Prof., Firat University, Faculty of Technology, Software Engineering, Orcid:0000-0001-9366-6124

materials science not only accelerate existing processes, but also enable innovative solutions that were previously inaccessible.

Artificial intelligence-powered materials science is creating a revolutionary transformation in materials research and development processes today (Bai & Zhang, 2025). The capability of machine learning algorithms to automatically solve complex tasks significantly accelerates the discovery of materials, understanding of their properties, and development of new materials (Fang et al., 2022). This interdisciplinary approach offers a wide range of applications from the discovery of stable materials to crystal structure prediction, from the development of machine learning-assisted force fields to optimization processes with active learning (Schmidt, Marques, Botti, & Marques, 2019). Computational Materials Combined with high-performance computing resources and cloud technologies, this approach can screen millions of material candidates to predict hundreds of thousands of potentially stable materials (Chen et al., 2024). These developments support material optimization and innovative design processes in a wide variety of applications from energy storage systems to clean energy technologies, from electrochemical systems to nanomaterials, playing a critical role in the development of sustainable technologies (Maqsood, Chen, & Jacobsson, 2024).

Artificial intelligence technologies are fundamentally transforming metallurgical production by facilitating advanced process automation and real-time optimization that drives unprecedented levels of operational efficiency and sustainability (Cao, Bambach, Merklein, Mozaffar, & Xue, 2024). Machine learning algorithms enable predictive maintenance systems to analyze massive datasets from industrial sensors, identifying equipment degradation patterns and predicting failures before they occur, thereby minimizing unplanned downtime and extending machinery lifespan (Çinar et al., 2020). Digital twin technologies

integrated with artificial intelligence create virtual representations of metallurgical processes, enabling precise control optimization and virtual testing scenarios that eliminate unnecessary costs while improving product quality and consistency (Waltersmann, Kiemel, Stuhlsatz, Sauer, & Miehe, 2021). Processing MThis integration of AI in metallurgy supports knowledge extraction and enables optimal process management, fostering enhanced flexibility, stronger resource efficiency, and ultimately advancing the industry toward intelligent, sustainable manufacturing paradigms essential for addressing global environmental challenges (Colla, 2022).

In this case, the application of AI not only increases operational effectiveness but also stimulates alloy design and material property innovation, paving the way for revolutionary developments in the sector (Bouiti et al., 2025; Ikenson, 2025).

All things considered, the combination of artificial intelligence (AI) with materials engineering and metallurgy is changing the field of material science and opening the door for new developments that could improve sustainability and efficiency in a range of sectors. Overcoming current obstacles and advancing the development of materials in the future will require continued research and cooperation between scientists, engineers, and business executives as this integration develops (Jiang et al., 2025).

The relationship between engineering design and material attributes grew stronger over time, providing a strong basis for integrating new technologies like artificial intelligence. The field has changed much more because artificial intelligence was recently introduced into materials research. By evaluating vast datasets, spotting patterns, and automating procedures, artificial intelligence (AI) technology started to make material discovery and optimization easier (“Artificial Intelligence for Metallurgical Industry,” 2025).

This study aims to comprehensively address the current status, key application areas and future potential of AI in materials science. In our study, we explore in detail how artificial intelligence is reshaping the landscape of materials science, particularly in the fields of materials engineering and metallurgy. First, we examine how AI accelerates material discovery and design processes, enabling breakthroughs previously thought impossible. Subsequently, we delve into practical AI-driven applications, highlighting significant advancements in materials engineering and metallurgical processes. Finally, we discuss the extensive benefits and inherent challenges posed by integrating AI into these disciplines, providing a comprehensive framework for researchers, engineers, and industry professionals seeking to navigate and contribute to this rapidly evolving field.

Figure 1 presents a comprehensive visual summary of the thematic structure covered in this chapter, illustrating the sequential flow of key topics related to the integration of artificial intelligence in materials science and engineering. It begins with the role of AI in accelerating material discovery and inverse design, then expands into its diverse applications within materials engineering—such as smart material development, advanced characterization, and process optimization. The diagram further highlights the transformative impact of AI in metallurgy, including alloy design, energy efficiency, and predictive maintenance. The latter sections focus on the broader benefits and challenges associated with AI adoption, including data quality concerns, interpretability, and the need for educational support. The chapter concludes by outlining future perspectives, emphasizing collaboration, education, and alignment with global sustainability goals.

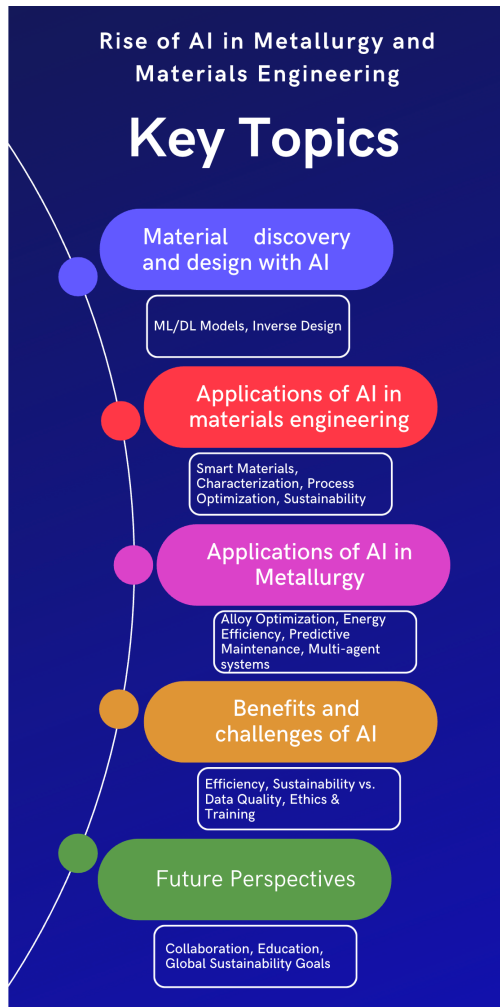


Figure 1. General flowchart depicting key topics covered in this chapter regarding the integration and applications of artificial intelligence in materials engineering and metallurgy.

2. Material discovery and design with AI

Materials science continues to push humanity's technological boundaries through the discovery and design of new materials. From superconductors to nanomaterials, energy storage systems to biomedical applications, understanding and optimizing the chemical

and physical properties of materials is a cornerstone of modern technology. However, traditional methods of materials discovery often rely on labor-intensive, time-consuming and costly processes. Trial-and-error-based approaches are insufficient to screen millions of possible compositions, while the efficiency and speed of these processes struggle to meet contemporary demands. This is where AI is emerging as a revolution that is radically transforming materials discovery and design.

AI accelerates the discovery of new materials and predicts material properties with high accuracy by analyzing large data sets with technologies such as machine learning, deep learning and graph neural networks (GNN). In DeepMind's Graph Neural Network Based Materials Discovery (GNoME) project, 380,000 new stable materials have been identified using graph neural networks (GNN) and density functional theory (DFT) simulations. These materials include potential superconductors and innovative compositions for energy storage. Thanks to this project, discovery processes that could take years with traditional methods are reduced to weeks or days ("Google DeepMind," 2025).

IBM's RXN for Chemistry project has streamlined material synthesis processes by integrating AI into laboratory automation. Thus, with models and robotic systems that predict chemical reactions, the synthesis of new materials has accelerated. It has reduced human error in experimental processes and increased reproducibility ("IBM RXN," 2025).

The Open Catalyst Project uses AI to discover catalyst materials for carbon capture and clean energy applications. With large data sets and machine learning models, surface properties and reactivity of catalysts are predicted. Thus, the development of materials that offer solutions to environmental problems is accelerated ("Open Catalyst," 2020)

Citrine Informatics supports material discovery and optimization processes by offering an AI-based platform. He uses machine learning models to predict material properties and recommend optimal compositions (“Citrine,” 2013).

Similarly, AI-based reverse design approaches are being used to design materials with specific properties from scratch, thus optimizing targeted materials development processes. These technologies not only accelerate discovery processes, but also offer the possibility to explore previously inaccessible combinations of chemical composition and structure.

3. Applications of AI in materials engineering

In materials engineering, AI has become a disruptive force that improves a number of procedures related to material design, synthesis, and characterization. Significant breakthroughs in a number of fields are made possible by the integration of AI technologies, which promotes increased productivity, creativity, and sustainability.

The application of AI algorithms to create materials that are suited to particular requirements and performance standards is growing. For example, materials with improved mechanical qualities for challenging settings, including heat-resistant materials for industrial processes or high-strength alloys for aerospace applications, can be predicted and optimized using machine learning (ML) approaches (“Revolutionizing Materials,” 2024). AI also makes it easier to create "smart" materials, which react dynamically to outside stimuli and have uses in wearable technology, robotics, and healthcare.

AI has a significant impact on material characterisation, especially when it comes to automating data interpretation from sophisticated imaging methods like atomic force microscopy (AFM) and scanning electron microscopy (SEM). Large volumes of data can

be processed using deep learning algorithms, enabling effective microstructure categorization, defect prediction, and material quality evaluation (Ikenson, 2025). This capability improves the accuracy and dependability of characterization efforts by drastically cutting down on the time and effort typically needed for manual analysis.

By evaluating real-time data from sensors during production, AI increases process efficiency in manufacturing. AI helps optimize these procedures to minimize flaws, improve consistency, and cut down on waste. Even minor changes in parameters can result in noticeable variations in product quality. In fields where accuracy is crucial, like metallurgy, polymers, and ceramics, this optimization is extremely beneficial (Bouiti et al., 2025).

AI is also essential to the high-throughput search for novel and sustainable materials. Materials with desirable environmental qualities, such recyclability and lower production energy usage, can be identified using AI algorithms. Researchers are investigating novel material categories targeted at lowering carbon footprints in sectors like steel production by fusing experimental validation with AI-driven screening techniques (“AI Materials Science,” 2025).

By facilitating the examination of large databases of material properties, machine learning has revolutionized materials discovery by empowering researchers to quickly identify and forecast materials with particular attributes. This method speeds up the entire development cycle and greatly reduces the need for intensive laboratory testing by speeding up the discovery phase. Moreover, researchers can now accurately forecast how materials will behave in a variety of settings, including harsh ones, because to AI’s capacity to manage complicated and high-dimensional data (Benardos, 2025).

4. Applications of AI in Metallurgy

Traditional methods have been completely transformed by the incorporation of AI technologies into a variety of metallurgical applications, which have also increased the efficiency and quality of metal production.

Manufacturers can detect bottlenecks and streamline operations by using machine learning algorithms to evaluate large datasets, which will increase efficiency and decrease waste. As an illustration of the potential of AI in optimizing energy use across manufacturing plants, ArcelorMittal's application of the technology has led to a noteworthy 5% reduction in energy usage during steel production. Furthermore, ordinary jobs may be managed more easily with AI-driven automation, freeing up expert individuals to concentrate on more difficult problem-solving, which enhances production processes overall ("How Artificial Intelligence," 2025) (Cau, 2025)("Revolutionizing Aluminum Alloy," 2024)

Predictive maintenance, which uses real-time data analytics to anticipate equipment breakdowns and save downtime, is another important use of AI in metallurgy. This proactive strategy improves operational efficiency and prolongs the life of machinery. Furthermore, by using its sophisticated data analysis and pattern recognition capabilities, AI improves quality control (Cau, 2025; "How Artificial Intelligence," 2025).

Additionally, AI is advancing alloy design, especially with multi-agent systems that let multiple autonomous agents to work together to solve problems. Finding the best alloy formulas and effectively exploring compositional spaces are made possible by this cooperative framework. Alloy compositions are refined using methods like Bayesian optimization and genetic algorithms, which guarantee a balance between cost and performance. Furthermore, AI-driven frameworks enable the simultaneous optimization of several

features, expanding the alloy design's capabilities to satisfy more demanding application needs (Lu et al., 2024; "Revolutionizing Aluminum Alloy," 2024).

In order to achieve greener steel-making methods, AI algorithms help optimize production procedures, which results in lower energy usage and emissions. For example, Toyota has reduced its energy consumption by 15% as a result of AI-supported energy management programs. AI's contribution to reducing environmental impact and promoting resource efficiency has grown critical as industry place a greater emphasis on sustainability (Cau, 2025; "How Artificial Intelligence," 2025).

5. Benefits and challenges of AI in Materials Engineering

By boosting efficiency and encouraging creativity, the application of AI in materials engineering is transforming the discipline. Significant productivity gains are reported by researchers using AI-assisted techniques; some cite increases of up to 44%, while patent filings have increased by 39% ("AI and Material Science," 2024).

AI technologies simplify the modeling and synthesis procedures, allowing researchers to more easily create domain-specific materials models and express complex simulation requirements in normal language. For example, researchers have successfully navigated complex materials environments and adhered to a variety of restrictions by merging machine learning and Integrated Computational Materials Engineering (ICME) in a hybrid approach ("Harnessing," 2024) AI also facilitates the creation of sustainable materials by identifying alternatives with better recyclability and less of an adverse effect on the environment. This possibility is consistent with more general global issues such as resource depletion and climate change. AI can help improve supply

chain management by forecasting demand and cutting waste, which boosts operational effectiveness even more.

The application of AI in materials engineering poses a number of difficulties despite its many benefits. The quality and variety of data, which frequently include noise and unbalanced classes that make machine learning model training more difficult, is a major obstacle (“GE Vernova,” 2024). Another major worry is the interpretability of AI algorithms; since many models operate as “black boxes” they raise questions about accountability, ethics, and transparency in decision-making processes (“Markus Buehler,” 2024). To promote confidence and evaluate the predictions provided by AI systems, researchers stress the importance of creating interpretable AI algorithms. Additionally, integrating AI calls for specific education and training programs to give researchers and engineers the abilities they need, such as understanding data analysis and machine learning methodologies. Investment in educational infrastructure is essential to guaranteeing that professionals are equipped to handle this changing environment as the use of AI in materials science increases.

Conclusion

The integration AI in materials engineering and metallurgy signifies a transformative paradigm shift, substantially enhancing traditional methodologies. AI technologies are proving invaluable in rapidly identifying and optimizing new materials, significantly reducing the time, cost, and labor associated with traditional trial-and-error approaches. By analyzing extensive datasets, AI facilitates predictive insights, enabling researchers and manufacturers to efficiently design, synthesize, and characterize materials with unprecedented accuracy.

AI-driven advancements in alloy design, catalysis, energy storage, and smart materials have tangible implications for numerous

sectors, including aerospace, automotive, renewable energy, healthcare, and environmental sustainability. By automating material characterization processes, such as those involving sophisticated imaging techniques, AI ensures higher accuracy, consistency, and reliability while significantly reducing manual labor and potential for human error.

Manufacturing and production environments particularly benefit from AI by leveraging predictive maintenance, process optimization, and real-time quality control mechanisms, resulting in increased operational efficiency, reduced resource wastage, and minimized environmental footprints. Notably, industries adopting AI-driven methodologies have reported remarkable improvements, such as reductions in energy usage and enhancements in overall sustainability.

Nevertheless, the adoption of AI technologies in materials engineering is not devoid of challenges. Issues such as ensuring high-quality, representative datasets, addressing the interpretability and transparency of AI models, and developing adequate educational frameworks to equip researchers and professionals with essential AI competencies are critical areas needing attention. Moreover, ethical considerations surrounding data use and algorithmic decision-making processes require comprehensive policy frameworks and guidelines.

Looking forward, continued investment in research infrastructure, fostering interdisciplinary collaborations among data scientists, materials engineers, policymakers, and industry stakeholders, and prioritizing educational initiatives will be essential. Such integrated efforts will help overcome existing barriers, accelerate the adoption of AI methodologies, and maximize their potential for societal benefit.

Ultimately, AI's integration into materials engineering and metallurgy promises not only accelerated innovation but also significant contributions towards achieving global sustainability goals. By effectively addressing current limitations, we can unlock unprecedented opportunities, paving the way for next-generation technological advancements that profoundly enhance our quality of life and environmental stewardship.

References

AI and Material Science. (2024). Retrieved June 17, 2025, from <https://timothy-urista.medium.com/ai-and-material-science-unequal-benefits-for-researchers-and-implications-for-innovation-gaps-233de99f8289>

AI Materials Science. (2025). Retrieved June 17, 2025, from https://www.mpie.de/4867299/artificial_intelligence

Artificial Intelligence for Metallurgical Industry. (2025). Retrieved June 16, 2025, from <https://www.mheavytechnology.com/solutions/ai-in-the-metals-industry/>

Bai, X., & Zhang, X. (2025). Artificial Intelligence-Powered Materials Science. *Nano-Micro Letters 2025 17:1*, 17(1), 1–30. <https://doi.org/10.1007/S40820-024-01634-8>

Benardos, P. (2025). Advanced Applications of Artificial Intelligence in Metallic Materials Processing. *Metals 2025, Vol. 15*, Page 153, 15(2), 153. <https://doi.org/10.3390/MET15020153>

Bouiti, K., El Hamdouni, Y., Labjar, N., Labjar, H., Lagmiri, S. N., Nasrellah, H., & El Hajjaji, S. (2025). Materials Engineering and Artificial Intelligence Innovations: A Comprehensive Review. *Journal of Materials Engineering and Performance 2025 34:10*, 34(10), 8335–8349. <https://doi.org/10.1007/S11665-025-11040-9>

Cao, J., Bambach, M., Merklein, M., Mozaffar, M., & Xue, T. (2024). Artificial intelligence in metal forming. *CIRP Annals*, 73(2), 561–587. <https://doi.org/10.1016/J.CIRP.2024.04.102>

Cau, R. (2025). Smart Automation in Metallurgy: How AI Is Revolutionizing the Metallurgical Industry. *Iconic Research And Engineering Journals*, 8(10), 218–221. <https://doi.org/10.1155/2021/5592878>

Chen, C., Nguyen, D. T., Lee, S. J., Baker, N. A., Karakoti, A. S., Lauw, L., ... Troyer, M. (2024). Accelerating Computational Materials Discovery with Machine Learning and Cloud High-Performance Computing: from Large-Scale Screening to Experimental Validation. *Journal of the American Chemical Society*, 146(29), 20009–20018. https://doi.org/10.1021/JACS.4C03849/SUPPL_FILE/JA4C03849_SI_001.PDF

Çinar, Z. M., Nuhu, A. A., Zeeshan, Q., Korhan, O., Asmael, M., & Safaei, B. (2020). Machine Learning in Predictive Maintenance towards Sustainable Smart Manufacturing in Industry 4.0. *Sustainability 2020, Vol. 12, Page 8211*, 12(19), 8211. <https://doi.org/10.3390/SU12198211>

Citrine. (2013). Retrieved June 16, 2025, from <https://citrine.io/>

Colla, V. (2022). A big step ahead in Metal Science and Technology through the application of Artificial Intelligence. *IFAC-PapersOnLine*, 55(21), 1–6. <https://doi.org/10.1016/J.IFACOL.2022.09.234>

Fang, J., Xie, M., He, X., Zhang, J., Hu, J., Chen, Y., ... Jin, Q. (2022). Machine learning accelerates the materials discovery. *Materials Today Communications*, 33, 104900. <https://doi.org/10.1016/J.MTCOMM.2022.104900>

GE Vernova. (2024). Retrieved June 17, 2025, from <https://www.governova.com/software/blog/challenges-best-practices-in-industrial-artificial-intelligence>

Google DeepMind. (2025). Retrieved June 16, 2025, from <https://deepmind.google/>

Harnessing. (2024). Retrieved June 17, 2025, from <https://questek.com/harnessing-the-power-of-ai-in-materials-digital-transformation-a-synergistic-hybrid-approach/>

How artificial intelligence. (2025). Retrieved June 17, 2025, from <https://www.complizen.ai/post/how-artificial-intelligence-can-assist-the-metallurgy-industry-to-optimize-supporting-processes-in>

IBM RXN. (2025). Retrieved June 16, 2025, from <https://rxn.res.ibm.com/rxn/robo-rxn/welcome>

Ikenson, B. (2025). The paradigm-shifting potential of AI in materials science. *Scilight*, 2025(24). <https://doi.org/10.1063/10.0036918>

Jiang, X., Xue, D., Bai, Y., Wang, W. Y., Liu, J., Yang, M., & Su, Y. (2025). AI4Materials: Transforming the landscape of materials science and engineering. *Review of Materials Research*, 1(1), 100010. <https://doi.org/10.1016/J.REVMAT.2025.100010>

Lu, Z., Kapoor, I., Li, Y., Liu, Y., Zeng, X., & Wang, L. (2024). Machine learning driven design of high-performance Al alloys. *J Mater Inf* 2024;4:19., 4(4), N/A-N/A. <https://doi.org/10.20517/JMI.2024.21>

Maqsood, A., Chen, C., & Jacobsson, T. J. (2024). The Future of Material Scientists in an Age of Artificial Intelligence. *Advanced Science*, 11(19), 2401401. <https://doi.org/10.1002/ADVS.202401401>

Markus Buehler. (2024). Retrieved June 13, 2025, from <https://professional.mit.edu/news/articles/revolutionizing-materials-science-interview-markus-buehler-impact-ai>

Open Catalyst. (2020). Retrieved June 16, 2025, from <https://opencatalystproject.org/>

Revolutionizing Aluminum Alloy. (2024). Retrieved June 17, 2025, from <https://texametals.com/blog/revolutionizing-aluminum-alloy-research-with-machine-learning/>

Revolutionizing Materials. (2024). Retrieved June 16, 2025, from <https://professional.mit.edu/news/articles/revolutionizing-materials-science-interview-markus-buehler-impact-ai>

Schmidt, J., Marques, M. R. G., Botti, S., & Marques, M. A. L. (2019). Recent advances and applications of machine learning in solid-state materials science. *Npj Computational Materials* 2019 5:1, 5(1), 1–36. <https://doi.org/10.1038/s41524-019-0221-0>

Waltersmann, L., Kiemel, S., Stuhlsatz, J., Sauer, A., & Mieke, R. (2021). Artificial Intelligence Applications for Increasing Resource Efficiency in Manufacturing Companies—A Comprehensive Review. *Sustainability* 2021, Vol. 13, Page 6689, 13(12), 6689. <https://doi.org/10.3390/SU13126689>

CHAPTER 6

Artificial Intelligence Driven Image Analyzes in Material Science

NİDA KATI¹
FERHAT UÇAR²

Introduction

Artificial intelligence (AI) has become a transformative tool for materials science in the field of image analysis. The processing and interpretation of complex visual data from microscopy, spectroscopy and other imaging techniques has revolutionized areas such as characterization of materials, prediction of their properties, and design of new structures (Goodfellow et.al., 2016). This study examines the methodologies, applications and future potential of AI-based image analysis in materials science. By leveraging machine learning (ML) and deep learning (DL) algorithms, scientists are now able to extract meaningful insights from high-dimensional data sets,

¹ Assoc. Prof., Firat University, Faculty of Technology, Metallurgical and Materials Engineering, Orcid: 0000-0001-7953-1258

²Assoc. Prof., Firat University, Faculty of Technology, Software Engineering, Orcid:0000-0001-9366-6124

accelerating advances in fields such as nanotechnology, metallurgy and polymer science.

Materials science is highly dependent on imaging techniques such as scanning electron microscopy (SEM), transmission electron microscopy (TEM), atomic force microscopy (AFM) and X-ray diffraction (XRD). These techniques are used to study the microstructure, composition and properties of materials and generate large amounts of image data. Traditionally, the analysis of these images is done manually by experts. However, manual analysis is time-consuming, subjective and prone to human error, especially when dealing with large data sets or fine patterns (Stuckner, Harder, and Smith 2022)

AI-based image analysis overcomes these challenges by automatically extracting features, identifying patterns, and correlating visual data with material properties. Techniques such as convolutional neural networks (CNN), generative adversarial networks (GAN), and unsupervised learning have proven effective in tasks such as defect detection, phase segmentation, and grain boundary analysis (Davydzenka et al. 2022).

The structure of the AI applications in this field follows a logical progression that reflects the typical pipeline of AI-assisted image analysis in materials science. As illustrated in Figure 1, the workflow begins with the acquisition and annotation of imaging data using techniques such as SEM, TEM, and EBSD. This is followed by preprocessing and feature engineering, which prepare the data for model development by enhancing quality and extracting relevant information. The next stage focuses on the design and training of AI models—primarily convolutional architectures—tailored to specific materials characterization tasks. Subsequently, these models are deployed across various application domains, including

microstructure segmentation, defect detection, phase identification, and property prediction. Finally, the performance of these models is evaluated through quantitative metrics and tested for generalizability under real-world conditions. This figure provides a conceptual map for the image analysis driven AI applications in materials science, highlighting the relationships between the technical components and their roles in the overall analytical framework.

A Structured Workflow for AI-Driven Image Analysis in Materials Characterization

An End-to-End Representation from Data Acquisition to Model Evaluation

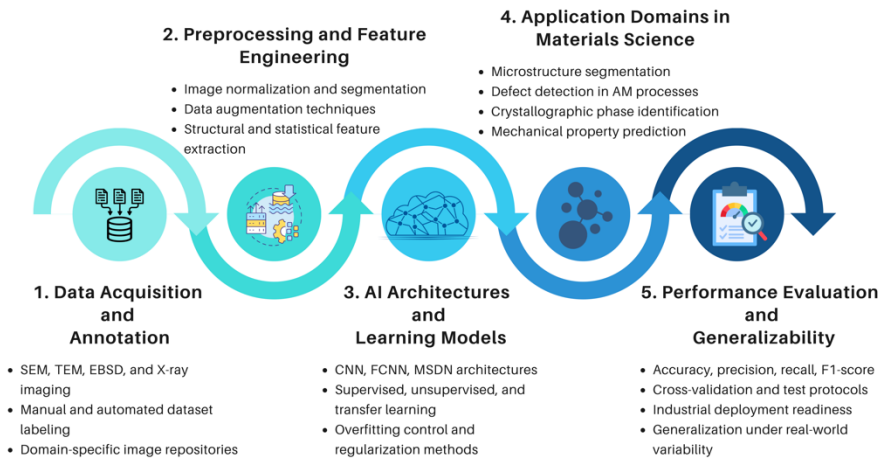


Figure 1. A structured workflow of AI-driven image analysis in materials science, illustrating the sequential stages from data acquisition to performance evaluation.

In the following sections, this chapter presents a structured exploration of artificial intelligence applications in image-based materials characterization. It begins with an overview of data acquisition modalities and preprocessing techniques, including image normalization, augmentation, and feature extraction pipelines tailored for microstructural data. The discussion then progresses to advanced learning architectures—particularly convolutional neural

networks (CNNs), fully connected networks, and multi-stream models—highlighting their effectiveness in tasks such as microstructure segmentation, defect localization, and crystallographic phase classification. Special attention is given to model training strategies, dataset annotation challenges, and evaluation metrics relevant to materials science contexts. The final sections examine property prediction frameworks that leverage both simulated and experimental imaging data, illustrating how AI models accelerate traditional workflows such as finite element analysis and fatigue life estimation. Taken together, these components provide a comprehensive framework that demonstrates the integration of AI-driven computer vision techniques into the broader domain of materials design and quality assessment.

1. Methodologies in Artificial Intelligence-Based Image Analysis

Image preprocessing is a critical step to improve the quality of raw images and reduce noise before applying AI algorithms. In this process, pixel intensities are set to a standard range through normalization to ensure consistency across datasets. Noise removal is performed using filters or deep learning-based methods to eliminate artifacts from imaging equipment. Additionally, segmentation techniques such as thresholding or clustering are applied to segment images into regions of interest, such as grains, phases, or defects (Stuckner et al. 2022).

AI-based image analysis in materials science effectively utilizes various ML and deep learning algorithms. Convolutional Neural Networks (CNN) are widely preferred for feature extraction and classification tasks such as defect detection in metal alloys or classification of crystal structures in TEM images. Generative Adversarial Networks (GAN) are used to generate synthetic images for data augmentation or to reconstruct missing data in low-

resolution images. Autoencoders play an important role in unsupervised learning tasks such as anomaly detection in composite materials. Additionally, transfer learning applied with pre-trained models such as ResNet or VGG reduces training time and data requirements by fine-tuning for materials science-specific applications (Davydzenka et al. 2022; Horwath et al. 2020).

The success of AI models depends on high-quality labeled datasets. In materials science, this involves labeling images with relevant features (e.g., cracks, voids, or grain boundaries). Crowd-sourced data collection, expert labeling, or semi-supervised learning can be used to create robust training datasets. Data augmentation techniques, such as rotation, translation, or scaling, are frequently applied to increase dataset diversity and prevent over-learning (Horwath et al. 2020)

To ensure reliability, AI models should be rigorously evaluated with metrics such as accuracy, precision, recall, and F1-score. Techniques such as K-fold cross-validation help evaluate the model's performance on unseen data. In materials science, domain-specific metrics such as grain size accuracy or defect detection rate are also considered (Stuckner et al. 2022)

2. Image Analysis based Applications in Materials Science

AI-based image analysis has found applications in several subfields of materials science.

2.1 Microstructure analysis

AI algorithms can segment and measure microstructural features such as grain size, phase distribution, and porosity. For example, deep learning models have predicted mechanical properties based on grain morphology by analyzing SEM images of steel alloys (Stuckner et al. 2022). Focusing on the automatic classification of

low carbon steel microstructures, a groundbreaking Deep Learning method is presented in the field of artificial intelligence and materials science. Microstructure is a complex internal structure that reflects the formation of the material and determines its physical-chemical properties; however, it has traditionally been classified subjectively by human experts. Using pixel-based segmentation and maximum voting scheme based on Fully Convolutional Neural Network (FCNN), this study succeeded in classifying microstructure components with 93.94% accuracy, greatly exceeding the 48.89% accuracy of the current best method. This innovative approach, which learns feature extraction and classification together, demonstrates the transformative potential of AI in material characterization by providing an objective, reliable and automatic solution for steel quality assessment (Azimi et al. 2018). A pioneering study at the intersection of artificial intelligence and materials science provides an innovative solution to microstructure analysis traditionally assessed by manual and subjective methods, using a deep convolutional neural network model for the automatic segmentation of complex microstructures. This research, performed on an open-access dataset on ultra-high carbon steel, addresses two key segmentation tasks: the separation of cementite particles in the spheroidized matrix and the segmentation of large fields of view containing multiple components such as grain boundary carbide, spheroidized particle matrix, particle-free impoverished regions and Widmanstätten cementite. By combining these data-driven models, critical metrics such as cementite particle size and impoverished zone width distributions were obtained from complex micrographs. This work, whose fully annotated dataset is available at materialsdata.nist.gov, demonstrates the potential of artificial intelligence to revolutionize materials characterization (DeCost et al. 2019). Another remarkable study that demonstrates the transformative potential of AI in microstructural analysis focuses on the automatic classification of microstructures of low-carbon steel.

Microstructure is a complex internal structure that reflects the formation of the material and determines its physical-chemical properties; however, it is usually classified subjectively by human experts. Using pixel-based segmentation and maximum voting scheme with FCNN, this study succeeded in classifying microstructure components with 93.94% accuracy. This rate greatly exceeds the 48.89% accuracy of the current best method, providing an objective and reliable approach to steel quality assessment (Azimi et al. 2018).

2.2 Defect Detection

Automatic defect detection is critical to quality control for materials used in the aerospace, automotive, and electronics industries. Deep learning models can detect cracks, voids, or inclusions with high accuracy, reducing the need for manual inspection.

Process monitoring in additive manufacturing (AM) is a critical element to accelerate industrialization; however, traditional methods such as computed tomography (CT) can only be applied post-build and eliminate the opportunity for in-process defect correction. In the present study, powder bed fusion (PBF) AM offers an in-situ defect detection strategy, enabling in-process defect detection and correction through layer-by-layer visual inspection. Multidimensional visual features were extracted from images collected from each build layer with a high-resolution DSLR camera, and binary classification was performed using linear support vector machine (SVM). Regions classified as defects or nominal structures were trained with ground truth labels obtained from post-build 3D CT scans. Disturbances in CT data (e.g., incomplete fusion, porosity, cracks) were identified by automatic analysis or manual inspection and transferred to the image domain by affine transformation. Over 80% in-situ defect detection accuracy was achieved in cross-

validation experiments. This innovative approach transforms part qualification in AM processes with AI-based image analysis, providing real-time quality control during production (Gobert et al. 2018). Real-time detection and classification of anomalies is critical to increase industrial adoption of powder bed metal AM. Defects such as recoating knife bumps, binder deposition issues, spatter and porosity can appear on the surface at every layer of the build process. In this context, another innovative work proposes a novel Convolutional Neural Network architecture for pixel-based semantic segmentation of layer-wise powder bed imaging data. This algorithm has the advantages of presenting segmentation results at the native resolution of the sensor, transferring the learned information to different AM machines and providing real-time performance. Tested on six different machines covering three technologies such as laser fusion, coherent sputtering and electron beam fusion, this method outperforms previous algorithms in terms of localization, accuracy, computation time and generalizability. This study proves that AI-based image analysis can transform defect detection in AM processes, adding reliability and efficiency to industrial production (Scime et al. 2020).

2.3. Phase Identification

In multiphase materials, AI can distinguish between different phases (for example, austenite and martensite in steel) based on image contrast or texture. This ability is particularly valuable for studying phase transformations during heat treatment or deformation.

Phase identification is a critical process for the characterization of crystal structures in materials science, and automatic and accurate determination of crystal symmetry is of great importance in this process. In recent years, artificial intelligence-based image processing techniques, especially DL methods, have

emerged as an effective tool in revealing the relationships between crystal phases and patterns obtained from X-ray or electron beam diffraction images. In the study, it has been shown that shaping the diffraction images with preprocessing techniques and a model developed using the multi-stream DenseNet (MSDN) architecture significantly increases the phase identification accuracy. This is due to the shaping strategy applied to the diffraction images. This strategy effectively distinguishes subtle pattern differences between symmetrically close phases (e.g., monoclinic and orthorhombic or trigonal and hexagonal systems). The proposed image processing and DL-based protocols provide high accuracy in multi-class phase identification problems, thus strengthening the practical use of artificial intelligence-assisted phase analysis in material characterization (Tiong et al. 2020). Although the use of ML techniques in the analysis of transmission electron microscopy (TEM) data is still limited, significant progress has been made in this area. Another study developed a convolutional neural network (CNN)-based model to reliably classify crystal phases from a small number of electron images and non-oriented diffraction patterns. The model was cross-validated with high-resolution TEM images and diffraction patterns in a variety of systems, from alloys to two-dimensional materials. This study demonstrates that AI-assisted image processing techniques are a powerful tool in TEM-based phase identification processes, providing an innovative analysis method for material characterization (Aguiar et al. 2019).

2.4. Estimation of Material Properties

By correlating image features with experimental data, AI models can predict material properties such as hardness, tensile strength, or thermal conductivity. This approach is particularly useful in high-throughput screening of new materials.

The fatigue properties of additive manufacturing (AM) materials depend on a multitude of factors such as processing parameters, microstructure, residual stress, surface roughness, and porosity, and the combination of these factors often results in low efficiency and high cost. In this context, another pioneering study examines the state-of-the-art advances in predicting the fatigue properties of AM materials using ML techniques. The study outlines the use of ML models such as Feedforward Neural Network (FNN), Convolutional Neural Network (CNN), Adaptive Network-Based Fuzzy Inference System (ANFIS), Support Vector Machine (SVM), and Random Forest (RF) in fatigue life and crack growth rate prediction by considering the dependencies on AM processes such as laser power, scanning speed, layer height, build direction, and post-processing parameters. Adapted for the specific properties of AM materials, these models offer effective results despite the challenges such as small datasets and a wide range of features. The study shows that AI-based image analysis and ML techniques offer innovative solutions in materials science and manufacturing processes by predicting the fatigue properties of AM materials (YI et al. 2024). In another study, a CNN-based solution to the computational challenges encountered in simulating random spatial variation in mechanical properties of composite materials was presented. In the traditional method, separate numerical homogenization is required for each Stochastic Volume Element (SVE) extracted from the composite microstructure image by moving window technique, and this process can take hours. The researchers developed a revolutionary approach by replacing this expensive and iterative homogenization procedure with a Convolutional Neural Network (CNN). The proposed CNN model takes SVE images as input and directly estimates the apparent mechanical properties of that region and is trained on randomly generated SVEs with variable volume fractions and inclusion locations. The results show that this methodology can estimate

random feature fields derived from both computer-simulated and real microstructure images with high accuracy within a few seconds, providing approximately 1000-10000 times speedup compared to the traditional finite element-based approach. This work represents a significant paradigm shift in terms of computational efficiency in materials science by offering real-time analysis in composite material design and optimization (Gavallas et al. 2024).

Conclusions

In this chapter, we have surveyed state-of-the-art AI-driven image analysis techniques and their applications across materials science domains. Beginning with preprocessing and feature-extraction methods, we explored supervised and unsupervised learning models—such as CNNs, fully connected networks, and Multi-Stream DenseNet (MSDN)—and demonstrated how these architectures significantly boost both accuracy and throughput in materials characterization tasks. To synthesize the discussion, the key application areas can be organized according to their specific intersections with AI methodologies and learning paradigms as outlined below.

Deep learning–based microstructure segmentation in steel alloys achieved 93.94% accuracy, far surpassing the 48.9% benchmark set by human experts. This represents a critical step toward automated, standardized microstructural evaluation. In powder-bed fusion additive manufacturing, in-situ imaging coupled with AI models yielded over acceptable detection accuracy values. This capability paves the way for real-time quality control, reducing both production costs and lead times. MSDN-based approaches effectively distinguished between closely related crystallographic phases—such as monoclinic versus orthorhombic systems or trigonal versus hexagonal structures—with high reliability. TEM diffraction image analysis further validated these findings. CNN

models applied to composite materials produced results up to 10,000× faster than traditional finite-element simulations. Likewise, ML-based fatigue-life predictions for additively manufactured components enable high-volume screening workflows.

Despite these advances, AI applications in this field have still limitations. The availability of labeled datasets remains restricted, and integrating diverse microscopy modalities poses ongoing challenges. Moreover, assessing model generalizability under varied operational conditions requires further investigation. Despite the promising outcomes across diverse application domains, current AI models still exhibit notable limitations—particularly in terms of generalizability, interpretability, and cross-domain adaptability. These challenges define clear and essential directions for future research and development. Key areas for improvement can be summarized as follows:

- Integration of multi-modal imaging data (e.g., SEM, EDS) to enable richer and more comprehensive feature representations.
- Customization of pre-trained neural networks to facilitate rapid adaptation to small and domain-specific datasets.
- Deployment of AI-powered prototype systems in real-world manufacturing settings for validation and performance benchmarking.
- Implementation of explainable AI (XAI) methods to improve transparency and interpretability of model decisions.

AI-enabled image analysis is ushering in a new paradigm in materials science—one that is more objective, reproducible, and

scalable. As these approaches gain broader adoption in both academic research and industrial applications, we anticipate transformative impacts on material discovery, optimization, and quality assurance over the coming years.

References

I. Goodfellow;, Y. Bengio;, and A. Courville; 2016. “Deep Learning.” 1–23.

Aguiar, J. A., M. L. Gong, R. R. Unocic, T. Tasdizen, and B. D. Miller. 2019. “Decoding Crystallography from High-Resolution Electron Imaging and Diffraction Datasets with Deep Learning.” *Science Advances* 5(10).

Azimi, Seyed Majid, Dominik Britz, Michael Engstler, Mario Fritz, and Frank Mücklich. 2018. “Advanced Steel Microstructural Classification by Deep Learning Methods.” *Scientific Reports* 8(1):1–14.

Davydzenka, Tsimur, Daniel Sinclair, Nikhilesh Chawla, and Pejman Tahmasebi. 2022. “Deep-Layers-Assisted Machine Learning for Accurate Image Segmentation of Complex Materials.” *Materials Characterization* 192:112175. doi:10.1016/J.MATCHAR.2022.112175.

DeCost, Brian L., Bo Lei, Toby Francis, and Elizabeth A. Holm. 2019. “High Throughput Quantitative Metallography for Complex Microstructures Using Deep Learning: A Case Study in Ultrahigh Carbon Steel.” *Microscopy and Microanalysis* 25(1):21–29. doi:10.1017/S1431927618015635.

Gavallas, Panagiotis, George Stefanou, Dimitrios Savvas, Cécile Mattrand, and Jean Marc Bourinet. 2024. “CNN-Based Prediction of Microstructure-Derived Random Property Fields of Composite Materials.” *Computer Methods in Applied Mechanics and Engineering* 430:117207. doi:10.1016/J.CMA.2024.117207.

Gobert, Christian, Edward W. Reutzler, Jan Petrich, Abdalla R. Nassar, and Shashi Phoha. 2018. “Application of Supervised

Machine Learning for Defect Detection during Metallic Powder Bed Fusion Additive Manufacturing Using High Resolution Imaging.” *Additive Manufacturing* 21:517–28. doi:10.1016/J.ADDMA.2018.04.005.

Horwath, James P., Dmitri N. Zakharov, Rémi Mégret, and Eric A. Stach. 2020. “Understanding Important Features of Deep Learning Models for Segmentation of High-Resolution Transmission Electron Microscopy Images.” *Npj Computational Materials* 6(1):1–9. doi:10.1038/S41524-020-00363.

Scime, Luke, Derek Siddel, Seth Baird, and Vincent Paquit. 2020. “Layer-Wise Anomaly Detection and Classification for Powder Bed Additive Manufacturing Processes: A Machine-Agnostic Algorithm for Real-Time Pixel-Wise Semantic Segmentation.” *Additive Manufacturing* 36:101453. doi:10.1016/J.ADDMA.2020.101453.

Stuckner, Joshua, Bryan Harder, and Timothy M. Smith. 2022. “Microstructure Segmentation with Deep Learning Encoders Pre-Trained on a Large Microscopy Dataset.” *Npj Computational Materials* 8(1):1–12. doi:10.1038/S41524-022-00878-5;SUBJMETA.

Tiong, Leslie Ching Ow, Jeongrae Kim, Sang Soo Han, and Donghun Kim. 2020. “Identification of Crystal Symmetry from Noisy Diffraction Patterns by a Shape Analysis and Deep Learning.” *Npj Computational Materials* 6(1):1–11. doi:10.1038/S41524-020-00466-5.

YI, Min, Ming XUE, Peihong CONG, Yang SONG, Haiyang ZHANG, Lingfeng WANG, Liucheng ZHOU, Yinghong LI, and Wanlin GUO. 2024. “Machine Learning for Predicting Fatigue Properties of Additively Manufactured Materials.”

Chinese Journal of Aeronautics 37(4):1–22.
doi:10.1016/J.CJA.2023.11.001.

CHAPTER 7

HAZELNUT SHELL FLOUR FILLED EPOXY COMPOSITES: CHARACTERIZATION AND MECHANICAL PROPERTIES

MURAT EROĞLU¹

Introduction

Sustainable and eco-friendly material demand stimulates extensive research in developing com-posite materials filled with natural fillers, particularly those derived from agricultural waste. In these fillers, hazelnut shells are considered abundant, cheap, and possessing unique fibrous structures. The hazelnut industry mainly concentrated in Turkey generates lots of hazelnut shells that can be recycled into a renewable and cheap substitute for synthetic reinforcements. The use of hazelnut shells deals with waste management problems and enhances the mechanical and thermal properties of polymer composites to make them viable in many industrial applications (Rangappa et al., 2018).

Epoxy resins are ideal candidates for many industries due to their good mechanical properties, chemical resistance, and adhesive strength. Their inherent brittleness, however, restricts their

¹ Instructor Dr., Bursa Technical University, Central Research Laboratory, Orcid: 0000-0001-5340-9609

application in areas needing quite a bit of toughness and flexibility. Instead, with such fillers, synthetic-natural fillers have been researched for incorporation with epoxy matrices. These are the more natural fillers with respect-wood flour, coconut fibers, and rice husks regarding their biodegradability and low density, which improve the mechanical properties of composites (Ferreira et al., 2019; Gouda et al., 2020). Among these, hazelnut shell flour is a particularly suitable reinforcing filler because of its high cellulose content and fibrous structures that certainly will increase the mechanical performance of epoxy composites (Derradji et al., 2022; Sosiati et al., 2023).

Natural fillers can be relatively easy to work with. Water absorption and interfacial adhesion between filler and epoxy matrix, however, can provide challenges. Such natural fillers absorb water since they are more hydrophilic than synthetic fillers, which causes moisture pick-up in the composite material and possible loss of mechanical performance and durability (Behera et al., 2023; Sosiati et al., 2022). One of the unquestionable requirements in obtaining satisfactory performance from mechanical tests is compatibility of the hydrophobic epoxy matrix with the hydrophilic natural filler. This situation leads to the development of stress concentrations as a result of poor interfacial adhesion to premature composite failure under mechanical loading (Kudus et al., 2019; Raj et al., 2022). Water absorption is greatly affected by the extent of dispersion of fillers in conjunction with filler types, as supported by multiple findings. A filler well dispersed is presumed to reduce surface voids thereby increasing low water absorption (Choudhary et al., 2019; Sosiati et al., 2023).

Here in is the work that studies the influence of addition of hazelnut shell flour fillers into epoxy resin composites, emphasizing the consequent effect of the amount of filler on the properties, water absorption occurrence, and surface characteristics of the composites.

Incorporating various amounts of hazelnut shell flour-including 5, 10, 20, 30, and 35 % as the varying optimal concentration of filler that yields balanced mechanical performance and water resistance. Characterization means for the composites are particle size analysis, water absorption tests, contact angle measurements, SEM, and mechanical testing. Findings are important from this study to propose hazelnut shell flour as an environmentally sustainable filler for these types of composites, eventually leading toward building green materials for application in industries.

Experimental Details

Materials

The Central Research Laboratory (BTÜ) in the Giresun, Turkey, area is responsible for collecting the hazelnut shells. We purchased epoxy resin and its hardener from Admiral-Turkey.

Preparation of hazelnut shell flour filled epoxy based composites

To make hazelnut shell flour, hazelnut shells were ground in a titanium knife and a 0.2 µm filter using a Pulverisette 14 Fritsch™ Germany for five minutes. Using a glass rod, hazelnut shell flour was manually mixed with epoxy resin in varying proportions. Hardener was added to the mixture after it had been mixed, and it was then mixed once more by hand. After pouring these concoctions into the silicone mold, they were allowed to sit at room temperature for a full day. Table 1 listed the amount of hazelnut shell flour in the resin and sample code.

Table 1. Compositions and sample codes of hazelnut shell flour filled epoxy based composites.

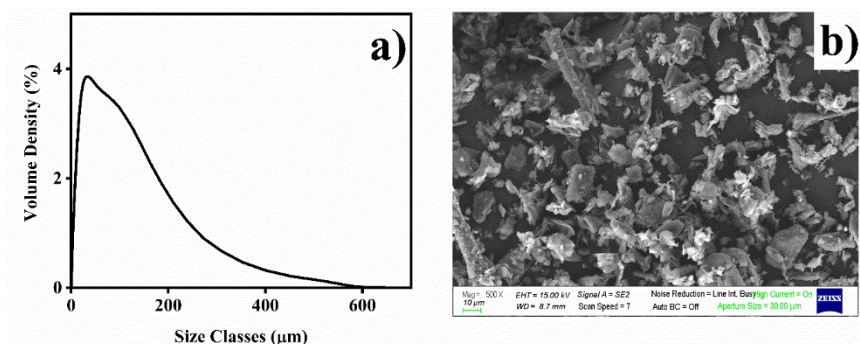
Sample Content	Sample Code
Epoxy	E
Epoxy – 5% hazelnut shell flour	E – 5H
Epoxy – 10% hazelnut shell flour	E – 10H
Epoxy – 20% hazelnut shell flour	E – 20H
Epoxy – 30% hazelnut shell flour	E – 30H
Epoxy – 35% hazelnut shell flour	E – 35H

Characterizations of the samples

Particle size measurements

Particle size measurement and SEM image of hazelnut shell flours can be seen in Figure 1. Using the particle size distribution 10% (D10) of the particles are smaller than 5.65 μm , 50% (D50) are smaller than 36.5 μm , and 90% (D90) are smaller than 161 μm . This characteristic produces a comparatively tiny particle size, which could help it be adopted in applications that need large surface areas. The morphology of the ground hazelnut shell particles is extensively revealed through the SEM image (Mag. 500X). The presence of the fibrous and randomly shaped particles is considerably revealed in the image. It indicates that the native fibrous architecture of hazelnut shell has mainly remained unscathed even after such grinding process. There is variation between the observed particles in terms of sizes and distribution for the particle size. This finding is consistent with the particle size distribution E graph and shows that grinding does not produce a uniform particle size distribution. Further, on analysing surface structure of the particles, some particles were noted to possess a rough and fibrous surface. This rough texture indicates that the hazelnut shell fibers are broken down due to grinding and increased surface area.

Figure 1. Particle size measurement (a) and SEM image (b) of hazelnut shell flours.



Water absorption test

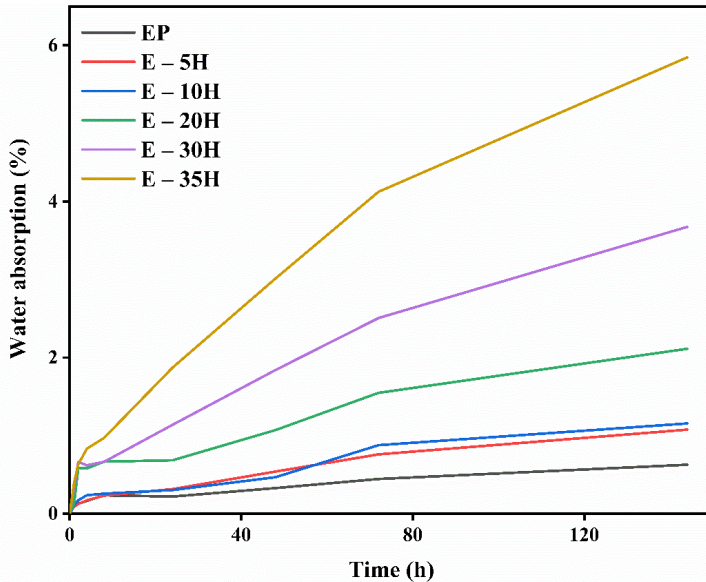
It also finally discloses how the specimens from epoxy-based composites containing various amounts of hazelnut shell flour behave water wise when used in real-life applications. It has been observed that all the samples absorb water with time, initially showing a steep rate in the first 24 hours, which gradually reduced thereafter. For example, pure epoxy (E) shows no water absorption at 0 hours, a water absorption percentage of 0.22 at the end of 24 hours, and a water absorption percentage of 0.63 at 144 hours. The time dependency of water absorption is likewise similar to the findings of literature based on other composite materials (Zamani et al., 2022). The addition of hazelnut shell flour significantly affects the water absorption properties of the composites. The absorption of water increases as the percentage of hazelnut shell flour increases. For example, E-5H absorbs water with a rate of 1.08 % after 144 hours, while an E-35H absorbs 5.85 %. The increase in water absorption with an increase in the filler content indicates that hazelnut shell flour conferred hydrophilic properties to the epoxy matrix that, in turn, increased moisture affinity in the composite. This has been confirmed in other studies where natural fibers and fillers were shown to enhance moisture absorption because of their

inherent hydrophilicity (Zamani et al., 2022). The moisture is thought to be absorbed due to higher porosity, which comes along with the incorporation of hazelnut shell flour, explaining that natural fillers may weaken the bond between the matrix and the filler and, hence, enhance water absorption (Włodarczyk-Fligier & Polok-Rubiniec, 2021). Furthermore, the distinct rates of water absorption shown by the samples usually reflect how water-sensitive the material is according to the amount of natural fibers it contains. Thus, it could be inferred that the E-35H samples with its higher percentage of hazelnut shell flour is very high when it comes to water absorption in comparison with others. Such thing reminds one to include environmental conditions where such composites would be used, as it would mean an increase of moisture absorption that could compromise the strength of the mechanical properties of the material, such has been pronounced by Pradhan and Satapathy, who noted that moisture might lead to microcracks and reduced impact-strength in composites (Pradhan & Satapathy, 2022).

Table 2. Water absorption test results of the epoxy based composites.

Time (h)	EP(%)	E-5H(%)	E-10H(%)	E-20H(%)	E-30H(%)	E-35H(%)
0	0.00	0.00	0.00	0.00	0.00	0.00
1	0.13	0.09	0.11	0.12	0.33	0.39
2	0.13	0.12	0.17	0.59	0.66	0.63
4	0.16	0.17	0.24	0.58	0.62	0.83
8	0.23	0.23	0.26	0.67	0.66	0.97
24	0.22	0.32	0.30	0.69	1.14	1.87
48	0.33	0.54	0.47	1.07	1.84	3.01
72	0.44	0.76	0.88	1.55	2.51	4.13
144	0.63	1.08	1.16	2.11	3.67	5.85
0	0.00	0.00	0.00	0.00	0.00	0.00

Figure 2. The water absorptions of the epoxy based composites.

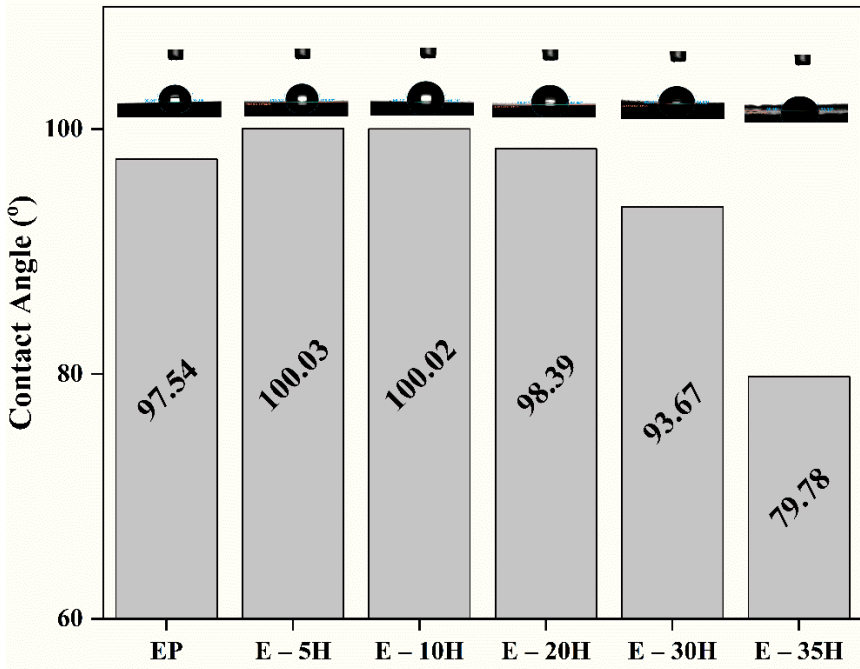


Contact angle measurement

Figure 3 shows the contact angle test results of the epoxy based composites. Water-contact-angle measurements on epoxy composites with variable amounts of hazelnut shell flour furnish some insights into the filler concentration-hydrophobicity relationship. For unmodified epoxy (EP), the water-contact angle was 97.54° . The incorporation of 5% (E-5H) and 10% (E-10H) hazelnut shell flour increased hydrophobicity with contact angles of 100.03° and 100.02° , respectively. However, higher concentrations, namely 20% (E-20H), 30% (E-30H), and 35% (E-35H), exhibited a pronounced opposite effect with reduced hydrophobicity: contact angles of 98.39° , 93.67° , and 79.78° , respectively. This observation implies that lower amounts of hazelnut shell flour might augment the hydrophobic properties of the epoxy surface, whereas higher amounts would be more deleterious. This would go along with the literature concerning the topic of filler concentration affecting the hydrophobicity of polymer composites. The addition of lignin as

filler in polylactic acid composites tended to make polymer composites more hydrophobic, which is similar to what has been found in this study with hazelnut shell flour. This suggests a possible common mechanism where lower concentrations of hydrophilic fillers enhance the complete hydrophobicity of a polymer matrix. Therefore, at higher concentrations, this hydrophobicity could be weakened by the effect of aggregation of filler particles on the surface characteristics of the composite (Gao et al., 2019). A similar discussion on the contribution of surface roughness and chemical composition to the hydrophobicity of a material appears in the literature. A study emphasized the critical roles of the chemical and topographical features in moisture absorption behavior for the carbon fiber/epoxy composites (Qian et al., 2016). They observed that by altering the surface characteristics, interfacial adhesion could be improved; and this is linked to the epoxy composite findings concerning contact angles. Filler-induced roughness may induce some composite-level wetting behavior necessary for superhydrophobicity (Bhushan & Nosonovsky, 2010). In addition, increased values of modulus are usually observed with higher filler loading correlating to changes in surface properties (Shah & Stansbury, 2014). Considering the mechanical properties of the epoxy composites along with the hydrophobic characters is evidently classified. It is the interplay of filler concentration and mechanical reinforcement that governs the overall performance of the composites.

Figure 3. The contact angles of the epoxy based composites.



Scanning electron microscopy (SEM)

Remarkable and sole feature in Figure 4 is display SEM images showing critical insights on fractures behavior and distributed additives within epoxy-based composites under tensile testing. Uniquely, the EP (pure epoxy) specimen indicates a smooth and rough fractured surface, suggesting brittle fracture behavior. This observation corresponds with the finding of Debnath and Abdullah, who noted that similar smooth fracture surfaces characterized incompletely reinforced composites turning toward brittle failure modes (Debnath & Abdullah, 2017). The visible lines and cracks in EP samples indicate energy absorption during deformation absence-a common characteristic of brittle materials.

On the other hand, the E-5H sample having a hazelnut shell content of 5% has a rough fracture surface. However, this roughness

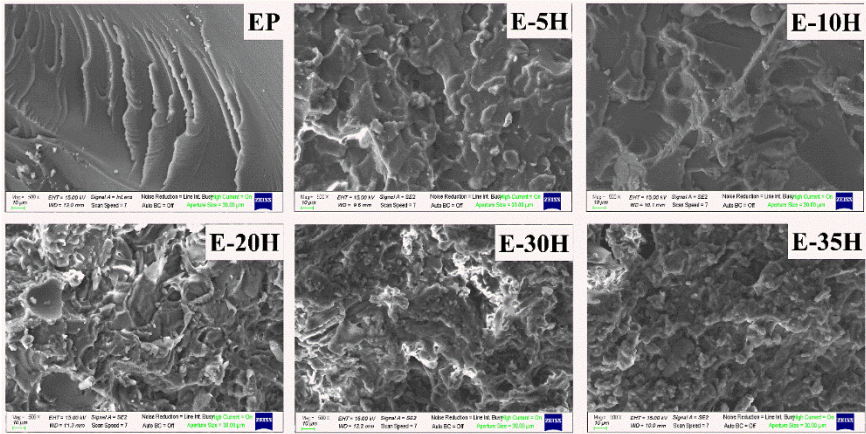
may refer to a more uniform distribution of hazelnut shell within the epoxy matrix probably impeding crack propagation and leading to the assumption of composite toughness improvement. Aliotta et al. supported this mechanism by showing that improved mechanical properties of biocomposites, due to better stress distribution and energy absorption i.e. that it is worthacknowledging that the strengthening of composites will be associated with the cracking of polymeric material and pore formation (Aliotta et al., 2021). The same holds for the E-10H sample, with a rough fracture surface but some onset of agglomeration, which would suggest that while distribution is still reasonable, the early onset of filler clustering can start to negatively affect performance (Aliotta et al., 2021).

At around twenty percent and above concentrations of hazelnut shell in the E-20H and E-30H samples, they turn from the breakage surfaces into rough and jagged. Such a trend correlates with that of Gbadeyan et al.; they noted that, the higher the filler content, the poorer the adhesion between the matrix and the filler used, leading to concentration of stress and initiation points of cracks (Gbadeyan et al., 2021). E-20H sample agglomeration is more spread out and may worsen the mechanical integrity of the composite, thus confirming the observations of Oladele et al. that excess filler loading negatively influences composite performance (Oladele et al., 2024).

The E-35H sample with 35% maximum hazelnut shell content shows signs of massive agglomeration, exhibiting clear separation between the epoxy matrix and the additive material. The critical balance required in filler loading indicated that excessive amounts would lead to poor interfacial adhesion: Poor dispersion and adhesion will adversely affect the mechanical properties of composites (Oladele et al., 2024). Findings indicate that low hazelnut shell concentration up to an optimal dose increases toughness via good dispersal, while high concentrations lead to

agglomerations and a drop in mechanical performance, as supported by the conclusion drawn by Aliotta et al. on the inverse relationship between filler contents and the mechanical properties of biocomposites (Aliotta et al., 2021).

Figure 4. SEM photographs of the cross-sections of epoxy based composites after tensile testing.



Mechanical test

The mechanical properties associated with different percentages of hazelnut shell flour incorporated in epoxy composites are given in Table 3 and Figure 5 above. The mechanical properties of the epoxy composite with different percentages of hazelnut shell flour indicate that the incorporation of natural fillers into polymer matrices leads to considerable trends comparable to the finding from literature. Pure epoxy sample exhibited the strength of 51.2 MPa and tends to lower or decline with hazelnut shell flour incorporation, for the examples E-5H and E-35H, where tensile strengths drop to 35.1 and 21.7 MPa, respectively. The reduction in tensile strength follows the observations made by Sałasińska et al., who remarked that the incorporation of plant waste fillers usually modifies the mechanical properties of epoxy composites towards higher filler contents resulting in reduced flexibility and increased brittleness. In the same

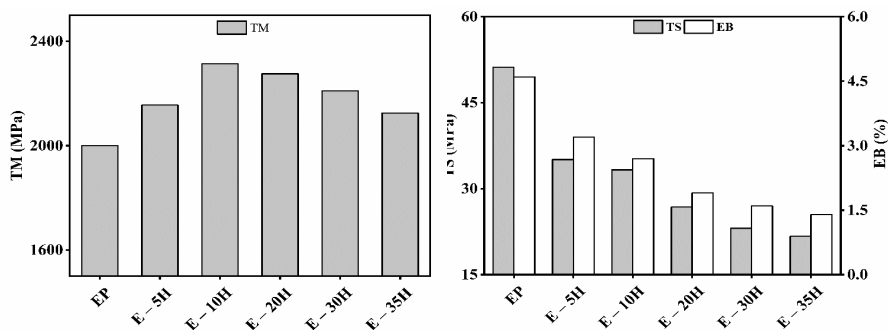
regard, Włodarczyk-Fligier and Polok-Rubinić reported that due to increased filler content, the porosity of composites considerably rises and results in poor interfacial bonding between the filler and matrix, which can lead to ultimate defects in tensile strength (Włodarczyk-Fligier & Polok-Rubinić, 2021). The elongation at the break also measures a downward trend from 4.6% in pure epoxy to 3.2% and 1.4% in the E-5H and E-35H samples, respectively.

This is in agreement with Ghaleb et al. since according to them, the fillers aggregate resulting to the deterioration of tensile properties such as elongation at break owing to the limited flexibilities of composite material (Ghaleb et al., 2014). In addition, tensile modulus increases from 2000 MPa in pure epoxy to 2156 MPa in the E-5H sample, decreasing to 2125 MPa in the E-35H sample. Such behavior suggests that low percentages of hazelnut shell flour can still enhance stiffness; beyond that concentration, improvement is limited, hence, corroborating the findings of Demirer et al., who documented that excessive filler content negatively affects the mechanical performance of composites (Demirer et al., 2018). The general trend that has been established from the analysis of the mechanical properties of epoxy composites with hazelnut shell flour shows that the effect of filler content on the performance of the materials has complex interactions. Such reduction in tensile strength and elongation at break causes hazelnut shell flour to improve some properties, rendering those composites unsuitable for use in applications requiring high flexibility and strength. This was also supported by Ceraulo et al. who advocated expert evaluation of filler content to satisfy the intended mechanical property requirements for the specific application (Ceraulo et al., 2022).

Table 3. Tensile test results of the epoxy based composites.

Sample Code	Tensile strength (MPa)	Tensile modulus (MPa)	Elongation at break (%)
EP	51.2	2000	4.6
E – 5H	35.1	2156	3.2
E – 10H	33.3	2314	2.7
E – 20H	26.8	2276	1.9
E – 30H	23.1	2210	1.6
E – 35H	21.7	2125	1.4

Figure 5. Tensile test results of the epoxy based composites.



Conclusion

The incorporation of hazelnut shell flour into epoxy composites has been shown to significantly affect their mechanical, water absorption, and surface properties. Lower concentrations of hazelnut shell flour (up to 10%) enhance the hydrophobicity and stiffness of the composites, while higher concentrations lead to increased water absorption and reduced tensile strength. SEM analysis revealed that higher filler content results in poor interfacial adhesion and agglomeration, which negatively impacts the mechanical performance. These findings suggest that hazelnut shell flour can be a viable filler for epoxy composites, but the filler content must be optimized to achieve the desired balance between

mechanical properties and water resistance. Future studies should focus on optimizing the filler content and exploring surface treatments to improve the interfacial adhesion between the epoxy matrix and hazelnut shell flour, thereby enhancing the overall performance of the composites.

References

Aliotta, L., Vannozzi, A., Bonacchi, D., Coltelli, M., & Lazzeri, A. (2021). Analysis, Development, and Scaling-Up of Poly(lactic Acid) (PLA) Biocomposites With Hazelnuts Shell Powder (HSP). *Polymers*, *13*(23), 4080. <https://doi.org/10.3390/polym13234080>

Behera, S., Gautam, R. K., Mohan, S., & Tiwari, A. (2023). Mechanical, Water Absorption and Tribological Properties of Epoxy Composites Filled With Waste Eggshell and Fish Scale Particles. *Progress in Rubber Plastics and Recycling Technology*, *39*(4), 387–403. <https://doi.org/10.1177/14777606231175921>

Bhushan, B., & Nosonovsky, M. (2010). The Rose Petal Effect and the Modes of Superhydrophobicity. *Philosophical Transactions of the Royal Society a Mathematical Physical and Engineering Sciences*, *368*(1929), 4713–4728. <https://doi.org/10.1098/rsta.2010.0203>

Ceraulo, M., Mantia, F. P. L., Mistretta, M. C., & Titone, V. (2022). The Use of Waste Hazelnut Shells as a Reinforcement in the Development of Green Biocomposites. *Polymers*, *14*(11), 2151. <https://doi.org/10.3390/polym14112151>

Choudhary, M., Singh, T., Dwivedi, M., & Patnaik, A. (2019). Waste Marble Dust-filled Glass Fiber-reinforced Polymer Composite Part I: Physical, Thermomechanical, and Erosive Wear Properties. *Polymer Composites*, *40*(10), 4113–4124. <https://doi.org/10.1002/pc.25272>

Debnath, S., & Abdullah, A. H. (2017). Mechanical Performance of Cockle Shell Particles (CSP) and Oil Palm Fibre (OPF) Reinforced Epoxy Composite. *International Journal of Engineering Materials and Manufacture*, *2*(3), 58–66. <https://doi.org/10.26776/ijemm.02.03.2017.03>

Demirer, H., Kartal, İ., Yildirim, A., & Büyükkaya, K. (2018). The Utilisability of Ground Hazelnut Shell as Filler in Polypropylene Composites. *Acta Physica Polonica A*, 134(1), 254–256. <https://doi.org/10.12693/aphyspola.134.254>

Derradji, M., Liu, W., & Fantuzzi, N. (2022). Editorial: Advanced Green Thermosetting Composites: Design and Performances. *Frontiers in Materials*, 9. <https://doi.org/10.3389/fmats.2022.1037259>

Ferreira, F. V., Pinheiro, I. F., Souza, S. F. de, Mei, L. H. I., & Lona, L. M. F. (2019). Polymer Composites Reinforced With Natural Fibers and Nanocellulose in the Automotive Industry: A Short Review. *Journal of Composites Science*, 3(2), 51. <https://doi.org/10.3390/jcs3020051>

Gao, Y., Qu, W., Liu, Y., Hu, H., Cochran, E. W., & Bai, X. (2019). Agricultural Residue-derived Lignin as the Filler of Polylactic Acid Composites and the Effect of Lignin Purity on the Composite Performance. *Journal of Applied Polymer Science*, 136(35). <https://doi.org/10.1002/app.47915>

Gbadeyan, O. J., Adali, S., Bright, G., & Sitholé, B. (2021). The Investigation of Reinforcement Properties of Nano-CaCO₃ Synthesized From *Achatina Fulica* Snail Shell Through Mechanochemical Methods on Epoxy Nanocomposites. *Nanocomposites*, 7(1), 79–86. <https://doi.org/10.1080/20550324.2021.1936972>

Ghaleb, Z. A. A., Mariatti, M., Ariff, Z. M., & Mohamed, A. R. (2014). Comparison on Tensile Properties of Graphene and Multi-Walled Carbon Nanotubes/Epoxy Thin Film Composites. *Advanced Materials Research*, 1024, 140–143. <https://doi.org/10.4028/www.scientific.net/amr.1024.140>

Gouda, K., Bhowmik, S., & Das, B. (2020). Thermomechanical Behavior of Graphene Nanoplatelets and Bamboo Micro Filler Incorporated Epoxy Hybrid Composites. *Materials Research Express*, 7(1), 015328. <https://doi.org/10.1088/2053-1591/ab67f8>

Kudus, M. H. A., Akil, H. M., Zakaria, M. R., & Othman, M. B. H. (2019). Effect of Water Absorption on Dielectric Constant of TMD Cured of Carbonaceous Filled Epoxy Composites. *Journal of Physical Science*, 30(Supp.1), 101–107. <https://doi.org/10.21315/jps2019.30.s1.6>

Oladele, I. O., Taiwo, A. S., Bello, L. J., Balogun, S. O., Siphon, L. S., & Adelani, S. O. (2024). Fabrication of Animal Shell and Sugarcane Bagasse Particulate Hybrid Reinforced Epoxy Composites for Structural Applications. *Polymers and Polymer Composites*, 32. <https://doi.org/10.1177/09673911231202183>

Pradhan, P., & Satapathy, A. (2022). Physico-Mechanical Characterization and Thermal Property Evaluation of Polyester Composites Filled With Walnut Shell Powder. *Polymers and Polymer Composites*, 30. <https://doi.org/10.1177/09673911221077808>

Qian, X., Zhang, Y., Wang, X., Heng, Y. J., & Zhi, J. (2016). Effect of Carbon Fiber Surface Functionality on the Moisture Absorption Behavior of Carbon Fiber/Epoxy Resin Composites. *Surface and Interface Analysis*, 48(12), 1271–1277. <https://doi.org/10.1002/sia.6031>

Raj, R. R., Sathish, S., Mansadevi, T. L. D., Supriya, R., Sekar, S., Patil, P. P., & Tonmoy, M. M. (2022). Effect of Graphene Fillers on the Water Absorption and Mechanical Properties of NaOH-Treated Kenaf Fiber-Reinforced Epoxy Composites. *Journal of Nanomaterials*, 2022(1). <https://doi.org/10.1155/2022/1748121>

Rangappa, S. M., Puttegowda, M., Jawaid, M., SenthamaraiKannan, P., Senthil, S., & Pradeep, S. (2018). Characterization and Properties of Natural Fiber Polymer Composites: A Comprehensive Review. *Journal of Cleaner Production*, 172, 566–581. <https://doi.org/10.1016/j.jclepro.2017.10.101>

Shah, P. K., & Stansbury, J. W. (2014). Role of Filler and Functional Group Conversion in the Evolution of Properties in Polymeric Dental Restoratives. *Dental Materials*, 30(5), 586–593. <https://doi.org/10.1016/j.dental.2014.02.015>

Sosiati, H., Ma'arif, M. G., Firmansyah, W. A., & Hamdan, S. (2023). Characterization of the Properties of Bio-CaCO₃ Waste Eggshell and Abaca Fiber Reinforced Hybrid Composites. *Materials Science Forum*, 1087, 13–20. <https://doi.org/10.4028/p-n61z06>

Sosiati, H., Rozi, M. F., Budiyanoro, C., & Sinin, H. (2022). Comparative Study of Epoxy Composites Reinforced With Kenaf Fiber and Different Types of Microparticles. *Key Engineering Materials*, 918, 73–81. <https://doi.org/10.4028/p-74282w>

Włodarczyk-Fligier, A., & Polok-Rubiniec, M. (2021). Studies of Resistance of PP/Natural Filler Polymer Composites to Decomposition Caused by Fungi. *Materials*, 14(6), 1368. <https://doi.org/10.3390/ma14061368>

Zamani, P., Alaei, M. H., Silva, L. F. M., & Ghahremani-Moghadam, D. (2022). On the Static and Fatigue Life of Nano-reinforced Al-GFRP Bonded Joints Under Different Dispersion Treatments. *Fatigue & Fracture of Engineering Materials & Structures*, 45(4), 1088–1110. <https://doi.org/10.1111/ffe.13652>

CHAPTER 8

NANO SURFACE PRODUCTION AND APPLICATIONS USING NATURAL HONEY

NACIYE SÜNDÜZ OĞUZ¹

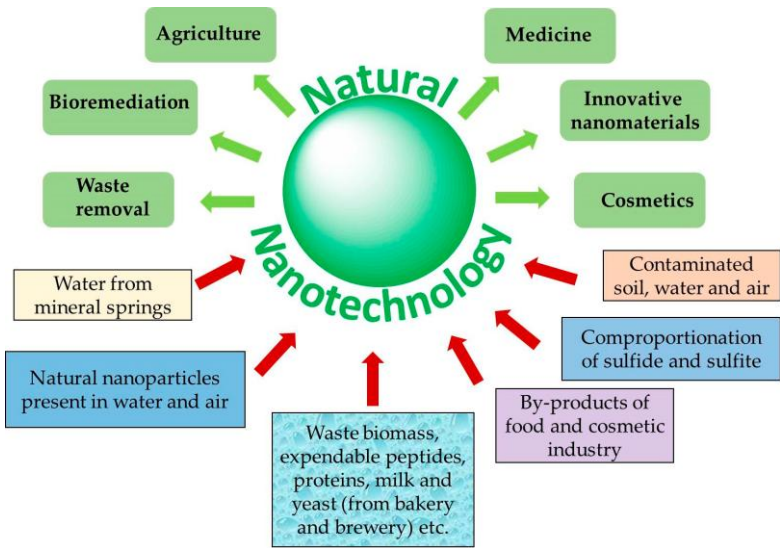
Introduction

Nanotechnology is a branch of science that enables the production of new materials, devices and systems by examining the physical, chemical and biological properties of materials at nanometer scale (Naschie, 2006). Nanotechnology is used in many areas such as materials and manufacturing, defense, space and aviation, electronics and information systems, medicine and health, textile, environment, energy, food, construction, automotive, biotechnology and agriculture, science and education. In this way, more durable, long-lasting, lightweight, smart products that have advantages over traditional production methods are produced by using less material and energy (Erkoç, 2008; Kadioğlu, 2010). It is used in many areas, from products that provide early diagnosis and

¹ Assistant Professor, Naciye Sündüz OĞUZ, Kastamonu University, Araç Rafet Vergili Vocational School, Department of Medical Services and Techniques, Kastamonu/ Turkey, Orcid: 0000-0002-3640-8038, noguz@kastamonu.edu.tr.

treatment in the health sector to antibacterial, stain-proof, non-wrinkling functional textile products in the textile sector; from robotic systems to artificial muscle, tissue, and organ applications, making human life easier (Ergül&Çakır, 2022). As seen in Figure 1, nanotechnology has a wide range of applications not only in these areas but also in less obvious areas such as agriculture and waste (Griffin et al., 2017).

Figure 1. Places where nanotechnology is used



Reference: Griffin et al., 2017

Nanosurfaces provide functionality and efficiency in a wide range of areas, leading to modern technologies. Nanosurfaces affect cell adhesion, proliferation and differentiation. They are used in biocompatible implants and tissue engineering, controlling cell behavior in biomedical applications (Kunrath et al., 2020). Antibacterial properties are provided to nanosurfaces by inhibiting pathogens by physical or chemical means and reducing the risk of infection (Guduru et al., 2011). Nanosurfaces increase the therapeutic properties by providing targeted, controlled release of

drugs (Xu et al., 2007). Nanosurfaces are used in sensors and biosensors by increasing sensitivity in molecular recognition systems due to their high surface area; in energy systems by increasing efficiency with nanocoatings that increase light absorption in solar panels (Ramos et al., 2017; Palmer, 2003). They are used in environmental technologies to increase reactivity in gas sensors and water purification systems (Rosei, 2004).

Naturally sourced materials have an important place in nanotechnology due to their advantages such as environmental friendliness, biocompatibility, biodegradability and functionality. Natural products are converted into nanocarriers using bioactive compounds such as plant-derived phenols, flavonoids and triterpenes with the nanoencapsulation method and used in drug delivery systems (Xia et al., 2024). In terms of environmental sustainability, naturally occurring nanomaterials such as sulfur and selenium nanoparticles produced by bacteria and fungi in nature are alternatives to synthetic nanomaterials (Griffin et al., 2017). The role of natural biopolymers such as gelatin, chitosan and pectin is important in nanomaterials. They are used in tissue engineering and drug delivery systems by producing sustainable nanostructures (Kumar & Abrahamse, 2020). Using nanotechnology, natural components are transformed into controlled release products and used in food supplements, pharmaceuticals and cosmetics (Mota et al., 2020). Naturally sourced materials have great potential in nanotechnological applications because they are biocompatible and environmentally friendly.

For centuries, people have used components obtained from nature for therapeutic purposes. Honey, one of these natural agents, has long been considered not only a nutritious food, but also a wound healing and anti-infection agent in traditional medicine. In particular, the healing effects of honey on open wounds, burns, and ulcerative lesions have been observed in ancient Egyptian, Mesopotamian,

Chinese, and Indian civilizations (Molan, 2001; Mandal & Mandal, 2011). Scientific studies have shown that these effects are based on the low pH, high sugar content, phenolic compounds, hydrogen peroxide production, and flavonoids of honey (Alvarez-Suarez et al., 2013; Tashkandi, 2021).

Nowadays, when developing products for wound healing, not only infection control but also features such as biocompatibility, tissue regeneration and moisture balance are required. These requirements have brought new generation biomaterial technologies to the agenda. In this context, the electrospinning method has come to the forefront in biomedical applications by enabling the production of micro and nanometer diameter fibers. Nanofibers obtained by the electrospinning method are intensively researched in areas such as wound dressings, drug delivery systems and tissue scaffolds due to their advantages such as high surface area/volume ratio, controlled porosity and customizable composition (Ramakrishna et al., 2006; Bhardwaj & Kundu, 2010).

The electrospinning process is based on the conversion of natural or synthetic polymer solutions into fibers under high voltage. When antibacterial or biological agents are integrated into the process, it becomes possible to produce functional and targeted biomaterials. In this direction, in recent years, the integration of honey into the electrospinning solution and its conversion into nanofibrous structures has come to the fore as an innovative approach in terms of the production of functional materials inspired by nature (Boateng & Catanzano, 2015). With its antibacterial and antioxidant properties, honey increases the biological effectiveness of nanofibrous polymer matrices and plays a role in reducing microbial contamination in the wound healing process (Tashkandi, 2021).

In addition, it has been observed that there are significant differences between the biological activities of honeys obtained from

different sources (chestnut, manuka, lavender, pine, etc.). These differences can directly affect the effectiveness of honey in the electrospinning device (Scepankova et al., 2021). Therefore, the biological content, chemical structure and viscosity of the honey to be used in electrospinning fiber production should be selected appropriately. The production of honey-containing nanofibrous structures by electrospinning is an innovative field of research that combines traditional natural therapeutic agents with medicine, materials science and engineering. Thus, it contributes to the achievement of important clinical goals such as infection control and wound healing in a more effective and holistic way.

Biological Properties and Antibacterial Effects of Honey

Composition and Chemical Content of Honey

Honey is a complex natural product that bees collect and enzymatically transform flower nectar. Although its composition varies depending on its source and production conditions, it generally contains the following main components:

Carbohydrates (80-85%): Glucose, fructose, sucrose, maltose and other disaccharides.

Water (15-20%): Determines the tendency for honey to crystallize and stabilize.

Organic Acids: Acetic, lactic and formic acids, especially gluconic acid.

Enzymes: Biocatalysts such as invertase, glucose oxidase, diastase.

Phenolic Compounds and Flavonoids: Plays a role in antioxidant and antimicrobial effects.

Vitamins and Minerals: Contains vitamin C, calcium, iron, zinc, magnesium, potassium.

With its versatile chemical structure, honey becomes not only an energy source but also a bioactive product with therapeutic effects (Alvarez-Suarez et al., 2010; da Silva et al., 2016).

Antibacterial Properties

The antibacterial effect of honey is due to high osmotic pressure, low pH, hydrogen peroxide production, phenolic compounds, methylglyoxal (especially in manuka honey), and flavonoids. In addition, hydrogen peroxide production via glucose oxidase enzyme is an important antibacterial mechanism (Çakmak et al., 2023).

In addition to components such as flavonoids, phenolic acids, and methylglyoxal, the osmotic effect and low water activity of honey make it difficult for bacteria to survive. Acidic pH and H₂O₂ production provide additional antibacterial effects (Feknous & Boumendjel, 2022).

The antimicrobial effect of honey occurs through the combination of several different biochemical mechanisms:

High Sugar Concentration (Osmotic Effect): Honey draws water from the cell membranes of microorganisms, causing dehydration and cell death (Tashkandi, 2021).

Low pH: Generally, the pH is between 3.2–4.5 and inhibits bacterial growth (Tashkandi, 2021).

Hydrogen Peroxide Production: H₂O₂, produced at low levels by the glucose oxidase enzyme, provides the long-term antibacterial effect of honey (Molan, 2001).

Non-peroxide Antibacterial Factors: Especially in some species such as manuka honey, there are strong antibacterial compounds such as methylglyoxal (MGO) (Schiesser et al., 2018).

Phenolic Compounds and Flavonoids: It has a cell-protective effect against oxidative stress and has a direct toxic effect against microorganisms (Eteraf-Oskouei, & Najafi, 2013).

These properties of honey are effective against both Gram-positive (e.g. *Staphylococcus aureus*) and Gram-negative (e.g. *Escherichia coli*) bacteria. Honey has been shown to be effective even against antibiotic-resistant strains (e.g. MRSA) (Sabo et al., 2015, Buchari & Amirsyah, 2024). The combination of low pH, high sugar concentration, hydrogen peroxide, phenolic compounds, flavonoids, methylglyoxal, etc. explains the broad-spectrum antimicrobial effect of honey (Israili, 2014).

Antibacterial Activity of Different Types of Honey

The source of honey directly affects its antimicrobial potential. For example:

Manuka Honey: Obtained from the *Leptospermum scoparium* plant. It exhibits strong non-peroxide effects thanks to its high methylglyoxal (MGO) content (Kwakman & Zaat, 2012). Manuka honey owes its antibacterial effect largely to its methylglyoxal content. This compound offers an antibacterial pathway independent of the classical hydrogen peroxide effect (Feng, 2023)

Chestnut Honey: Common in some regions such as Turkey, it draws attention with its high antioxidant capacity (Sevin, 2018).

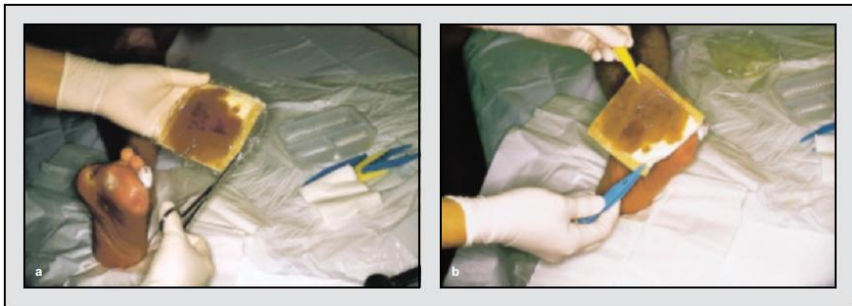
Pine Honey (Honey Glue): High in polyphenol content, offers antioxidant and antimicrobial effects (Sevin, 2018).

These differences are important in the selection of the type of honey to be used in electrospinning studies.

Biocompatibility of Honey and Its Contribution to Wound Healing

Honey has high compatibility with biological systems. It reduces inflammation in wound tissue, promotes granulation tissue formation and accelerates epithelialization. It also supports bleeding control by reducing fibrinolytic activity. It supports local immune response by affecting cytokine release with its immunomodulatory properties (Van den Berg et al., 2008). These properties have made honey an attractive bioactive agent for use in wound dressings and nanofibrous structures.

Figure 2. Honey-impregnated dressings



Reference: Molan, 2001

As seen in Figure 2, honey-impregnated dressings are one of the easy ways to apply honey to a wound to benefit from its wound-healing properties (Molan, 2001).

Nano Surface Production

The production of nanosurfaces is one of the most important areas of nanotechnology, materials science and engineering. The functionality, chemical structure and morphology of the produced surface depend on the raw material properties, the method used and the environmental conditions. Nanosurface production techniques are divided into three as physical, chemical and biological (Rossi & Marrazzo, 2021).

Physical Methods: Techniques such as physical vapor deposition (PVD), atomic layer deposition (ALD) and laser ablation require high temperature and vacuum. This limits the use of heat-sensitive natural materials.

Chemical Methods: Methods such as sol-gel, electrodeposition and chemical vapor deposition (CVD) provide homogeneous coating on large surfaces.

Biological Methods: Green synthesis methods using plant extracts and natural products (e.g. honey) are becoming increasingly widespread due to their environmental friendliness (Firmanda et al., 2024).

Nano Surface Production Using Natural Honey

Honey stands out as an environmentally friendly, functional and sustainable alternative in nano surface production with the enzymes, polyphenols and sugar structure it contains. Nano surfaces are produced with sol-gel, electrodeposition, green synthesis, coating methods and electrospinning methods.

Sol-Gel Method: It provides the formation of nano structures with the condensation and hydrolysis reactions of metal alkoxides. The sugars and polyphenols contained in honey form complexes with metal ions and create a reactive environment. It also contributes to the nano surface by controlling surface roughness and creating a template-stabilizer (Ghorbani et al., 2021).

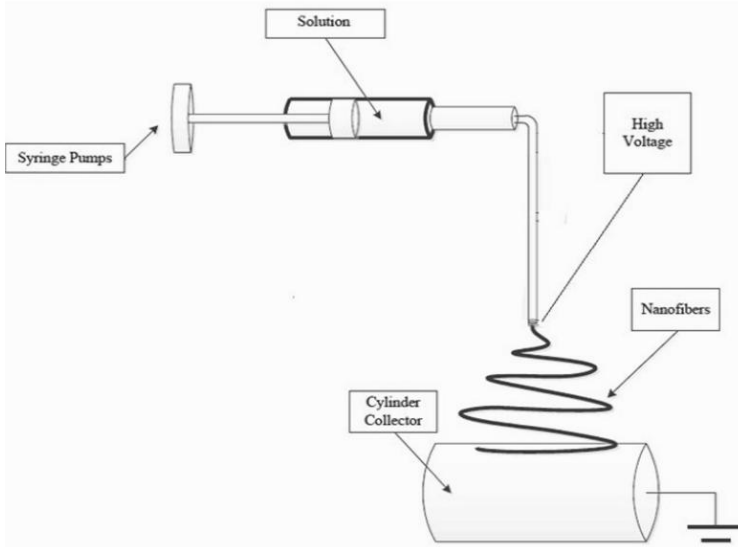
Electrodeposition: By depositing metal ions on the surface with the help of electric current, honey improves the conductive environment, supports ionic transport and contributes to the formation of regular nanostructures on the surface. Honey provides bioactive function to the coating with its antibacterial properties (Rossi & Marrazzo, 2021).

Green Synthesis: In this sustainable method where natural reducing and template agents are used instead of environmentally harmful chemicals, honey converts metal ions into nanoparticles as a reducing agent, controls particle size as a stabilizer, and produces functional nano surfaces with antioxidant and antibacterial properties (Skadiņš et al., 2023).

Spin Coating / Dip Coating: This method allows thin film coating to be applied to surfaces. With this method, honey can produce antibacterial and biocompatible wound dressings in biomedical applications by carrying bioactive molecules and adjusting the viscosity of the solution (Firmanda et al., 2024).

Electrospinning: It is a technique that enables the conversion of polymer solutions or melts into submicron or nano-sized fibers under high voltage. As seen in Figure 3, very thin fibers can be produced using a syringe, voltage device, and collector, and it has a wide range of uses in biomedical applications and tissue engineering. Nanofibers obtained by electrospinning are used in wound dressing materials due to their advantages such as controlled drug release, high surface area and porosity (Bhardwaj & Kundu, 2010, Ramakrishna et al., 2005). Honey is a natural additive integrated into electrospun nanofibers due to its antibacterial, anti-inflammatory and antioxidant properties (Mandal & Mandal, 2011, Alvarez-Suarez et al., 2013, Khanzada et al., 2024).

Figure 3. Electrospinning mechanism



Reference: Khanzada et al., 2024

Integration Methods of Natural Honey into Nanofibers

Honey is integrated using biodegradable and biocompatible polymers such as PVA (polyvinyl alcohol), PCL (polycaprolactone) and chitosan, as it is too viscous and has low polymer chain density to be electrospun alone.

Main methods:

- Direct electrospinning of honey–polymer solution
- Coaxial electrospinning (honey encapsulation with core-shell structures)
- Post-processing encapsulation after electrospinning (Boateng, & Catanzano, 2015, Cheriyan et al., 2025).

By adding honey, the antibacterial properties of nanofibers increase, their hydrophilic nature improves, and they support cell proliferation. However, high honey concentrations may negatively

affect fiber morphology by causing an increase in fiber diameter and bead formation. Therefore, the appropriate polymer-honey ratio and electrospinning parameters need to be optimized (Kirupha et al., 2021, Ghalei et al., 2021, Ghorbani et al., 2021).

Difficulties and Solutions in the Electrospinning Process of Honey

Viscosity Mismatch

The high viscosity of honey can cause irregularities in fiber morphology by reducing the fluidity of the electrospinning solution and making jet formation difficult, leading to thickening of the fibers and bead formation. Therefore, mixing honey with polymers in appropriate proportions can optimize the viscosity of the solution (Kassem et al., 2023).

Conductivity Change

The ions contained in honey can increase the electrical conductivity of the solution, and this increase can cause changes in fiber diameter and morphological deterioration during electrospinning. The concentration of honey should be carefully adjusted to keep the conductivity of the solution under control, and conductivity-balancing additives should be used when necessary (Rezeki & Surini 2019).

Hygroscopic Effect

The hygroscopic (humidifying) property of honey can cause electrospun fibers to absorb moisture, reducing the structural stability of the fibers. By creating multilayered structures or using honey with polymers with reduced hydrophilicity, the fibers can be protected from the hygroscopic effect (Kirupha et al., 2021, Ghalei et al., 2021, Ghorbani et al., 2021).

Sterilization Problem

The electrospinning process of honey offers potential benefits in biomedical applications such as wound healing. However, considering these challenges, appropriate polymer selection, formulation optimization and sterilization methods need to be carefully planned.

Characterization of Honey Additive Nano Surfaces

Physical, chemical and biological properties of nano surfaces are analyzed in order to determine their performance in application areas.

Surface Morphology: SEM & TEM

Parameters such as pore structure, fiber morphology and homogeneity in honey-additive nano surfaces are determined by SEM (Scanning Electron Microscope) analysis. It has been observed that honey-loaded nano fibers produced by electrospinning method improve the surface smoothness of honey (Ghorbani et al., 2021).

The internal structure, particle distribution and crystal planes of the structures formed by honey with nano particles are determined by TEM (Transmission Electron Microscope) analysis. The size and distribution of metal nanoparticles formed in green syntheses made with honey can be analyzed by TEM (Ong et al., 2014).

Chemical Composition: FTIR & XPS

The binding patterns of enzymes, phenolic compounds and sugar groups naturally found in honey are analyzed with FTIR. The increase in groups such as $-OH$, $-COOH$ can be detected with characteristic peaks in FTIR spectra (Panda et al., 2021).

The presence of elements such as carbon, oxygen and nitrogen on honey-treated surfaces and their bond structures are analyzed with XPS. In nano coatings where honey is used as a

reducing agent, the chemical structure of the surface can be seen in detail (Alexander et al., 2015).

Crystal Structure: XRD

Crystal structures are analyzed by XRD on honey-doped nanoparticle surfaces. The crystalline or amorphous nature of metal oxide or metal nanoparticles produced using honey is determined by XRD (Yang & Hong, 2024).

Hydrophobicity and Surface Roughness

Contact angle measurements reveal the behavior of honey-doped surfaces against water. Sugars and proteins contained in honey can reduce the contact angle by creating hydrophilic regions on the surface or make it superhydrophobic at appropriate concentrations (Coffinier et al., 2013).

The roughness of the honey-doped nanosurface is measured by topographic changes at the nano level and irregularities in the fiber structure and AFM (Atomic Force Microscopy) (Prajitno et al., 2016).

Antimicrobial and Biocompatibility Tests

Honey inhibits bacterial growth when applied to a surface due to its natural antibacterial properties. It has been seen with MTT and cell proliferation tests that honey-containing surfaces are not toxic to human cells and support cell growth (Ghorbani et al., 2021).

Application Areas of Honey-Added Nanosurfaces

Biomedical Applications

Honey can be integrated into many biomaterial systems thanks to its wound healing, antimicrobial and antioxidant properties. It is an ideal natural additive especially for nanofibrous structures and biodegradable coatings.

Wound dressings: Honey and propolis-based nanomaterials reduce inflammation, accelerate tissue regeneration and stimulate collagen synthesis (Jaldin-Crespo et al., 2022).

Antibacterial nanofibers: Honey-loaded nanofibers produced by electrospinning method show over 98% antibacterial properties against pathogens such as *S. aureus*, *E. coli* and *P. aeruginosa* (Dehdast et al., 2020).

Food Packaging Applications

When integrated into food packaging, honey's natural antimicrobial components (flavonoids, enzymes) extend shelf life and prevent pathogen growth.

Nano-composite packaging: Films formed with a mixture of bacterial cellulose and honey can also be used as packaging materials to delay spoilage in foods, along with their wound-healing properties (Nezhadmokhtari et al., 2021).

Antimicrobial food coatings: Nanomaterials produced with honey are applied to food surfaces and reduce microbial contamination, especially in meat and dairy products (Bumbudsanpharoke et al., 2015).

Antiviral Surfaces

Honey has a low pH and a hyperosmotic structure, which prevents viruses from interacting with the cell membrane. Honey-added surfaces have a feature that prevents the spread of respiratory viruses (Rossi & Marrazzo, 2021).

Antiviral coatings: The polyphenols contained in honey have an effect on viruses. For this reason, coatings that can be used in medical equipment and masks are being developed (Rossi & Marrazzo, 2021).

Environmentally Friendly Water Purification Systems

Honey is used as a reducing and template agent in green synthesis processes to produce environmentally friendly metal oxide nanoparticles that are effective in water purification.

Silver/zinc nanoparticles: These nanoparticles synthesized with honey are effective in killing pathogens released into water (Abeska & Çavaş, 2022).

Honey-containing adsorbents: Cu/Al-LDH structures synthesized with honey are used for both dye retention and drug release, providing environmentally friendly purification solutions (Bagheri & Ranjbar, 2025).

Usage in Solar Panels and Optical Sensors

Carbon-containing components of honey can be carbonized to form highly transmissible and conductive structures.

Sensor systems: Honey can be integrated into chemical vapor detection systems by using it as a capping agent in metal nanoparticle synthesis (Chaharlangi et al., 2021).

CuO/Ag composites synthesized with honey: Thanks to their enhanced photocatalytic properties, they can double-function as antimicrobials by using sunlight more efficiently (Gebremichael et al., 2025).

Conclusion

Recently, with the development of technology, the tendency towards nanotechnology in the fields of medicine, material science and engineering has increased. Today, honey, which has great importance in terms of health, is used not only as a food but also as a nanotechnology product with versatile functionality. It has great importance in terms of nano surfaces due to its functional properties and ecological properties. Since honey has wound healing, drug

release, biocompatibility, anti-inflammatory and antibacterial properties, it can make significant contributions to human health and the environment, and it has great importance and promise in the production of nano surfaces.

References

Abeska, Y. Y., & Cavas, L. (2022). Artificial neural network modelling of green synthesis of silver nanoparticles by honey. *Neural Network World*, 32(1), 1.

Alexander, S., Morrow, L., Lord, A. M., Dunnill, C. W., & Barron, A. R. (2015). pH-responsive octylamine coupling modification of carboxylated aluminium oxide surfaces. *Journal of Materials Chemistry A*, 3(18), 10052-10059.

Alvarez-Suarez, J. M., Giampieri, F., & Battino, M. (2013). Honey as a Source of Dietary Antioxidants: Structures, Bioavailability and Evidence of Protective Effects Against Human Chronic Diseases. *Current Medicinal Chemistry*, 20(5), 621–638.

Bagheri, A. M., & Ranjbar, M. (2025). A Novel Platform for Controlled Drug Delivery and Dye Removal; Green Synthesis and Characterization of Honey-Incorporated Cu/Al Layered Double Hydroxide (LDH) Nanocomposite. *Jundishapur Journal of Natural Pharmaceutical Products*, 20(1).

Bhardwaj, N., & Kundu, S. C. (2010). Electrospinning: A fascinating fiber fabrication technique. *Biotechnology advances*, 28(3), 325-347.

Boateng, J. S., & Catanzano, O. (2015). Advanced therapeutic dressings for effective wound healing—a review. *Journal of Pharmaceutical Sciences*, 104(11), 3653–3680.

Buchari, U. B., & Amirsyah, M. (2024). Antibacterial Potential of Linot Honey, Yellow Honey, and Black Honey Extracts against Methicillin-Resistant *Staphylococcus aureus* (MRSA): Inhibition Study on Wound Infections. *Gema Lingkungan Kesehatan*, 22(2), 174-177.

Bumbudsanpharoke, N., Choi, J., & Ko, S. (2015). Applications of nanomaterials in food packaging. *Journal of nanoscience and nanotechnology*, 15(9), 6357-6372.

Chaharlangi, M., Tashkhourian, J., Bordbar, M. M., Brendel, R., Weller, P., & Hemmateenejad, B. (2021). A paper-based colorimetric sensor array for discrimination of monofloral European honeys based on gold nanoparticles and chemometrics data analysis. *Spectrochimica Acta Part A: Molecular and Biomolecular Spectroscopy*, 247, 119076.

Cheriyana, S., Shin, H., Razack, S. A., Kang, M., Boopathi, T. S., Kang, H. W., & Mani, K. (2025). In-vitro and in-vivo studies of *Tridax procumbens* leaf extract incorporated bilayer polycaprolactone/polyvinyl alcohol-chitosan electrospun nanofiber for wound dressing application. *International Journal of Biological Macromolecules*, 139920.

Coffinier, Y., Piret, G., Das, M. R., & Boukherroub, R. (2013). Effect of surface roughness and chemical composition on the wetting properties of silicon-based substrates. *Comptes Rendus Chimie*, 16(1), 65-72.

Çakmak, Ö., Taş, N., Acaröz, U., Arslan-Acaröz, D., İstanbullulugil, F. R., Evrenkaya, S., & Gürler, Z. (2023). Inhibitory effects of honey on *Staphylococcus aureus* and *Escherichia coli*: A current review. *Veteriner Farmakoloji ve Toksikoloji Derneği Bülteni*, 14(3), 133-148.

Da Silva, P. M., Gauche, C., Gonzaga, L. V., Costa, A. C. O., & Fett, R. (2016). Honey: Chemical composition, stability and authenticity. *Food Chemistry*, 196, 309–323.

Dehdast, S. A., Chiari Fard, G., Maleknia, L., Giah, M., Almasian, A., & Shabani, M. (2020). Synthesis and characterization of novel antibacterial PdDA/honey nanofiber against Gram-positive

and Gram-negative bacteria. *Nanomedicine Research Journal*, 5(1), 75-89.

Deitzel, J. M., Kleinmeyer, J., Harris, D., & Tan, N. C. B. (2001). The effect of processing variables on the morphology of electrospun nanofibers and textiles. *Polymer*, 42(1), 261–272.

Ergül, V., & Çakır, S. (2023). Nanoteknolojinin Sektörel Uygulamaları Üzerine Bir Değerlendirme. *Savunma Bilimleri Dergisi*, 1(43), 1-22.

Erkoç, Ş. (2008). *Nanobilim ve Nanoteknoloji*. ODTÜ Yayıncılık, ISBN: 9786057744272, 208 s., Ankara.

Eteraf-Oskouei, T., & Najafi, M. (2013). Traditional and modern uses of natural honey in human diseases: a review. *Iranian Journal of Basic Medical Sciences*, 16(6), 731–742.

Feknous, N., & Boumendjel, M. (2022). Natural bioactive compounds of honey and their antimicrobial activity. *Czech Journal of Food Sciences*. 40(3), 163-178.

Feng, Y. (2023). Antibacterial Properties of Manuka Honey and the Role of Methylglyoxal. *Scholarly Review Journal*, (Fall 2023), 12(4), 1-12.

Firmanda, A., Mahardika, M., Fahma, F., Gozan, M., Pratama, A. W., Mardawati, E., ... & Habib, A. A. Y. (2024). Honey-loaded 3D bioprinted scaffolds: A promising fabrication with wound healing properties. *Biocatalysis and Agricultural Biotechnology*, 103247.

Gebremichael, T. E., Muleta, G. G., & Tadele, K. T. (2025). Green synthesis of Ag-doped CuO Nanocomposites Using Honey Solution for Evaluation of their Antimicrobial and Antioxidant Activities. *Current Nanomaterials*.10 (3), 333-345.

Ghalei, S., Li, J., Douglass, M., Garren, M., & Handa, H. (2021). Synergistic approach to develop antibacterial electrospun scaffolds using honey and S-Nitroso-N-acetyl penicillamine. *ACS biomaterials science & engineering*, 7(2), 517-526.

Ghorbani, M., Ramezani, S., & Rashidi, M. R. (2021). Fabrication of honey-loaded ethylcellulose/gum tragacanth nanofibers as an effective antibacterial wound dressing. *Colloids and Surfaces a: Physicochemical and Engineering Aspects*, 621, 126615.

Greiner, A., & Wendorff, J. H. (2007). Electrospinning: a fascinating method for the preparation of ultrathin fibers. *Angewandte Chemie International Edition*, 46(30), 5670-5703.

Griffin, S., Masood, M. I., Nasim, M. J., Sarfraz, M., Ebokaiwe, A. P., Schäfer, K. H., Keck, C.M., & Jacob, C. (2017). Natural nanoparticles: a particular matter inspired by nature. *Antioxidants*, 7(1), 3.

Guduru, D., Niepel, M. S., Vogel, J., & Groth, T. (2011). Nanostructured material surfaces – preparation, effect on cellular behavior, and potential biomedical applications: A review. *The International Journal of Artificial Organs*, 34(10), 963–985.

Hussein, S. Z., Yusoff, K. M., Makpol, S., & Yusof, Y. M. (2014). Does gamma irradiation affect physicochemical properties of honey. *Clin Ter*, 165(2), e125-133.

Israili, Z. (2014). Antimicrobial properties of honey. *American Journal of Therapeutics*, 21(4), 304–323.

Jaldin-Crespo, L., Silva, N., & Martínez, J. (2022). Nanomaterials based on honey and propolis for wound healing—a mini-review. *Nanomaterials*, 12(24), 4409.

Kadioğlu, F. (2010). Fen Öğretiminde Öğrenim Gören Öğretmen Adaylarının Nanoteknoloji ile İlgili Güncel ve Geleceğe Yönelik Düşünceleri. *Gazi Üniversitesi, Eğitim Bilimleri Enstitüsü*,

Biyoloji Bölümü, Ortaöğretim Fen ve Matematik Alanları Eğitimi Ana Bilim Dalı, Biyoloji Öğretmenliği Bilim Dalı, 99s, Ankara.

Kassem, L. M., El-Deen, A. G., Zaki, A. H., & El-Dek, S. I. (2023). Electrospun manuka honey@ PVP nanofibers enclosing chitosan-titanate for highly effective wound healing. *Cellulose*, 30(10), 6487-6505.

Khanzada, H., Munir, M. U., Kumpikaite, E., & Riaz, S. (2024). Development of Iodine and Honey Based PVP Electrospun Fibers for Biomedical Applications. *Arabian Journal for Science and Engineering*, 1-10.

Kirupha, S. D., Elango, S., & Vadodaria, K. (2021). Fabrication of nanofibrous membrane using stingless bee honey and curcumin for wound healing applications. *Journal of Drug Delivery Science and Technology*, 63, 102271.

Kumar, S. S. D., & Abrahamse, H. (2020). Advancement of nanobiomaterials to deliver natural compounds for tissue engineering applications. *International Journal of Molecular Sciences*, 21(18), 6752.

Kunrath, M., Diz, F. M., Magini, R., & Galárraga-Vinueza, M. (2020). Nanointeraction: The profound influence of nanostructured and nano-drug delivery biomedical implant surfaces on cell behavior. *Advances in Colloid and Interface Science*, 284, 102265.

Kwakman, P. H. S., & Zaat, S. A. J. (2012). Antibacterial components of honey. *IUBMB Life*, 64(1), 48–55.

M. Alvarez-Suarez, J., Giampieri, F., & Battino, M. (2013). Honey as a source of dietary antioxidants: structures, bioavailability and evidence of protective effects against human chronic diseases. *Current medicinal chemistry*, 20(5), 621-638.

Mandal, M. D., & Mandal, S. (2011). Honey: its medicinal property and antibacterial activity. *Asian Pacific journal of tropical biomedicine*, 1(2), 154-160.

Molan, P. C. (2001). Potential of honey in the treatment of wounds and burns. *Am J Clin Dermatol*, 2(1), 13–19.

Mota, A. H., Sousa, A., Figueira, M., Amaral, M., Sousa, B., Rocha, J., Fattal, E., Almeida, A.J., & Reis, C. P. (2020). Natural-based consumer health nanoproducts: Medicines, cosmetics, and food supplements. In *Handbook of functionalized nanomaterials for industrial applications* (pp. 527-578). Elsevier.

Naschie, M.S.E. (2006). Nanotechnology for developing world. *Chaos, Solitons and Fractals*, 30(4), 769-773.

Nezhadmokhtari, P., Asadi, N., Ghorbani, M., Del Bakhshayesh, A. R., Milani, M., & Akbarzadeh, A. (2021). Development of a Novel Film Based on Bacterial Nanocellulose Reinforced Gelatin/Guar Gum Containing Honey for Wound Healing Applications.

Ong, J. L., Appleford, M. R., & Mani, G. (2014). *Introduction to biomaterials: basic theory with engineering applications*. Cambridge University Press.

Palmer, R. E. (2003). Nanostructured surfaces. *Journal of Physics: Condensed Matter*, 15(42), E01.

Panda, P. K., Yang, J. M., & Chang, Y. H. (2021). Preparation and characterization of ferulic acid-modified water soluble chitosan and poly (γ -glutamic acid) polyelectrolyte films through layer-by-layer assembly towards protein adsorption. *International Journal of Biological Macromolecules*, 171, 457-464.

Prajitno, D. H., Maulana, A., & Syarif, D. G. (2016, August). Effect of surface roughness on contact angle measurement of nanofluid on surface of stainless steel 304 by sessile drop method. In

Journal of Physics: Conference Series (Vol. 739, No. 1, p. 012029). IOP Publishing.

Ramakrishna, S., Fujihara, K., Teo, W. E., Lim, T. C., & Ma, Z. (2005). *An Introduction to Electrospinning and Nanofibers*. World Scientific Publishing.

Ramakrishna, S., Fujihara, K., Teo, W. E., Yong, T., Ma, Z., & Ramaseshan, R. (2006). Electrospun nanofibers: solving global issues. *Materials today*, 9(3), 40-50.

Ramos, A., Cruz, M., Tovani, C. B., & Ciancaglini, P. (2017). Biomedical applications of nanotechnology. *Biophysical Reviews*, 9(2), 79–89.

Rezeki, N., & Surini, S. (2019). Optimization of PVA-Arabic gum–honey-based electrospun nanofibers as candidate carrier for peptide and protein delivery. *Pharmaceutical Sciences and Research*, 6(2), 3.

Rosei, F. (2004). Nanostructured surfaces: Challenges and frontiers in nanotechnology. *Journal of Physics: Condensed Matter*, 16(17), S1373.

Rossi, M., & Marrazzo, P. (2021). The potential of honeybee products for biomaterial applications. *Biomimetics*, 6(1), 6.

Sabo, I. A., Mahmud, T., Danlami, D., Ibrahim, H. M., & Dahiru, N. (2015). Antibacterial Potential of Honey On Some Selected Clinical Isolates. *International Journal of Innovation Sciences and Research*, 4(8), pp.366-368.

Scepankova, H., Combarros-Fuertes, P., Fresno, J. M., Tornadijo, M. E., Dias, M. S., Pinto, C. A., ... & Estevinho, L. M. (2021). Role of honey in advanced wound care. *Molecules*, 26(16), 4784.

Schiesser, A., Şimşek, D., Sarimehmetoğlu, İ., & Esendemir, G. (2018). Evaluation of Antimicrobial Activity of Methylglyoxal-The Major Antibacterial Component of Manuka Honey. *Mellifera*, 18(2), 1-6.

Sevin, S. (2018). Ülkemize özgü çam balı ve kestane balı'nın krem tarzında farmasötik şeklinin geliştirilmesi ve yara iyileşmesi üzerine etkisinin araştırılması. Ankara Üniversitesi, Sağlık Bilimleri Enstitüsü, Farmakoloji ve Toksikoloji Ana Bilim Dalı, 107s., Ankara.

Skadiņš, I., Labsvārds, K. D., Grava, A., Amirian, J., Tomsone, L. E., Ruško, J., ... & Brangule, A. (2023). Antimicrobial and antibiofilm properties of latvian honey against causative agents of wound infections. *Antibiotics*, 12(5), 816.

Tashkandi, H. (2021). Honey in wound healing: An updated review. *Open life sciences*, 16(1), 1091-1100.

Van den Berg, A. J. J., et al. (2008). An in vitro examination of the antioxidant and anti-inflammatory properties of buckwheat honey. *Journal of Wound Care*, 17(4), 172–178.

Xia, Q.-C., Liang, T., Zhou, Y., Liu, J., Tang, Y., & Liu, F. (2024). Recent advances in biomedical nanotechnology related to natural products. *Current Pharmaceutical Biotechnology*, 25(8), 944 – 961.

Xu, T., Zhang, N., Nichols, H. L., Shi, D., & Wen, X. (2007). Modification of nanostructured materials for biomedical applications. *Materials Science and Engineering: C*, 27(3), 579–594.

Yang, K. R., & Hong, M. H. (2024). Improved Biocompatibility and Osseointegration of Nanostructured Calcium-Incorporated Titanium Implant Surface Treatment (XPEED®). *Materials*, 17(11), 2707.

ADVANCED MATERIALS AND PRODUCTION TECHNIQUE APPLICATIONS

